The Longitudinal Static Stability and Control Characteristics of a Flying V Scaled Model

An Experimental and Numerical Investigation

Marco Palermo

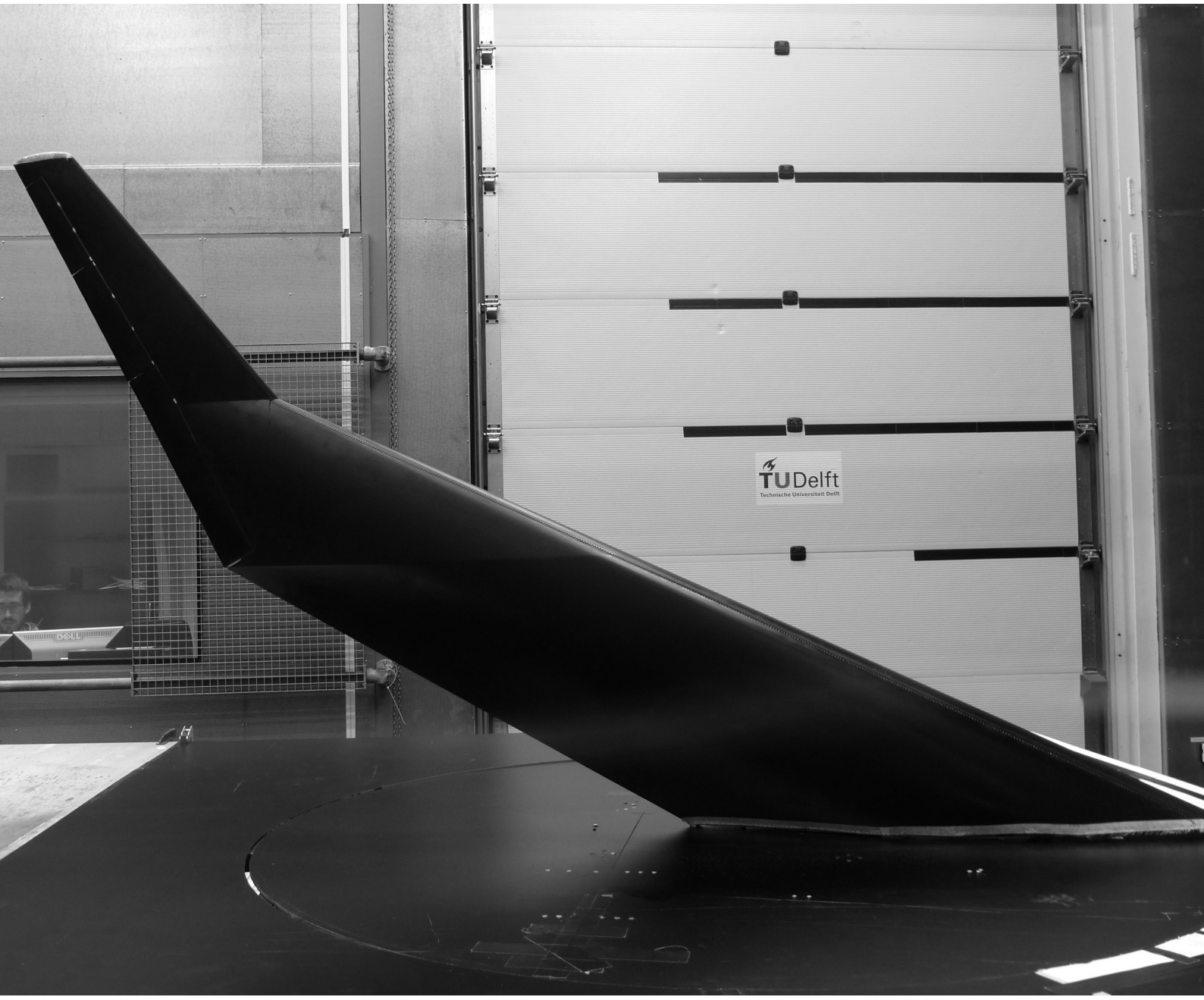

TUDelft

Flying V

The Longitudinal Static Stability and Control Characteristics of a Flying V Scaled Model

An Experimental and Numerical Investigation

by

Marco Palermo

in partial fulfillment of the requirements for the degree of

Master of Science in Aerospace Engineering

at the Delft University of Technology.

To be defended publicly on Wednesday February 27, 2019 at 13:00.

Student number:	4476174	
Duration:	January, 2018 – February, 2019	
Thesis committee:	Dr. ir. R. Vos,	TU Delft, supervisor
	Prof. dr. ir. L. M. Veldhuis,	TU Delft
	Dr. Ir. C. Borst,	TU Delft
	Ir. A. Raju Kulkarni,	TU Delft

TU Delft

Abstract

Despite widespread research into the possibilities of improving aerodynamic efficiency, a plateau seems to have been reached for the conventional configuration. Hence, the potential of unconventional configurations are being investigated in recent years. Flying V is one such configuration that promises a lift to drag ratio about 24 in cruise conditions, an improvement of 25% with respect to the NASA Common Research Model that was used as conventional configuration benchmark. In addition, the flight dynamic characteristics of such an aircraft must be investigated to ensure flight safety. Sub-scale flight testing (SSFT) allows the characterization of flight dynamics using sub-scaled models. In order to mitigate the risk of loss of control situations, the static stability and control characteristics of the model must be investigated. This research work aims to support SSFT by designing a sub-scale model and assessing its aerodynamic characteristics by wind tunnel testing. The sub-scaled design is representative of a 4.6% geometrically scaled model of full-scale Flying V design based on Froude scaling laws.

To test the aerodynamics of the future flying model, wind tunnel testing have been conducted. Balance measurements of 4.6% scaled half-model have been collected in an open jet wind-tunnel. A total of three control surfaces are installed on the model and the two inboard have been prescribed, during the design phase, to provide pitching moment control authority. The shift in aerodynamic center at higher angles of attack has been registered and large deflections of the control surfaces have been noticed to influence the shift of the aerodynamic center up to 6% of the mean aerodynamic chord.

Aside of the experimental investigations, RANS simulations have been performed using the Spalart-Allmaras one equation turbulence model. Although discrepancies have been identified between the wind tunnel and numerical results, especially in terms of drag and pitching moment coefficient, the CFD results are used to get a better understanding of the influence of vortical flows on the genesis of lift and drag over the scaled model. Based on the performed CFD simulations, it can be concluded that the performed CFD simulations are insufficient to reproduce the pitching moment behavior recorded during wind tunnel testing.

The designed sub-scaled model proved to be able to substain flight loads up to more than 2.5g at MTOM conditions. Based on the performed analyses, the center of gravity is suggested to be located between 1.33 and 1.39 meters behind the nose of the configuration. The deployed control surfaces can trim the aircraft up maximum lift coefficients between 0.6 and 0.7, depending on the location of the center of gravity, with an ultimate static stability margin equal to -4.4%. The results highlight that a reduction in pitching moment control authority would cause a reductions up to 20 % on the maximum lift coefficient achievable in trimmed conditions due to lack of control authority for forward location of the center of gravity. The designed model can therefore be used for future SSFT activities and landing speeds are estimated to be lower than 20 m/s for the proposed range of center of gravity locations at MTOM conditions.

Acknowledgements

This project has been completed thanks to many.

My supervisor, Roelof Vos for the trust, the responsibilities, and for the positive attitude in facing challenges you transferred me. Akshay Raju Kulkarni, we overcame our first impressions and worked togheter to complete this project. Malcom Brown, beside our dirvergence of opinions and arguments, which eventually we even enjoyed, your help and know-how has been priceless and without it much less would have been achieved. My teammates, Alberto Ruiz Garcia and Rob Viet. All the guys in the 6.01 for the time spent togheter.

My "Delft Brucia" friends. My flatmates, Biagio and Giulia, for making me feeling home, taking care of me everyday, eating my over-peppered cucine, and listening to my endless violin playing sessions. Peppe e Cecilia, the most far and the closest: always there keeping an eye on me.

My entire family, infinite dispenser of love.

Marco Palermo
Delft, January 2019

Contents

List of Figures ix

List of Tables xiii

1 Introduction 1

1.1 Flying Wings: a Future Opportunity? . . . 1
1.2 The Flying V Configuration . . . 3
1.3 Aerodynamic Investigation Methods in Aircraft Development Cycle . . . 4
1.4 Research Aim and Objectives . . . 6
1.5 Thesis outline . . . 7

2 Design Activities 9

2.1 Wind Tunnel and Preliminary SSFT Model . . . 9
2.1.1 Scaling Factor Selection . . . 9
2.1.2 Coordinate Systems . . . 12
2.1.3 Scaled Model Geometric Description . . . 13
2.1.4 Preliminary Sizing of the Control Surfaces . . . 14
2.1.5 Internal Structure Preliminary Design . . . 15
2.2 Wind Tunnel Setup . . . 19
2.2.1 Facility Description . . . 19
2.2.2 Description of the Testing Methodology . . . 19
2.2.3 Description of the Wind Tunnel Setup . . . 20
2.2.4 Forces and Moments Measurement Technique . . . 22
2.2.5 Test Conditions . . . 23
2.3 CFD Simulations . . . 23
2.3.1 Geometry Generation . . . 24
2.3.2 Grid Setup . . . 24
2.3.3 Simulation Setup. . . . 25
2.4 Flight Mechanic Framework . . . 27
2.4.1 Development of the Trim Algorithm . . . 27
2.4.2 Identification of the Optimal Center of Gravity Location for a Statically Stable Model . . . 28

3 Verification and Validation 31

3.1 Wind Tunnel Data Repeatibility Analysis . . . 31
3.2 Verification and Validation of the Numerical Investigations . . . 33
3.2.1 Quality Assessement of the Tetrahedral Grid . . . 33
3.2.2 Definition of the Convergence Criteria . . . 37
3.2.3 Y+ Verification . . . 38
3.2.4 Grid Dependency Study . . . 40
3.2.5 Comparison of Computational and Experimental Results . . . 41

4 Results **47**
4.1 Wind Tunnel . . . 47
4.1.1 Wind Tunnel Data Corrections . . . 47
4.1.2 Aerodynamic Characteristics of the Flying V Wind Tunnel Model . . . 48
4.1.3 Individuation of the Aerodynamic Center . . . 51
4.2 Numerical Investigation . . . 54
4.2.1 Vortex Visualization . . . 54
4.2.2 Effects of Vortical Structures on Pressure Coefficient Distributions Over The Wing. . . . 57
4.2.3 Aerodynamic Forces Spanwise Distributions. . . . 64
4.3 Flight Mechanic Analyses . . . 68
4.3.1 Identification Optimal Center of Gravity Location . . . 69
4.3.2 Center of Gravity Influence on Max Trimmed Lift Coefficient . . . 70
4.3.3 Identification Most Forward and Aft Center of Gravity Location for a Stable SSFT Model. . . 74
4.3.4 CoG Longitudinal Location and CSDR Effects on Max Trimmed Lift Coefficient . . . 75

5 Conclusions and Recommendations **83**
5.1 Conclusions. . . . 83
5.2 Recommendations . . . 85

Bibliography **87**

Appendices **91**

A Appendix A **93**

B Appendix B **95**

List of Figures

1.1 Artistic representation of the original Flying V configuration [1, 2]. . . . 3
1.2 Flying V - A350-900 planform comparison [2]. . . . 4
1.3 Aircraft development cycle. . . . 5
1.4 Modified aircraft development cycle. . . . 5

2.1 Scaling factor effect on V_∞-C_L. . . . 10
2.2 W/S and MTOW vs scaling factor. . . . 10
2.3 Mean geometric section thickness varying the scaling factor. . . . 10
2.4 Flying V model planform top view. Wing characteristics. Dimensions in mm. . . . 13
2.5 Flying V model planform top view. Control Surfaces characteristics. Dimensions in mm. . . . 15
2.6 Flying V model planform top view. Control Surfaces characteristics. Dimensions in mm. . . . 16
2.7 Radiocommand input to control surface deflections. . . . 17
2.8 CAD Model Internal Structure. Top View. . . . 17
2.9 CAD Model Internal Structure. Isometric View. . . . 17
2.10 Manufacturing. Assembly of the structure on-going. . . . 19
2.11 Manufacturing. Assembly of the structure completed. . . . 19
2.12 Drawings of the wind tunnel setup. Dimensions in millimeters. . . . 20
2.13 Lateral view of the experimental setup. . . . 21
2.14 Front view of the experimental setup. . . . 21
2.15 Isometric view of the wind tunnel setup. Dimensions in millimeters . . . 22
2.16 Simulation domain. Dimensions in meters. . . . 24
2.17 Mesh side view. . . . 25
2.18 Wing surface mesh. Top view. Flow direction from right to left. . . . 25
2.19 Root airfoil mesh. Side view. Flow direction from right to left. . . . 25
2.20 Mesh boundary conditions. . . . 26

3.1 Data repeatibility. Dataset 1. . . . 32
3.2 Data repeatibility. Dataset 2. . . . 32
3.3 Grid isosurfaces at cell volume levels equal to 10^{-9}, 0.01, and 0.1 m^3. . . . 34
3.4 Metrics distribution. Diagonal Skewness 1. . . . 34
3.5 Metrics cumulative distribution. Diagonal Skewness 1. . . . 34
3.6 Metrics distribution. Diagonal Skewness 2. . . . 35
3.7 Metrics cumulative distribution. Diagonal Skewness 2. . . . 35
3.8 Effects of large Maximum Corner Angles on faces geometry. . . . 36
3.9 Metrics distribution. Maximum Corner Angle. Wedge elem. . . . 36
3.10 Metrics distribution. Maximum Corner Angle. Tetra elem. . . . 36
3.11 Metrics distribution. Orthogonal Quality. Wedge elem. . . . 37
3.12 Metrics distribution. Orthogonal Quality. Tetra elem. . . . 37
3.13 Convergence history of the test simulation for the definition of the convergence criteria. . . . 38

3.14 Convergence history of the test simulation for the definition of the convergence criteria. 38
3.15 Max Y+ spanwise distribution. Grid 1. 39
3.16 Max Y+ spanwise distribution. Grid 2. 39
3.17 Max Y+ spanwise distribution. Grid 3. 39
3.18 Grids comparison. C_L - α curve. 40
3.19 Grids comparison. ΔC_L - α curve. 40
3.20 Grids comparison. C_D - α curve. 40
3.21 Grids comparison. ΔC_D - α curve. 40
3.22 Grids comparison. C_M - α curve. 41
3.23 Grids compamrison. ΔC_M - α curve. 41
3.24 Comparison Computational and Experimental Results. C_L vs α. 42
3.25 Comparison Computational and Experimental Results. C_D vs α. 42
3.26 Comparison Computational and Experimental Results. C_M vs α. 43
3.27 Comparison Computational and Experimental Results. C_M vs C_L. 43
3.28 Comparison Computational and Experimental Results. Aerodynamic center locations projected on the planform view of the configuration. 44
3.29 Comparison Computational and Experimental Results. $(x_{ac})_r$ vs α. 45
3.30 Comparison Computational and Experimental Results. $(y_{ac})_r$ vs α. 45

4.1 Aerodynamic effects of CS1. $V_\infty \approx 20$ m/s. $Re_{\bar{c}} \approx 1 \cdot 10^6$. $\rho \approx 1.22$ kg/m^3. 48
4.2 Aerodynamic effects of CS2. $V_\infty \approx 20$ m/s. $Re_{\bar{c}} \approx 1 \cdot 10^6$. $\rho \approx 1.22$ kg/m^3. 49
4.3 Aerodynamic effects of CS3. $V_\infty \approx 20$ m/s. $Re_{\bar{c}} \approx 1 \cdot 10^6$. $\rho \approx 1.22$ kg/m^3. 49
4.4 Pitching moment control power contours of CS1. $V_\infty \approx 20$ m/s. $Re_{\bar{c}} \approx 1 \cdot 10^6$. $\rho \approx 1.22$ kg/m^3. . . 50
4.5 Pitching moment control power contours of CS2. $V_\infty \approx 20$ m/s. $Re_{\bar{c}} \approx 1 \cdot 10^6$. $\rho \approx 1.22$ kg/m^3. . . 50
4.6 Aerodynamic center locations on the wing planform top view within the investigated range of angles of attack at different deflections. 52
4.7 Longitudinal and spanwise locations of the aerodynamic center over the tested half-wing as functions of the angle of attack for different control surface deflections. 53
4.8 Vortical structures visualization. Top view. α = 10 degrees. 55
4.9 Vortical structures visualization. Isometric view. α = 10 degrees. 55
4.10 Vortical structures visualization. Top view. α = 15 degrees. 55
4.11 Vortical structures visualization. Isometric view. α = 15 degrees. 55
4.12 Vortical structures visualization. Top view. α = 20 degrees. 56
4.13 Vortical structures visualization. Isometric view. α = 20 degrees. 56
4.14 Vortical structures visualization. Top view. α = 25 degrees. 56
4.15 Vortical structures visualization. Isometric view. α = 25 degrees. 56
4.16 Vortical structures visualization. Top view. α = 30 degrees. 57
4.17 Vortical structures visualization. Isometric view. α = 30 degrees. 57
4.18 Pressure distributions on wing sections. Isometric view. α = 5 degrees. 60
4.19 Pressure distributions on wing sections. Isometric view. α = 10 degrees. 60
4.20 Pressure distributions on wing sections. Isometric view. α = 15 degrees. 60
4.21 Pressure distributions on wing sections. Isometric view. α = 20 degrees. 61
4.22 Pressure distributions on wing sections. Isometric view. α = 25 degrees. 61
4.23 Pressure distributions on wing sections. Isometric view. α = 30 degrees. 61
4.24 Pressure distributions at different wing spanwise locations. $\alpha \in [0; 15]$ degrees. 62

4.25 Pressure distributions at different wing spanwise locations. $\alpha \in [15; 30]$ degrees. 63
4.26 Spanwise distribution. Aerodynamic Load. $\alpha \in [0; 15]$ degrees. 65
4.27 Spanwise distribution. Normalized aerodynamic load. $\alpha \in [0; 15]$ degrees. 65
4.28 Spanwise distribution. Lift load distribution. $\alpha \in [20; 35]$ degrees. 66
4.29 Spanwise distribution. Normalized lift load distribution. $\alpha \in [20; 35]$ degrees. 66
4.30 Spanwise distribution. Drag load distribution. $\alpha \in [5; 20]$ degrees. 67
4.31 Spanwise distribution. Drag load distribution. $\alpha \in [20; 35]$ degrees. 67
4.32 C_P contour on the suction side. Black edge: contour line at $C_P = 0$. $\alpha = 0$ degrees. 67
4.33 C_P contour on the suction side. Black edge: contour line at $C_P = 0$. $\alpha = 5$ degrees. 67
4.34 C_P contour on the suction side. Black edge: contour line at $C_P = 0$. $\alpha = 10$ degrees. 68
4.35 Aerodynamic characteristics of the Flying V with the center of gravity located at the optimal location. 69
4.36 Comparison clean and trimmed C_L versus α. 70
4.37 Comparison clean and trimmed C_L versus C_D. 70
4.38 Comparison clean and trimmed C_L versus α. 71
4.39 Drag versus flight speed in MTOM configuration (on the left axis). Flight speed versus lift coefficient in trim conditions in MTOM configuration (on the right axis). 72
4.40 CoG effects on C_L, C_D, and C_{M_α} in trim conditions. 73
4.41 CoG effects on α, δ_{CS1}, and δ_{CS1} in trim conditions. 73
4.42 **(a)**: C_{M_α}, $\%\delta_{CS}$, V_∞ vs α for different CoG locations in trim conditions. **(b)**: Trim diagrams of the proposed most forward and aft CoG locations for an unitary value of CSDR. Solid lines: null deflections. Triangles up lines: first and second control surfaces deflected fully upwards. 75
4.43 Trim algorithm variables at maximum and minimum trimmed lift coefficient. 78
4.44 Trim algorithm variables at maximum and minimum trimmed lift coefficient. 79
4.45 Trim algorithm variables at maximum and minimum trimmed lift coefficient. 80
4.46 Trim algorithm variables at maximum and minimum trimmed lift coefficient. 81

A.1 C_P contour on the suction side. Black edge: contour line at $C_P = 0$. $\alpha = 15$ degrees. 94
A.2 C_P contour on the suction side. Black edge: contour line at $C_P = 0$. $\alpha = 20$ degrees. 94
A.3 C_P contour on the suction side. Black edge: contour line at $C_P = 0$. $\alpha = 25$ degrees. 94
A.4 C_P contour on the suction side. Black edge: contour line at $C_P = 0$. $\alpha = 30$ degrees. 94

B.1 Support picture. Aerodynamic characteristics Flying V model. 95
B.2 Support picture. Aerodynamic characteristics Flying V model. 96
B.3 Support picture. Aerodynamic characteristics Flying V model. 96
B.4 Support picture. Aerodynamic characteristics Flying V model. 97

List of Tables

2.1 Scaling laws for *geometric Froude scaling* . . . 10
2.2 Wing planform characteristics. Dimensions in millimeters. . . . 14
2.3 Reference values of the tested model. Dimensions in International Unit System. . . . 14
2.4 Control surfaces characteristics. . . . 15
2.5 Control surfaces coordinates. Dimensions in millimeters. . . . 15
2.6 Mass breakdown of the required instrumentation. . . . 17
2.7 Preliminary mass estimation of the internal structure for half-wing. . . . 18
2.8 Mass estimation comparison between preliminary estimation and weighted components. . . . 18
2.9 Distances in in x and z directions between balance and the nose of the model. . . . 22
2.10 Test matrix CS1 and CS2 . . . 23
2.11 Wing and Volume Meshing Discretization. . . . 26
2.12 Grids Specifications. . . . 26
2.13 Applied boundary conditions. . . . 26

3.1 Confidence intervals of Dataset 1. Relative to Fig.3.1. Values reported in counts. . . . 32
3.2 Confidence intervals of Dataset 2. Relative to Fig.3.2. Values reported in counts. . . . 33
3.3 Skewness Ranges and Cell Quality [3]. . . . 35
3.4 Orthogonal Quality mesh metrics spectrum [4]. . . . 36

4.1 α_{I_1} and α_{I_2} values for three deflections of the second control surface. . . . 52
4.2 Approximate spanwise locations of the load peaks due to rolling up vortex and trailing edge suction side vortex. $\alpha \in [15; 30]$ degrees. . . . 65
4.3 Approximate spanwise locations of the load peaks due to the vortex developing in proximity of the leading edge of the wing. $\alpha \in [20; 30]$ degrees. . . . 66

Nomenclature

Latin symbols

b	Reference Span	[m]
$\bar{c}$	Mean Geometric Chord	[m]
c_{in}	Inequality Constraint	
c_{eq}	Equality Constraint	
C_D	Drag Force Coefficient	
C_L	Lift Force Coefficient	
C_{L_α}	Lift Force Coefficient derivative of the Angle of Attack	[1/deg]
C_M	Pitching Moment Coefficient	
C_{M_α}	Pitching Moment Coefficient derivative of the Angle of Attack	[1/deg]
C_{M_α}	Pitching Moment Control Power	[1/deg]
C_{M_0}	Zero Lift Pitching Moment Coefficient	
D	Drag Force	[N]
g	Gravitational Acceleration	[m/s^2]
f_s	Sampling Frequency	[Hz]
L	Lift Force	[N]
$\mathscr{M}_q$	Pitch angular acceleration per unit of pitching rate.	[1/s]
$\mathscr{M}_\alpha$	Pitch angular acceleration per unit change of angle of attack.	[1/s^2]
$\mathscr{M}_{\dot{\alpha}}$	Pitch angular acceleration per unit rate of change of angle of attack.	[1/s]
R_{F_z}	Residual of the vertical force equation	
R_{M_y}	Residual of the pitching moment equation	
S_{ref}	Reference area	[m^2]
V_∞	Free-stream airspeed	[m/s]
$V_{CS_{i-th}}$	Volume i-th control surface	[m^3]
V_w	Volume wing	[m^3]
W	Weight force	[N]
$W_{initial}$	Initial weight [N]	[N]
W_{final}	Final weight [N]	[N]
$\bar{x}$	Trim algorithm control variable vector	
$(\bar{x}_{\text{CoG}})_d$	$((x_{\text{CoG}})_r$ - $(x_{\text{LE, MGC}})_r)/\bar{c}$.	
$(x)_{(\cdot)}$	Longitudinal position in a frame of reference.	[m]
$(y)_{(\cdot)}$	Spanwise position in a frame of reference.	[m]
$y+$	height of the first boundary layer	[m]
Z_α	Vertical acceleration per unit change in angle of attack.	[m/s^2/rad]

Special symbols

@	at.
$(\cdot)\vert_{\text{Condition}}$	estimated at the condition.

Greek symbols

α	Angle of attack	[deg]
β	Side-slip angle	[deg]
$\%\delta_{CS_i}$	Percentage deflection i-th control surface	
δ_{CS_i}	Deflection i-th control surface	[deg]
ΔC_D	Deviation drag coefficient from average.	
ΔC_L	Deviation lift coefficient from average.	
ΔC_M	Deviation pitching moment coefficient from average.	
Δx_{BM}	Longitudinal distance balance to model	[m]
Δz_{BM}	Vertical distance balance to model	[m]
Λ_{LE}	Sweep angle at the leading edge	[deg]
γ	Climb angle	[deg]
$\rho_{95\%}$	95% confidence interval	
$\rho_{99\%}$	99% confidence interval	
η	Dimensionless spanwise position	
τ	Control surface local chords ratio	

Subscripts

$()_{\text{CoG}}$	Measured in the center of gravity or related to the center of gravity.
$()_{\text{CS}_i}$	Value relative to the i-th control surface.
$()_{\text{I}_i}$	of to the i-th interval.
$()_{\text{in}}$	Inboard value.
$()_{\text{out}}$	Outboard value.
$()_{\text{max}}$	Minimum value of a range.
$()_{\text{min}}$	Minimum value of a range.
$()_{\text{ph}}$	Phugoid Motion.
$()_{\text{Ref}}$	Reference value.
$()_{\text{sp}}$	Short Period Motion.
$()_{\text{w}}$	Value relative to the wing.

Abbreviations

AC	Aircraft
ac	Cerodynamic Center
BWB	Blended-Wing-Body
CFD	Computational Fluid Dynamics
CoG	Center of Gravity
CS	Control Surface
CSDR	Control Surface Deflection Ratio
KBE	Knowledge Based Engineering
MGC	Mean Geometric Chord
MGS	Mean Geometric Section
MTOM	Max Take-Off Mass
MTOW	Max Take-Off Weight
MSS	Static Stability Margin
OJF	Open Jet Facility
Re	Reynolds number
RANS	Reynolds Averaged Navier Stokes
SFC	Specific Fuel Consumption

1

Introduction

Day after day, the number of flights increases all over the world thus increasing the impact of the aviation industry on the emission of pollutants. From 1950s, the beginning of aviation era, until now, civil transportation aircraft are designed as vehicles composed of different main components: fuselage, wing, tails, and engines. This configuration is referred as conventional aircraft configuration and, although each aircraft component evolved over time, the architecture has never been drastically modified. Over the years it has reached a plateau in terms of fuel efficiency [5]. Nowadays, many research institutes are committed in developing and assessing the impact of unconventional aircraft configurations for civil transportation purposes. However, as full scale flight testing is not possible due to economical reasons, an alternative techniques are required to be used to check the dynamic characteristics of unconventional aircraft configurations, also due to the lack of legacy knowledge in the development of unconventional aircraft architectures. Over the last decades, a novel testing technique, referred as Sub-Scaled Flight Testing (SSFT), has been used to assess the flight dynamic characteristics of unconventional configurations, to investigate loss-of-control situations, and for educational purposes. The relatively low costs of SSFT investigations, compared to full-scale prototype flight testing, and the possibility of recording flight test data make this technique interesting to estimate the dynamic characteristics of under-development aircraft configurations although testing activities take place in different Reynolds and Mach regimes compared to a full-scaled design. Still, before the sub-scaled flight testing phase an initial assessment of the aerodynamic characteristics is required to be performed by wind tunnel testing to assess the flyability of the configuration in low Reynolds regimes.

1.1. Flying Wings: a Future Opportunity?

Much research has been conducted to identify new configurations to improve aircraft efficiency. The configurations referred as flying wings are identified by many authors [6–9] as a suitable candidate for future transportation aircraft thanks to the technological advantages with respect to conventional configuration aircraft. The following key features are identified in literature as potential advantages to improve aerodynamic efficiency in cruise conditions and turn into positive effects on range, which is presented in Eq. (1.1).

1. Decrease in cruise drag in Eq. 1.1, thanks to lowered number of junctions between aircraft components;

2. Increment of weight ratio in Eq. 1.1, thanks to better weight efficiency due to fuselage-wing integration;
3. Decrease of trim drag in Eq. 1.1, because of reduced stability margins. Highly affected by aerodynamic design choices.

$$\text{Range} = \frac{V_{\text{cruise}}}{g}\frac{1}{SFC}\frac{L}{D}\ln\left(\frac{W_{\text{initial}}}{W_{\text{final}}}\right) \tag{1.1}$$

Despite these promising premises, flying wings also present challenges related to aircraft stability and control due to the lack of horizontal tail [10] and, more in general, due to a lack of consolidated knowledge and experience on designing this type of unconventional aircraft [11].

Three of the main challenges in designing flying wings longitudinal controls are related to:

1. Take-off conditions, as additional pitching moment authority is required to counteract the nose down pitching moment of the weight of the aircraft about the point of contact with the ground, the pitching moment caused by the friction forces of the wheels and pitching moments arising from interference caused by ground proximity.
2. Effectiveness of the control surfaces: as the control surfaces are located at the trailing edge of the outboard sections of the aircraft to provide pitching control authority, no loss of effectiveness has to take place during low speed operations.
3. The selection of a static stability margin for a statically stable flying wing. Large static stability margins might induce complications for take-off rotation, as it would require greater pitching moment control authority, and it might also affect the range of angles of attack in which trim conditions can be achieved. On the other hand, a small static stability margin could lead the designed configuration to become statically unstable on the longitudinal channel: the natural forward shift of the aerodynamic center at high angles of attack could induce pitch-up break tendencies, and, potentially, to deep-stall.

The presented challenges in designing flying wings require high fidelity analyses to be performed to capture the flow separation phenomena which might affect the effectiveness of the control surfaces and the shift of the aerodynamic center. The shift of aerodynamic center at higher angles of attack and the effectiveness of the control surfaces are crucial points for the design of an aircraft as these influence the stablity and control characteristics of the vehicle.

To ensure static longitudinal stability, it is known that the center of gravity has to be located in front of the neutral point of the aircraft which tends to shift forward at higher angles of attack. While on a conventional aircraft stability is ensured at high angles of attack by the presence of a properly designed horizontal tail. For flying wings, the aerodynamic center of the wing coincides with the neutral point of the aircraft and the slope of the pitching moment curve can be expressed as presented in Eq. (1.2) in body axes. Therefore, to avoid the pitching moment slope to turn positive, the location of the aerodynamic center has to be known and the center of gravity range has to be selected such that stability is ensured from low to high angles of attack. Pitch-up break tendencies take place as the aerodynamic center moves forward and overtakes the center of gravity, these tendencies can eventually degenerate into deep stall tendencies if the control surfaces lose of effectiveness. As, on flying wings aircraft, the control surfaces that provide longitudinal control authority are usually deployed over the trailing edge, it has to be ensured the control surfaces can provide sufficient control authority to trim the aircraft. The latter depends on the arms of the deployed control surfaces with respect to the center of gravity location. At high angles of attack, the control surfaces have to be checked not to suffer of loss of effectiveness due to flow separation to allow maneuverability. The aerodynamic center

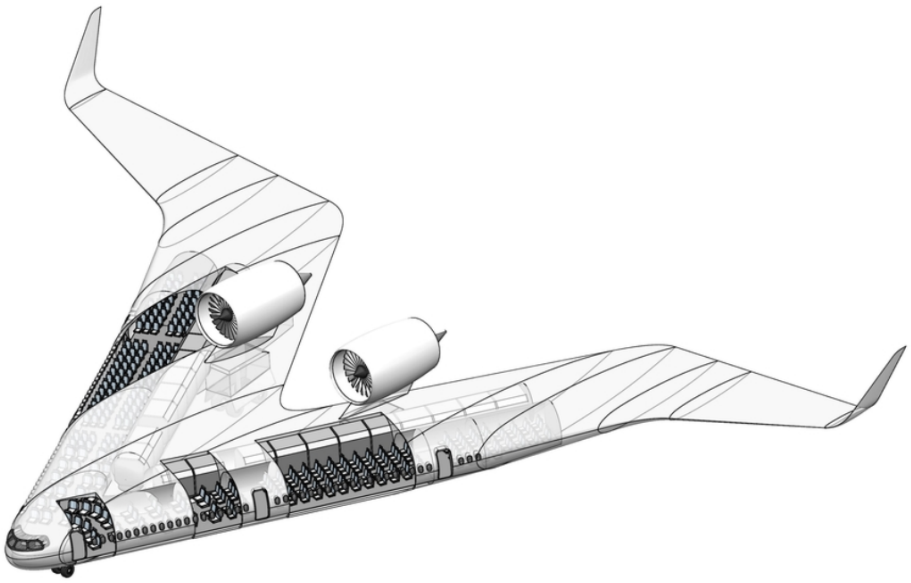

Figure 1.1: Artistic representation of the original Flying V configuration [1, 2].

location, availability of pitching moment control authority, and effectiveness of the control surfaces are all fundamental characteristics to be checked to estimate the ranges of angles of attack and airspeed in which the investigated configuration can be trimmed for different locations of the center of gravity.

$$C_{M_\alpha} = |C_{Z_\alpha}| \cdot (x_{\text{CoG}} - x_{AC}) \tag{1.2}$$

Over the last years, preliminary analyses have been performed on a novel flying wing configuration referred as Flying V Configuration. As a result, the novel flying wing design has been identified as a promising commercial transport aircraft candidate. However, the aerodynamic characteristics of the Flying V configuration, and their influence on the previously listed design challenges, are still to be investigated.

1.2. The Flying V Configuration

In 2015, Benad presented the Flying V, a new flying wing configuration, for commercial passenger transport [1] that was developed as collaboration between TU Berlin and Airbus Airbus GmbH. The design concept was intended to compete with the Airbus A350-900, about 315 passengers capability. The preliminary aerodynamic analyses were performed using the vortex lattice method tool ODILILLA. From the results by Benad, the Flying V concept would operate with a 10% greater aerodynamic efficiency in cruise and a 2% lower empty weight. A geometrically scaled demonstrator of the conceptual design was manufactured and flown, although no information are available about the applied scaling technique. An artistic representation of the original Flying V design is presented in Fig. 1.1.

The conceptual design was optimized to improve the aerodynamic efficiency [2] in cruise conditions, Mach 0.85 at 13,000 m, using as reference benchmark the NASA Common Research Model [12]. Euler simulations were used for the optimization procedure to capture the locations of the shockwaves over the wing. The optimization resulted in a very promising aerodynamic efficiency equal to 23.7 in cruise conditions, achieved by modifying both the planform of the wing and the airfoils. The aerodynamic efficiency value of the Flying V resulted about 25% larger value compared to that of the NASA Common Research Model. The predictions

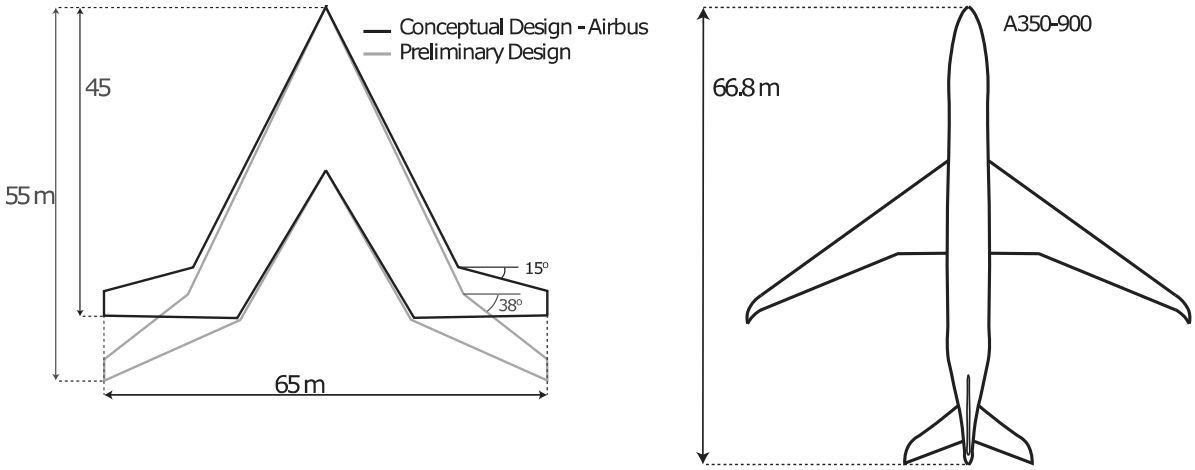

Figure 1.2: Flying V - A350-900 planform comparison [2].

in terms of cruise efficiency matched the qualitative estimations about the greater aerodynamic efficiency in cruise conditions of flying wings with respect to the conventional configuration aircraft [5–8].

The original and optimized planform of the Flying V are compared in Fig. 1.2 with the Airbus A350-900 planform view to highlight the about 18% smaller length of the novel design. Thanks to its planform geometry, the Flying V configuration is foreseen to be potentially successful for the development of aircraft families [7], which is one of the best advantages of pure flying wings with respect to other flying wing configurations [6]. A constant cross section of fuselage can be added or removed from the middle of the wing to increase, or decrease, the number of passengers without modifying the outboard zone of the wing.

Beside the promising preliminary results, still much has to be investigated on the proposed configuration especially concerning:

- The determination of the longitudinal shift of the aerodynamic center from low to high angles of attack.
- The sizing of the control surfaces to assess whether the design can satisfy aircraft regulations.
- The identification of the most forward and aft center of gravity locations and their effects on aircraft flight envelope.
- The assessment of the stall characteristics of the configuration.
- The assessment of the flight dynamic characteristics of the configuration.

1.3. Aerodynamic Investigation Methods in Aircraft Development Cycle

The development cycle of a new aircraft has not evolved so much since the beginning of aviation era. As presented in the flowchart in Fig. 1.3, the cycle is still based on four major steps: design, analyses, prototype flight testing, and series production. While a legacy knowledge has been developed over years in designing conventional configuration aircraft, not much experience is available for the design of unconventional aircraft configurations [11].

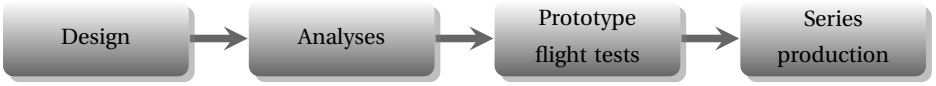

Figure 1.3: Aircraft development cycle.

During the analyses phase of the aircraft development cycle, two approaches are usually followed to estimate the high level of fidelity aerodynamic characteristics of the under development aircraft configuration in order to minimize the risks during prototype flight testing: numerical and experimental analyses.

During the past years, much research has been conducted on sub-scaled flight testing. Eventually, researchers have also speculated about embedding this novel testing technique in the aircraft development cycle between the "analyses" and "prototype flight testing" phases [13], as presented by the flowchart in Fig. 1.4.

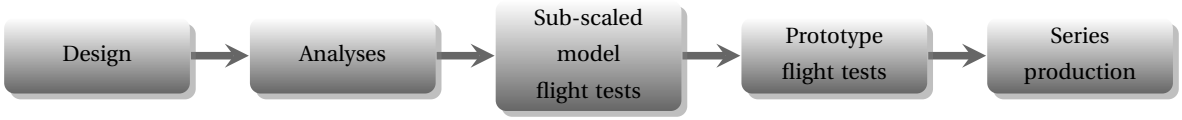

Figure 1.4: Modified aircraft development cycle.

The use of numerical analyses allows to estimate the impact of design choices on the performance of the under development vehicle without the need of producing a physical model. Currently, the best practice to perform high level of fidelity aerodynamic analyses in industrial environment is represented by RANS CFD simulations. Although more advanced models exist to numerically solve the Navier-Stokes equations, such as LES or DNS, the computational cost is too high for the currently available computers to provide results in due time [14]. Although numerical analyses are very flexible, allow to investigate different configurations, and to analyze the impact of modifications on the aerodynamic characteristics of the under development vehicle, the results from numerical analyses always require an experimental validation. The best practice in aerospace engineering environments for numerical validation is represented by wind tunnel testing [15]. The main drawback of this technique is the necessity of the right testing facility to reproduce the required flow regimes, especially in terms of Mach and Reynolds numbers. Compared to numerical analyses, wind tunnel testing allow to produce much more data in a shorter amount of time. However, wind tunnel testing require a much longer, and much more expensive, preparation as only a limited number of days is available to complete the required analyses.

Another limitation of wind tunnel testing is represented by the possibility of collecting mostly static data. To record the dynamic characteristics of an aircraft, the phase of "Prototype flight testing" is used. From an economical point of view this solution can be very risky from an economical point of view and also dangerous as loss-of-control situations can take place especially during the prototype flight testing phase [13], when the dynamic characteristics of the configuration are not completely known. Therefore, in the last decades, much research has been conducted on sub-scaled flight testing to assess whether it can be used as an intermediate stage between the analyses phase and the prototype flight testing phase. Possible positive outcomes of introducing this novel technique are represented by reduction of risk, cost and time in the maturation of aeronautical developments and in the research of novel advanced aircraft configurations, and to reduce the risk of loss-of-control conditions during flight testing [13].

Both scientific and industrial environments are still skeptical about the real utility of sub-scaled flight testing, and much research still have to be conducted especially in terms of scaling laws and aerodynamic differences between the characteristics of a sub-scaled and a full-scale aircraft. Many research activities in SSFT

have been carried out so far in the U.S. [13, 16–19]. The researches have been mostly oriented to help in the development and in assessing the flight qualities of unconventional aircraft configurations [18, 19], to reproduce aircraft flight dynamics behaviours in loss-of-control situations [17], and to use scaled models as technical demostrators to assess the feasibility of novel technologies [16].

Although sub-scaled flight testing is intended to mitigate the risks during prototype flight testing, sub-scaled flight testing itself requires risk mitigation activities as presented in the project from from Boeing [18, 19]. Prior flight testing activities, both CFD analyses and wind tunnel campaigns have been performed to know what aircraft behaviors to minimize the risks which might take place during SSFT activities.

The prior numerical and experimental investigations on the to test configuration can provide important information about the aerodynamic characteristics in terms of aerodynamic center location and effectiveness of the control surfaces, especially at high angles of attack. By preforming numerical and experimental investigation, the risks of experiencing loss-of-control situations during sub-scaled flight testing can be reduced by identifying the range of center of gravity that allow in-flight operations of the sub-scaled model and, eventually, by modifying the configuration to delay the onset of undesirable tendencies.

1.4. Research Aim and Objectives

The scope of this project is conduct a wind tunnel campaign on a Flying V scaled model as first step towards future sub scaled flight testing activities which will be useful to estimate the dynamic characteristics of a sub-scaled model of Flying V aircraft configuration. The wind tunnel testing phase is required to record the aerodynamic characteristics of the geometrically sub-scaled Flying V. Aside of the experimental part, CFD simulations are performed using the RANS Spalart-Allmaras turbulence model to replicate the aerodynamic characteristics collected in the wind tunnel, get a better understanding of the aerodynamic phenomena taking place on the Flying V model from low to high angles of attack, and assess how the presence of vortices influence the generation of aerodynamic forces over the wing.

The main objective can therefore be summarized as:

Estimation of the longitudinal stability and control characteristics of a geometrically scaled Flying V model by performing wind tunnel testing and CFD simulations.

The main research question to be answer at the end of the research project is:

What design constraint can be set on the longitudinal location of the center of gravity to make the future sub-scaled model suitable for future SSFT activities based on the available wind tunnel and CFD data?

To answer this question and reach the objective of the research, the following sub-questions have to be answered.

1. What are the aerodynamic characteristics of the geometrically scaled Flying V model? Does the model present deep stall tendencies at high angles of attack?

2. What is the excursion of the aerodynamic center between low and high angles of attack? Is it influenced by other parameters than the angle of attack?

3. To develop a stable flying model, how can an optimal location of the center of gravity be defined? If yes, where is it located?

4. What are the effects of the center of gravity location on the maximum lift coefficient achievable in trimmed steady state horizontal flight using the entire available pitching moment control authority?
5. What are the effects of using a limited amount of the available pitching moment control authority on the ranges of lift coefficients in which trim conditions can be achieved?
6. To which extent do the CFD simulations agree with the collected wind tunnel data? What are the aerodynamic phenomena reproduced by the CFD simulations and how the aerodynamic phenomena influence the generation of the aerodynamic forces at different angles of attack?

1.5. Thesis outline

The rest of the document is organized as follow.

- In Chapter 2, the design activities related to the preparation of the wind tunnel model, the wind tunnel setup, the setup of the CFD simulations, and the development of the trim algorithm used to perform trim analyses are presented.
- In Chapter 3, the verification and validation processes applied to assess the validity of the results are presented.
- In Chapter 4, the wind tunnel, CFD, and flight mechanic results are presented.
- In Chapter 5, the main conclusions that can be drawn from this study are presented and recommendations about the future phases of the Flying V scaled model project are presented.

2

Design Activities

2.1. Wind Tunnel and Preliminary SSFT Model

In the current section the following activities are presented:

- Selection of the scaling factor.
- Definition of two coordinate systems used for the design of the model and the presentation of the results.
- Description of the geometry of the designed and manufactured model.
- Preliminary sizing of the control surfaces for the wind tunnel model.
- Description of the design choices taken for the design of the internal structure of the model and the mass breakdown of the internal structure of the wind tunnel model.

2.1.1. Scaling Factor Selection

The selection of the scaling factor is performed by taking into account manufacturing requirements, the need of using off-the-shelves instrumentation to reduce the costs of the project, and flight airspeed during future in-flight operations. Further, logistic considerations have been taken into accont based on the dimensions of the laboratory for manufacturing activities and on the dimensions of the test section of the available wind tunnel facility.

The scaling procedure is performed by applying geometric Froude scaling laws [20] to the Flying V aircraft concept geometry and specifications from Faggiano [2] and Van der Schaft [21]. Geometric Froude scaling laws are presented in Table 2.1. The calculations to evaluate MTOM of the model and the airspeed required during in flight conditions have been performed at ISA sea level conditions as one of the incoming EASA regulations for flying drones is to fly in line-of-sight [22].

In Fig. 2.1, the thickness of the mean geometric chord section and of the tip section are presented. As geometric scaling is applied, the chords, thus the thicknesses, scale linearly with the scaling factor. By considering

Parameter	Symbol	Dimensional analysis	Froude scaling law
Linear dimension	l	L	n
Relative density ratio	RdR	~	1
Attitudes to the flow	α, β	~	1
Froude number	Fr	~	1
Mach number	M	~	$\sqrt{n}\frac{T_{FS}}{T_{SS}}$
Reynolds number	Re	~	$\sqrt{n^3}\frac{\nu_{FS}}{\nu_{SS}}$
Linear velocity	V	LT^{-1}	$\sqrt{n}$
Reduced angular velocity	$\bar{p}, \bar{q}, \bar{r}$	$L\,L^{-1}\,T^{-1}$	$1/\sqrt{n}$
Linear acceleration	a	LT^{-2}	1
Mass	m	M	n^3/σ
Inertia	I	ML^2	n^5/σ
Time	t	T	$\sqrt{n}$

Table 2.1: Scaling laws for *geometric Froude scaling*

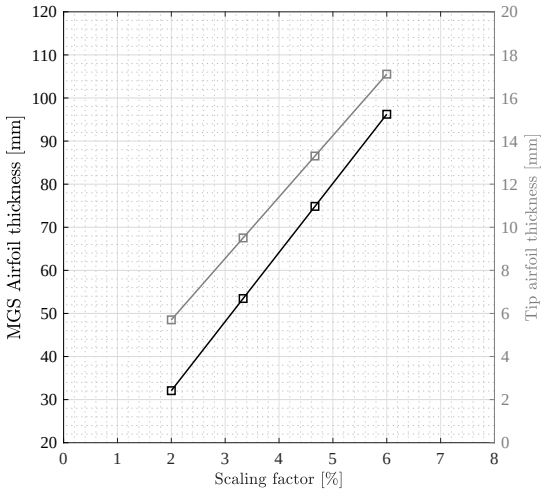

Figure 2.1: Scaling factor effect on V_∞-C_L.

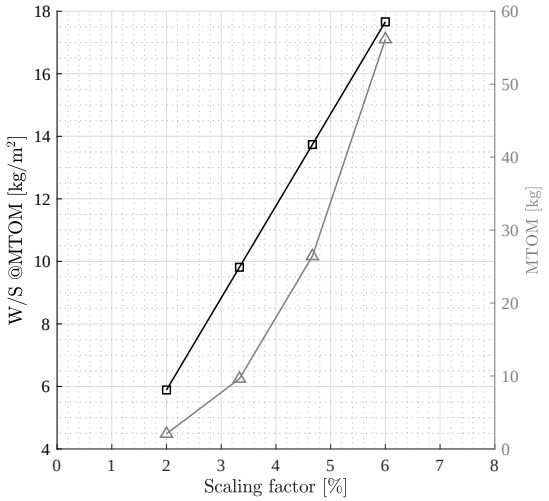

Figure 2.2: W/S and MTOW vs scaling factor.

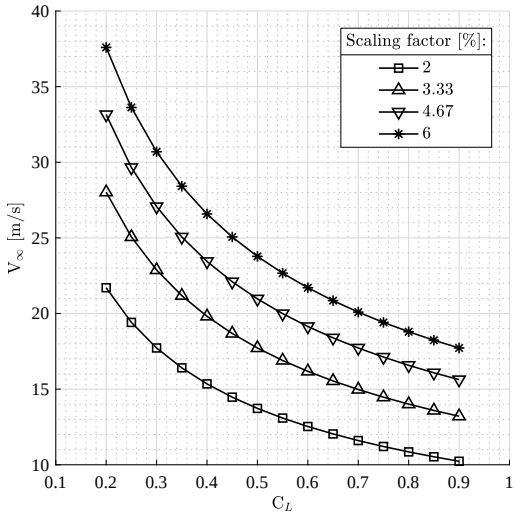

Figure 2.3: Mean geometric section thickness varying the scaling factor.

the need of installing actuators inside the structure of the model, to minimize flow disturbances due to the presence of non aerodynamic bodies, the scaling factor has to be selected to allow the installation of the required actuators inside the wing. As the tip section of the Flying V configuration presents a thickness to chord ratio about 9%, the minimum dimensions of off-the-shelves actuators available are in the range between 7 and 9 millimeters, and the wing skin has to be reinforced with foam panels to avoid buckling phenomena, the thickness of the tip section cannot be thinner than 10 millimeters.

In Fig. 2.2, the effects of scaling on the wing load and on the maximum take off weight are presented. By applying geometric Froude scaling, the mass of the scaled model scales as cubic power of the scaling factor, while reference surface scales quadratically. The two different scaling powers make the wing load of a scaled model to be linearly dependent on the scaling factor. In Fig. 2.3, the influence of scaling on wing load is made explicit by plotting V_∞-C_L. As flying in line-of-sight is one of the requirements for flying drones, the model shall operate during future SSFT activities at moderate airspeed, which would lead the scaling factor selection to be as low as possible, especially to allow landing operations at relatively low speed, lower than 20 m/s.

The long term final goal of the project is to record flight test data of the Flying V configuration both to get a better insight of the flight dynamic characteristics of this configuration and to contribute to researching sub scaled flight testing. By making use of the approximated longitudinal approach, extensively presented in may books and notes of flight dynamics [23–25], scaling influence on the motion natural frequency ω_n and damping coefficient ξ can be evaluated theoretically. By combining the dimensional stability derivatives with the scaling laws presented in Table 2.1 and using the natural frequencies and damping coefficients equations the presented equation from (2.1) to (2.4), the evaluation of scaling influence on ω_n and ξ is evaluated and presented by Eq. (2.5) and (2.6). In Eq. (2.5) and (2.6), n is the scaling percentage, which is unitary for full scale and lower then one for sub-scaled models.

Short period approximation: natural frequency and damping coefficient.

$$\omega_{n_{sp}} = \sqrt{\frac{Z_\alpha \mathcal{M}_q}{V_\infty} - \mathcal{M}_\alpha} \tag{2.1}$$

$$\xi_{sp} = -\frac{\mathcal{M}_q + Z_\alpha / V_\infty + \mathcal{M}_{\dot{\alpha}}}{2\omega_n} \tag{2.2}$$

Phugoid motion approximation: natural frequency and damping coefficient.

$$\omega_{n_{ph}} = \frac{g}{V_\infty}\sqrt{2} \tag{2.3}$$

$$\xi_{ph} = \frac{\sqrt{2}}{2\left(\frac{C_{L_0}}{C_{D_0}}\right)} \tag{2.4}$$

Froude scaling laws influence on natural frequency and damping coefficient.

$$\frac{\omega_n^{SS}}{\omega_n^{FS}} = \frac{1}{\sqrt{n}} \tag{2.5}$$

$$\frac{\xi_n^{SS}}{\xi_n^{FS}} = 1 \tag{2.6}$$

From Eq. (2.5) and (2.6), it is clearly visible that geometrical-Froude scaling has a direct effect on the natural frequencies of aircraft modes. By selecting smaller factors, the natural frequencies of the tested aircraft increase leading to the need of increasing the sampling time to record flight test data. Morelli [26] describes the sampling rate of the data acquisition system as one of the most critical parameters to collect high quality, and useful, flight test data. As rule of thumb, Morelli suggests the sampling frequency to be 25 times the maximum frequency of the frequency of the dynamic motion to record:

$$f_s = 25 f_{\max} \tag{2.7}$$

Morelli also reports that almost all the frequency of the rigid-body dynamic modes are below 2 Hz, therefore a 50 Hz sampling rate is usually sufficient. However, by recalling the implications of equation (2.5), attention has to be paid when selecting a scaling factor sub-scaled model. The works from Dorobantu et al. [27] and Lundstrom [28] have highlighted that a 50 Hz sampling rate can be sufficient to register useful flight test data, also using off-the-shelves instrumentation.

As a flight dynamic assessment of the Flying V aircraft is still not available, no calculations have been performed to estimate the required sampling frequency of the sensor during future SSFT activities by assuming a perfect aerodynamic matching between the full scale and sub-scaled aircraft. Still, the presented theory-based analysis does suggest not to select too small scaling factors.

Based on the previous considerations, the scaling factor has to be:

- As large as possible not to increase too much aircraft natural frequencies during future scaled flight testing activities.
- As large as possible not to reduce the internal volume of the model and allow the use of off-the-shelves devices.
- As small as possible to minimize take-off and landing speeds, and reduce the wing loading, to allow easier remote operations.

Based on the previous observations, a scaling factor equal to 4.6% is selected to allow internal installation of off-the-shelves actuators and to allow take-off and landing airspeed lower than 20 m/s during future SSFT activities in MTOM conditions, assuming a maximum lift coefficient achievable by the Flying V model at least equal to 0.55.

2.1.2. Coordinate Systems

The two coordinate systems used for the design of the model and the analysis of the data are here described.

The aircraft frame of reference is used to describe the geometry of the model, the origin is set to be at the leading edge point of the root airfoil. The measurements presented in this frame of reference are identified by the pedix r, $(\cdot)_r$.

The aircraft frame of reference is shifted longitudinally on the symmetry plane of the model to present some results in the last chapters of the report. The origin of this frame of reference is set to be the projection of the leading edge point of the mean geometric chord of the configuration onto the symmetry plane of the model. The measurements presented in this frame of reference are identified by the pedix d, $(\cdot)_d$.

2.1.3. Scaled Model Geometric Description

The model used for wind tunnel experiments is representative of a 4.6% geometrically scaled Flying V aircraft. The model is about 1.5 m wide and 2.5 m long. The geometry of the model is simplified by removing the second section of the design from Faggiano [2] and van der Schaft [21] for manufacturing reasons.

Three planform top views are presented in Fig. 2.4, Fig.2.5, and in Fig.2.6, to present respectively the planform characteristics of the model in terms of chords and the relative spanwise position, the planform characteristics of the designed control surfaces of the wind tunnel model abd the longitudinal and spanwise coordinates of the three control surfaces zones.

Three planform top views are presented in Fig. 2.4, to present the planform characteristics of the model in terms of chords and the relative spanwise position, in Fig.2.5, to present the planform characteristics of the equipped control surfaces of the wind tunnel model, and in Fig.2.6, to present the longitudinal and spanwise coordinates of the three control surfaces zones. In Fig.2.4, the mean geometric chord is represented by a dashed line and the quarter chord point of the mean geometric chord is presented as well.

The leading edge sweep is equal to 64.4 degrees up to $\eta \approx 0.63$, then the leading edge sweep angle reduces to 37.8 degrees up to the tip. The outer wing, $\eta \approx [0.63, 1.00]$ features -4.3 degrees of twist. Three independent control surfaces are deployed over the trailing edge of this zone of the wing, presented in Fig. 2.5. The control surfaces of the model are designed with the chords normal to the trailing edge of the local wing to allow rotation. Three actuators are installed inside the wing to remotely control the deflections of the control surfaces during wind tunnel testing. No movable is deployed on the leading edge.

The data from the planform view in Fig. 2.4, 2.5, and 2.6 are reported and elaborated in Table 2.2, 2.4, 2.5. The reference values of the tested model are reported in Table 2.3.

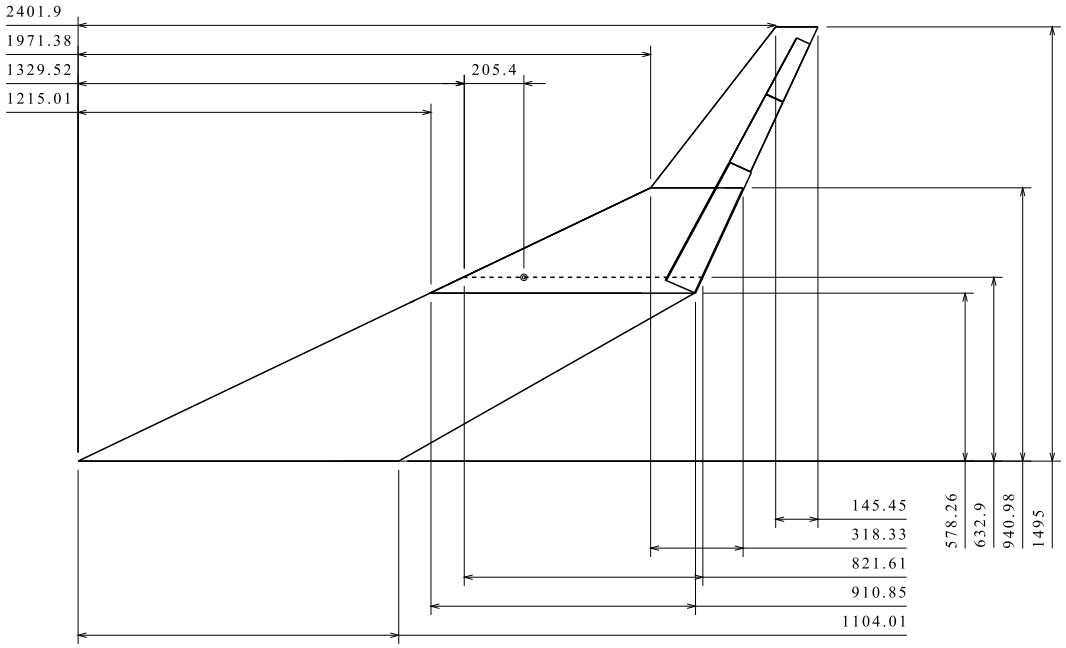

Figure 2.4: Flying V model planform top view. Wing characteristics. Dimensions in mm.

Table 2.2: Wing planform characteristics. Dimensions in millimeters.

Section	c	$(x_{LE})_r$	$(x_{1/4c})_r$	$(y)_r$	η	Λ_{LE}
1	1.104	0.00	0.276	0.00	0.00	64.4
2	0.910	1.215	1.442	0.578	0.38	64.4
3	0.318	1.971	2.050	0.940	0.63	37.8
4	0.145	2.401	2.438	1.495	1.00	37.8
MGC	0.821	1.329	1.534	0.632	0.42	64.4

Table 2.3: Reference values of the tested model. Dimensions in International Unit System.

$\bar{c}$	S_{ref}	b/2
0.820	0.9345	1.495

2.1.4. Preliminary Sizing of the Control Surfaces

As previously reported, a complete study on the aerodynamics of the Flying V aircraft is currently missing. No state-of-the-art analyses have been performed in the past to estimate the zero lift pitching moment coefficient nor the aerodynamic characteristics of the Flying V configuration at high angles of attack. A preliminary sizing of the control surfaces is therefore performed by defining an equivalent horizontal tail volume for the Flying V using, as area of the horizontal tail, the planform area in front of the control surfaces. The volume is compared with the horizontal tail volume of the Airbus A350-900, reference aircrat selected by Faggiano during the aerodynamic optimization [2].

The geometric data of the Airbus A350-900 are extracted from the top view drawing [29]. The horizontal tail volume of the Airbus A350-900 is evaluated assuming a longitudinal location of the center of gravity equal to the 25% of the mean geometric chord of the wing. A horizontal tail volume equal to $2.74 \cdot 10^3$ m^3 is calculated for the A350-900.

The same analysis is conducted on the Flying V configuration assuming to deploy control surfaces over the entire trailing edge of the second and third trunks of the wing, $\eta \in [0.38; 0.96]$. The hinge line of the control surfaces is parallel to the trailing edge of the wing and the inboard and outboard sections of each control surfaces are designed to be orthogonal to the wing trailing edge.

To perform the calculations, the reference point to evaluate the moment arm is located at the most aft center of gravity location proposed by Faggiano [2], which is at a longitudinal distance from the nose of the full-scale configuration equal to 33 meters. The trailing edges of the second and third trunk are split in three control surfaces. The aerodynamic forces acting on the control surfaces are assumed to be applied at the quarter chord of the mean geometric chord of each control surface. The control surfaces volume of the full scale Flying V evaluated as presented is equal to $3.18 \cdot 10^3$ m^3.

By deploying control surfaces over the entire trailing edges of the central and outer trunks of the Flying V configuration, a 16% larger volume of the control surfaces is featured by the flying wing configuration with respect to the Airbus A350-900.

The presented solution of deploying three control surfaces over the trailing edge of the central and outer trunks is adopted for the design of the SSFT model as:

1. The need of extra control authority during take-off is referred by Donlan [10] as one of the main challenges in the design phase of a flying wing configuration.

2. Differently from a conventional aircraft configuration, the control surfaces, at the current stage of the design, will have to provide both longitudinal and lateral control authority.

The planform characteristics of the control surfaces are presented in Fig. 2.5 and 2.6. The data relative to the control surfaces are reported in Table 2.4 and 2.5. The extentions of the three control surfaces have been chosen arbitrarily based on what follows:

- The inboard control surface (CS1) is foreseen to work as main elevator;
- The central control surface (CS2) is foreseen to provide both lateral and longitudinal control;
- The outboard control surface (CS3) is foreseen to provide mostly lateral control.

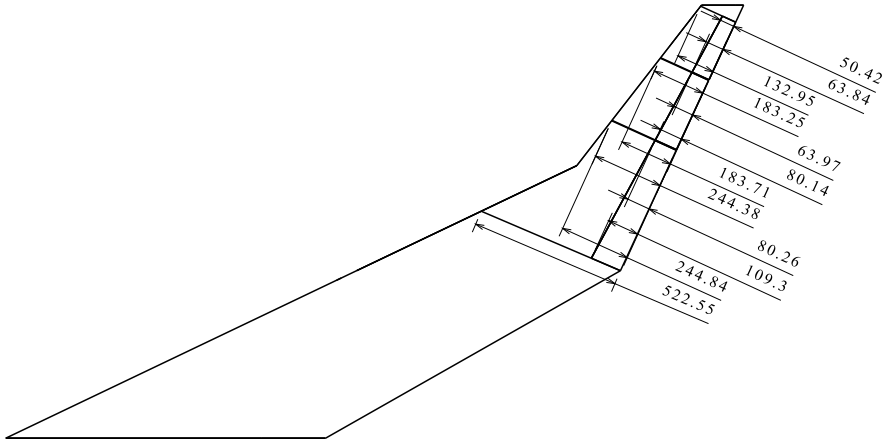

Figure 2.5: Flying V model planform top view. Control Surfaces characteristics. Dimensions in mm.

Table 2.4: Control surfaces characteristics.

CS	c_{in_w}	c_{out_w}	$c_{\text{in}_{cs}}$	$c_{\text{out}_{cs}}$	τ_{in}	τ_{out}	$x_{1/4\bar{c}_{cs}}$	$y_{1/4\bar{c}_{cs}}$	S_{cs}	S_{cs}/S_w	V_{cs}/V_w
1	0.522	0.244	0.109	0.080	0.21	0.33	1.949	0.852	0.158	0.084	0.105
2	0.244	0.183	0.080	0.064	0.33	0.35	2.222	1.178	0.056	0.030	0.057
3	0.183	0.132	0.064	0.050	0.35	0.38	2.360	1.378	0.034	0.018	0.040

Table 2.5: Control surfaces coordinates. Dimensions in millimeters.

CS	$(x_{\text{in}_{LE}})_r$	$(x_{\text{out}_{LE}})_r$	$(y_{\text{in}_{LE}})_r$	$(y_{\text{out}_{LE}})_r$	$(x_{\text{in}_{TE}})_r$	$(x_{\text{out}_{TE}})_r$	$(y_{\text{in}_{TE}})_r$	$(y_{\text{out}_{TE}})_r$
1	1641.6	2091.7	783.6	1095.7	2122.1	2314.5	578.3	994.4
2	2092.9	2259.5	1097.3	1311.7	2315.4	2426.7	996.2	1235.5
3	2260.8	2399.0	1313.3	1491.2	2427.5	2519.9	1237.3	1436.0

2.1.5. Internal Structure Preliminary Design

The scaled flight testing model based, on the selected scaling factor, the application of geometrical-Froude scaling laws, and the specifications of the full scale Flying V configuration [2] is foreseen to have a maximum take-off mass equal to 25 kg. Therefore, the only parameter to be taken into account during the design of the wind tunnel model is represented by the mass of its internal structure, as this design is foreseen to be used as a starting point for the design of the flying model. Still, foreseeing design activities related to the flying model,

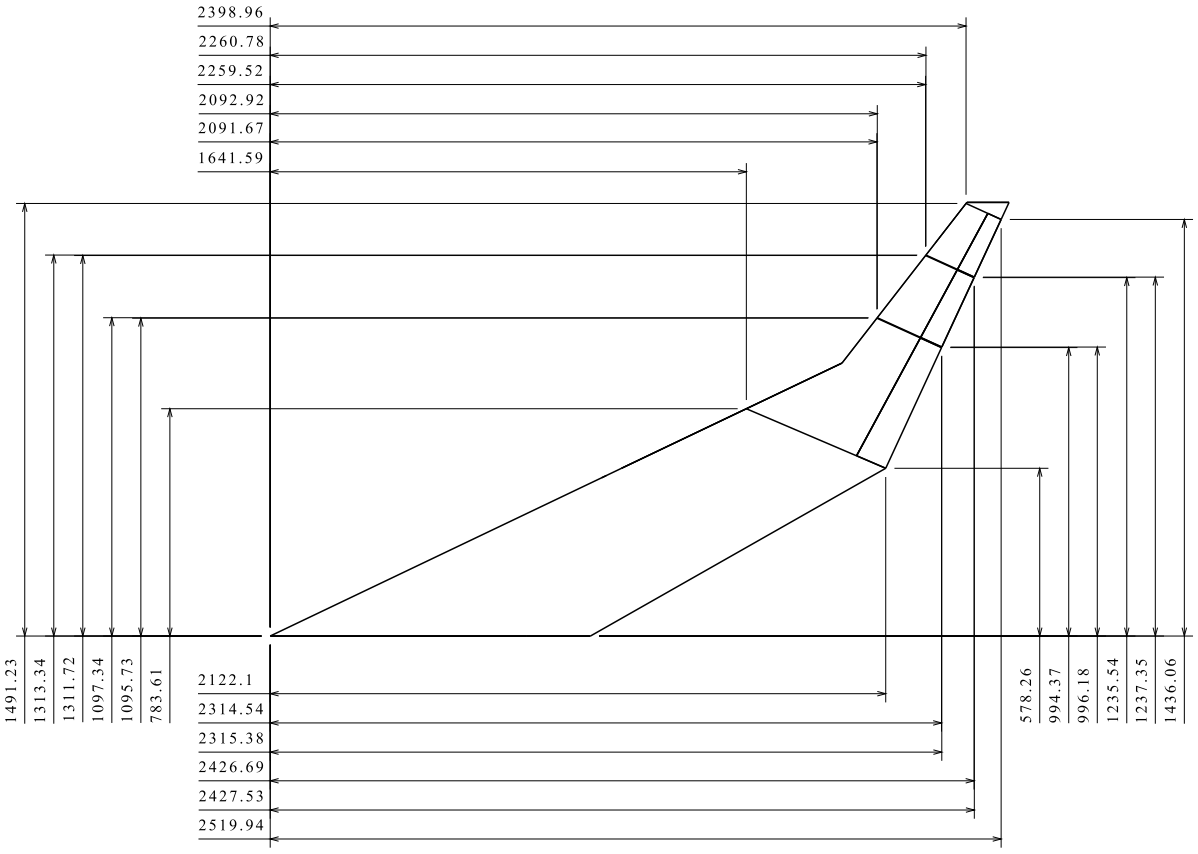

Figure 2.6: Flying V model planform top view. Control Surfaces characteristics. Dimensions in mm.

design choices are taken to allow future minor modifications to the internal structure of the model, i.e. for landing gears and engines positioning, engines or to resize the control surfaces.

The design of the structure has not involved structural calculations as it would have required too long and the wind tunnel slot would have been missed. After a preliminary estimation of the weight of the internal devices required for future SSFT activities, part of the remaining mass is allocated for the internal structure of the flying model. The mass breakdown of the required instrumentation is presented in Table 2.6. The engines have been selected to provide a static trust to weight ratio about 0.7. Based on the technical data of the engines and of the batteries, a flight test time of about 23 minutes is estimated for the flying model. The calculations on the hinge moment to select the actuators have been based on quasi three dimensional aerodynamic estimations.

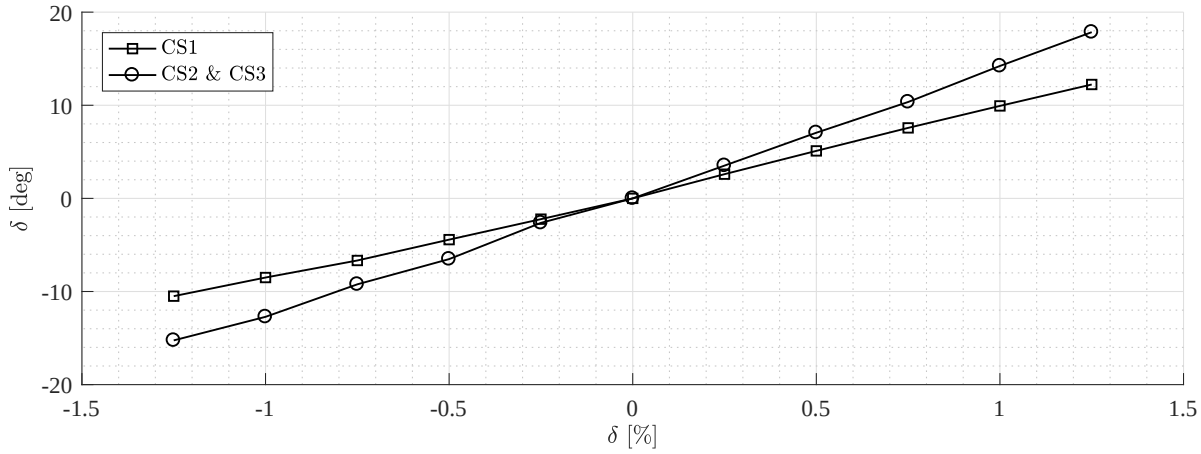

Figure 2.7: Radiocommand input to control surface deflections.

Table 2.6: Mass breakdown of the required instrumentation.

Function	Number required	Mass per unit [kg/unit]	Mass [kg]	Link
Servo CS1	2	0.068	0.136	Hitec D954SW
Servo CS2 and Rudder	4	0.025	0.100	Hitec D89MW
Servo CS3	2	0.014	0.028	Hitec HS-5070MH HV
Engines	2	1.20	2.40	DS-86-AXI HDS
Landing Gear System	1	2.235	2.23	ER-50eVo
Batteries	2	1.6	3.2	12S1P Lipo Battery Pack
Total			8.094	

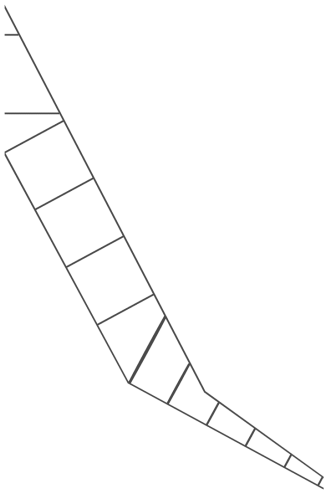

Figure 2.8: CAD Model Internal Structure. Top View.

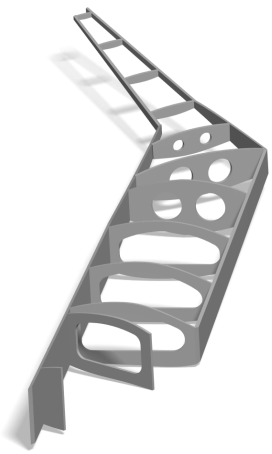

Figure 2.9: CAD Model Internal Structure. Isometric View.

The CAD model of the wing box structure is designed in CATIA V5 environment and weight estimations are performed based on the areal density of three specimen of composite material and on the surface of the designed structure. Two renderings of the CAD model of the internal structure are presented in Fig. 2.8 and

Table 2.7: Preliminary mass estimation of the internal structure for half-wing.

Part	Main wing					
Structural element	Front spar	Rear spar	Ribs	Upper skin	Lower skin	Total
Estimated mass [kg]	0.664	0.401	0.710	1.413	1.402	4.59

Part	Winglet				
Structural element	Front spar	Rear spar	Ribs	Skin	Total
Estimated mass [kg]	0.02	0.01	0.005	0.114	0.149

Table 2.8: Mass estimation comparison between preliminary estimation and weighted components.

Part	Main wing			
Structural element	Front spar	Rear spar	Upper skin	Total
Estimated mass [kg]	0.664	0.401	1.413	2.478
Measured mass [kg]	0.690	0.391	1.327	2.407
Error [%]	3.85%	-2.53%	-6.11%	-2.67%

2.9.

The preliminary weight estimation of the structure of the wind tunnel model are presented in Table 2.7. The material to manufacture the components of the internal structure of the wind tunnel model has been selected on the base of a pure shear test on a sandwich panel from which the shear characteristics of the material have been considered sufficient to withstand the forces during the wind tunnel campaign. The sandwich panel is made of three plies per side of glass fiber and a core of depron. Depron is substituded with a certified foam, Airex C70.75, for the manufacturing of the wing as depron material has been observed to release air bubbles during resin liquid infusions which might have compromised the integrity of the structure.

The wing tunnel model is completely manufactured using composite materials produced by performing resin liquid infusions. To manufacture the wing box structural elements a single sandwich has been produced and water-cut. Two moulds have been designed to manufacture the skin of the wing and these have been outsources to third party company. A picture of the internal structure sitting into the moulds during the assembly of the internal structure is presented in Fig. 2.10. A picture of the half-wing model sitting into the moulds after completing the assembly of the internal structure is presented in Fig. 2.11. The front spar, rear spar and upper skin are weighted before the assembly of the internal structure highlighting an error on the weight prediction about -2.6%. The estimated and measured masses of the front spar, rear spar, and top surface of the skin are presented in Table 2.8.

Figure 2.10: Manufacturing. Assembly of the structure on-going.

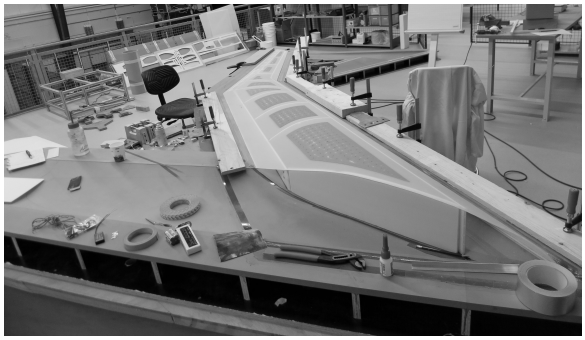

Figure 2.11: Manufacturing. Assembly of the structure completed.

2.2. Wind Tunnel Setup

The activities for the design of the wind tunnel setup are presented in the current section. The section report the description of:

- A description of the wind tunnel facility.
- The description of the testing methodology.
- The description of wind tunnel setup designed for half model wind tunnel testing.
- The instrumentation used to record aerodynamic forces and moments.
- The tested conditions.

2.2.1. Facility Description

The investigations were conducted in the TU Delft Open Jet Facility, a closed-circuit wind tunnel capable of a maximum airspeed of about 35 m/s with an octagonal nozzle section of 285 x 285 cm (H x W).

2.2.2. Description of the Testing Methodology

Half-model wind tunnel testing is selected as testing technique to based on:

- The dimensions of the available wind tunnel test section and of the model to test.
- The possibility of investigating the longitudinal aircraft characteristics of the model.
- The will of maximizing the Reynolds number of the model compared to the full-scale Reynolds in take-off conditions, about 9.6 e^7 assuming ISA model at sea level, a reference length equal to 17.6 m, and a reference take-off speed equal to 80 m/s.

Peniches were not used according to the results presented by Eder et al. [30] and the observations by Skinner et al. [31] about the influence of peniches on flow complexity and uncertainties, especially at large angles of attack.

2.2.3. Description of the Wind Tunnel Setup

The three views of the designed wind-tunnel setup for semi-span wind tunnel testing are presented in Fig.2.12. From top to bottom, the setup consists of the following devices: wind tunnel model, reflection plane, splitting plane, elliptical leading edge, model support, and balance. For sake of clarity, a simplified model of the OJF nozzle is presented in the three views as well.

Two triangular supports have been designed and CNC machined to sit flat both on the front and rear spar of the internal structure of the model and on the aluminum plate. The triangular supports are fastened both to the front spar, rear spar, and to the aluminum plate. The plate works also as root rib by connecting the front and rear spar. Forces and moments are transferred from the model to the balance using an aluminum profile as connecting element between the balance and the aluminum plate located at the root of the model. The entire supporting system is assumed to be infinitely stiff. During the wind tunnel tests, the leading edge angle of the model has been measured with a digital inclinometer indicating a leading edge sweep angle equal to 64.4 degrees.

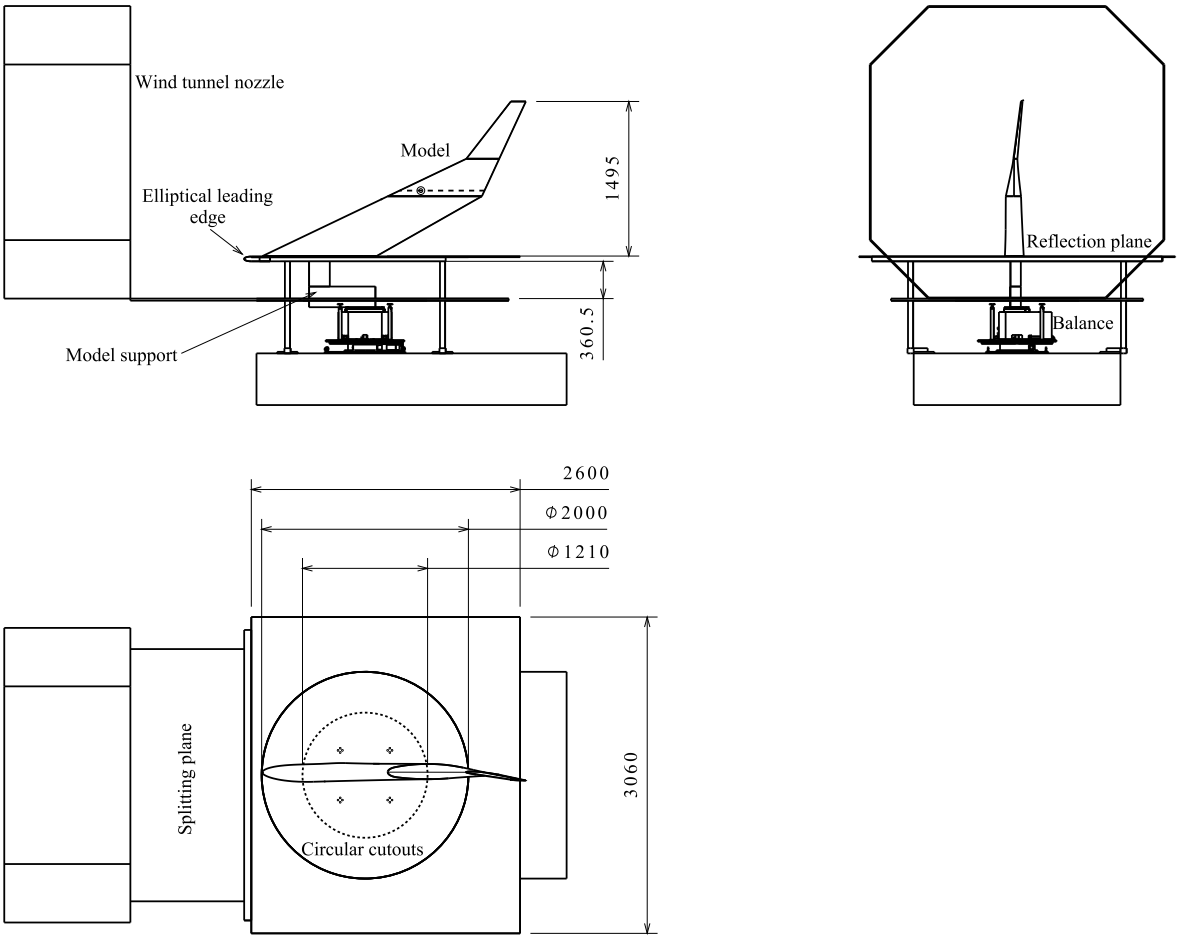

Figure 2.12: Drawings of the wind tunnel setup. Dimensions in millimeters.

The supporting system of the model is shielded to minimize its interaction with the flow flowing between the reflection and splitting plane. Elliptical leading edges are mounted on the front side of the reflection plane to avoid vortex shedding phenomena from the sharp corner of the reflection plane itself, which might have influenced the aerodynamics of the wing, and to help the development of a fresh boundary layer over the

reflection plane.

The interaction effects between the boundary layer of the wind-tunnel and the model are mitigated by vertically displacing the reflection plane and the nozzle of the wind tunnel with an offset from the wind tunnel wall. This can be observed in Fig.2.12, a 360 mm gap is present between the reflection and the splitting plane. Two pictures of the experimental setup are presented in Fig. 2.13 and 2.14. The elliptical leading edge of the reflection plane can be observed in Fig. 2.13. The shield of the supporting system of the wing can be observed in Fig. 2.14.

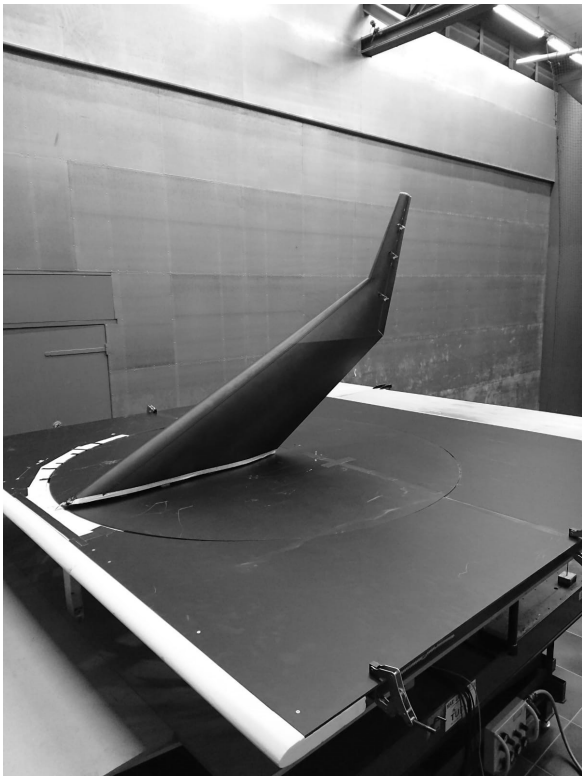

Figure 2.13: Lateral view of the experimental setup.

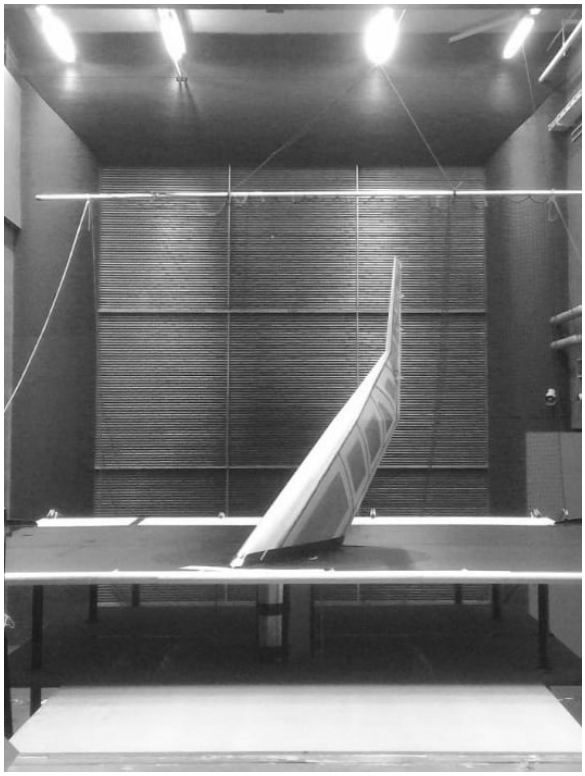

Figure 2.14: Front view of the experimental setup.

Two coaxial circles are cut out from the splitting and symmetry plane and made rotating to allow the use of an external remote-controlled turning table during testings. The circular cuts are visible in the top view of Fig.2.12: the solid circle is located on the reflection plane, the dotted circle is located on the splitting plane. The weight of the circles is completely discharged on the turning table.

The balance is directly mounted on the turning table resulting in two advantages: numerical control on the angle of attack and a fixed relative positioning between the model and the balance independent of the selected angle of attack. The use of the electric turning table and of a scale, located on the reflection plane of the setup, as well as the use of digital actuators to control the three independent control surfaces improved the quality and the repeatibility of the experiments.

The use of the turning table and the balance added two constraints to the design of the setup. The turning table can provide a maximum torque about 90 Nm which influenced the relative positioning between the wing, the balance and the turning table. The balance can handle a the maximum load in z-direction about 500 N under combined loading. The latter limitation represented the main constraint during the design of the setup and leaded to develop the described wind tunnel setup such that only the wing, and its supporting system discharged their weight onto the balance.

Δx_{BM}	Δz_{BM}
1.065	0.681

Table 2.9: Distances in in x and z directions between balance and the nose of the model.

2.2.4. Forces and Moments Measurement Technique

An external six-axes balance [32], co-axially mounted with a turning table, is used to record aerodynamic forces and moments on the aircraft during testing. The relative positioning between the aerodynamic center of the wing and the balance is chosen to reduce the torque generated by the wing on the turning table. The offsets between the nose of the model and the balance center are reported in Table 2.9.

The position is identified not to exceed the turning table limits at the test speed of 20 m/s in the angle of attack range between -10 and 55 degrees in order to be able to investigate post-stall characteristics as well, which are not part in this piece of work. Data are collected at a sampling rate of 2 kHz and using a measurement time equal to 10 seconds.

The angles of attack have been defined by aligning the leading edge line of the inboard trunk of the wing with the midpoints of two sections of the outlet of the nozzle of the wind tunnel. The leading edge line of the model can be identified as the junction line between the shells of the suction and pressure sides. The angles are therefore computed with respect to the plane referred as Mid-plane in Fig. 2.15.

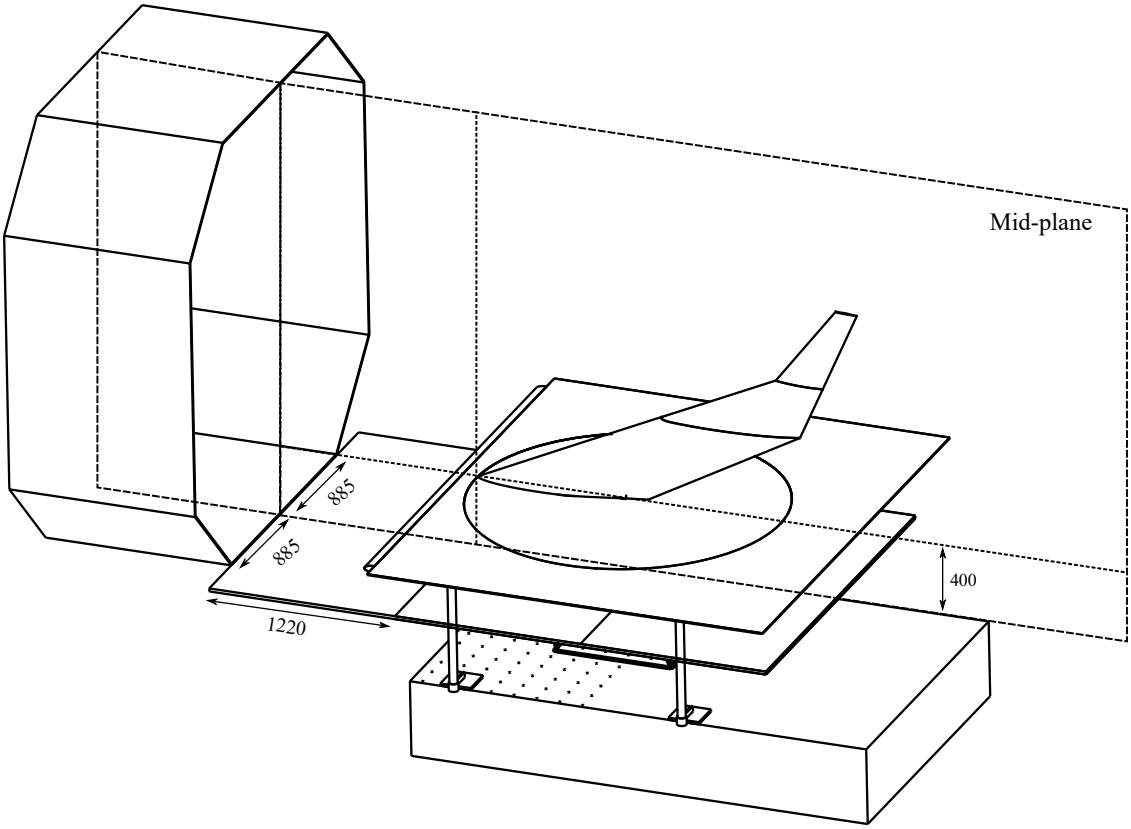

Figure 2.15: Isometric view of the wind tunnel setup. Dimensions in millimeters

2.2.5. Test Conditions

During the wind tunnel campaign, forces and moments without any control surface deflections are recorded in a larger range of geometrical angles of attack, from -10 to 50 degrees, and in an airspeed range from 15 to 31 m/s. The effects of the three control surfaces are collected both by deflecting the control surfaces singularly and mixing them, thus to estimate cross effects as well.

The data used to investigate the static stability and control characteristics of the Flying V scaled model are collected across a geometrical angle-of-attack range from -10 to +35 degrees at 20 m/s, Re $\approx 1\ 10^6$. As suggested by Barlow et al. [15], balance data to estimate stability and control characteristics are measured with transition grits such that transition would occur in a consistent and repeatable manner. The transition grits on the suction side is applied at 5% of the local chord over the entire span. The transition grits on the pressure side is applied at 10% of the local chord over the entire span.

These ranges of angle of attack and speed are selected to quantify the effects of tip stall and of the stalling characteristics of the Flying V. The testing airspeed is selected to be representative of the estimated take-off and landing conditions of the flying model that will be used for sub-scaled flight test activities.

A sample test matrix for the testing of the control surfaces testing is presented in Tab. 2.10.

Table 2.10: Test matrix CS1 and CS2

$\%\delta_{CS2}$	δ_{CS2}	V_∞	α_{min}	α_{max}	$\Delta\alpha$	$\%\delta_{CS1,min}$	$\%\delta_{CS1,max}$	$\delta_{CS1,min}$	$\delta_{CS1,max}$	$\Delta\%\delta_{CS1}$
-125%	-15.2	20	-10	35	5	-125%	125%	-10.5	12.2	25%
-100%	-12.7	20	-10	35	5	-125%	125%	-10.5	12.2	25%
-75%	-9.2	20	-10	35	5	-125%	125%	-10.5	12.2	25%
-50%	-6.5	20	-10	35	5	-125%	125%	-10.5	12.2	25%
-25%	-2.6	20	-10	35	5	-125%	125%	-10.5	12.2	25%
0%	0.0	20	-10	35	5	-125%	125%	-10.5	12.2	25%
25%	3.5	20	-10	35	5	-125%	125%	-10.5	12.2	25%
50%	7.0	20	-10	35	5	-125%	125%	-10.5	12.2	25%
75%	10.3	20	-10	35	5	-125%	125%	-10.5	12.2	25%
100%	14.2	20	-10	35	5	-125%	125%	-10.5	12.2	25%
125%	17.8	20	-10	35	5	-125%	125%	-10.5	12.2	25%

2.3. CFD Simulations

As the designed wind tunnel campaign allows to evaluate the aerodynamic characteristics of the Flying V scaled model without providing almost any information on the local flow characteristics, RANS CFD analyses are performed on a half-wing model to gain a better understanding of the aerodynamic flow over the geometry of the model. The wind tunnel setup is not simulated. The analyses are completed using the commercial software Ansys Workbench 19.1.

In the current section the following activities are presented:

- Generation of the geometry and description of the domain.
- Setup of the numerical grid to perform RANS analyses.
- Setup of the simulations.

2.3.1. Geometry Generation

The geometry of the wing is generated using the *Multi-Model-Generator* KBE application under development at Delft University of Technology. A side view of the virtual domain used for the CFD analyses is presented in Fig.2.16. The origin of the virtual space is located at the nose of the model. Three parallelepipeds are generated around the Flying V model to have better control for refining the mesh close to the wing. The three boxes, from the most inner to the most outer, are extruded of 25, 50, and 200 meters to generate the three-dimensional domain.

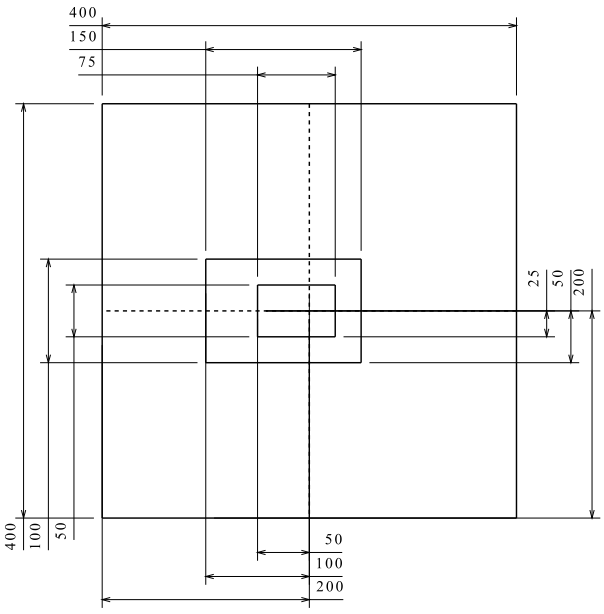

Figure 2.16: Simulation domain. Dimensions in meters.

2.3.2. Grid Setup

The grid is constructed by means of ANSYS® Meshing. The inner volume of the simulation domain is meshed using an unstructured grid. The zone in proximity of the wing are meshed using an inflation layer. Grid density is controlled by means of bodies of influence to slow down the growth of the cells in proximity of the wing. The surface mesh on the wing is presented in Fig.2.18.

The inflation layer zone is meshed by selecting 1st layer thickness, the growing rate and the number of cells. The values are tuned to achieve y+ values lower than one over the wing and a thickness large enough to resolve the entire boundary layer. Fig.2.19 presents an enlargement of the mesh close to the root section airfoil in which the inflation layer is visible. The thickness of the boundary layer is firstly calculated according to the turbulent flat plate solution by Blasius, in Eq. (2.8), at the root and tip of the wing. The y+ is calculated at the tip of the wing, and the number of layers of the inflation layer such that an inflation layer thicker than the root boundary layer is generated. The final y+ value is tuned based on a simulation to achieve y+ values lower than 1 over the entire wing surface. A y+ value equal to $5 \cdot 10^{-6}$ meters is selected, 40 layers, and a growing rate equal to 1.2.

$$\delta \approx \frac{0.37c}{\mathrm{Re}^{0.2}} \tag{2.8}$$

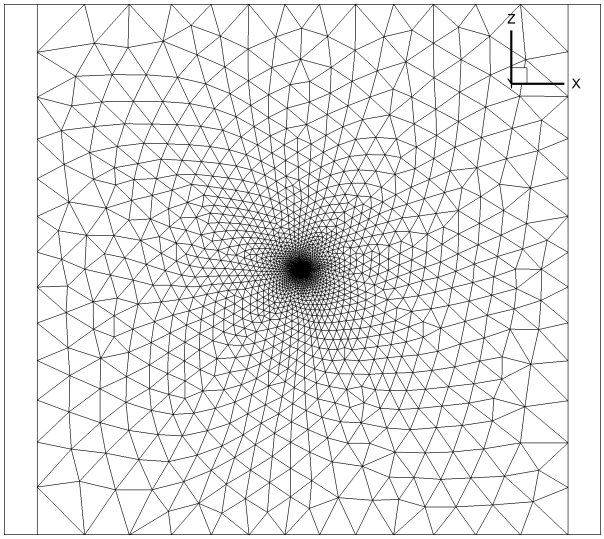

Figure 2.17: Mesh side view.

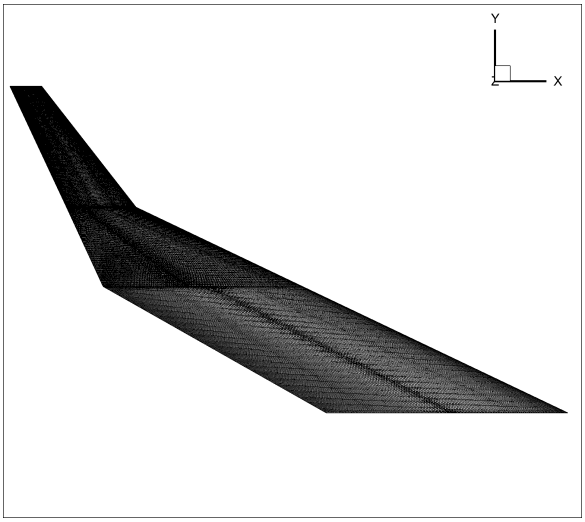

Figure 2.18: Wing surface mesh. Top view. Flow direction from right to left.

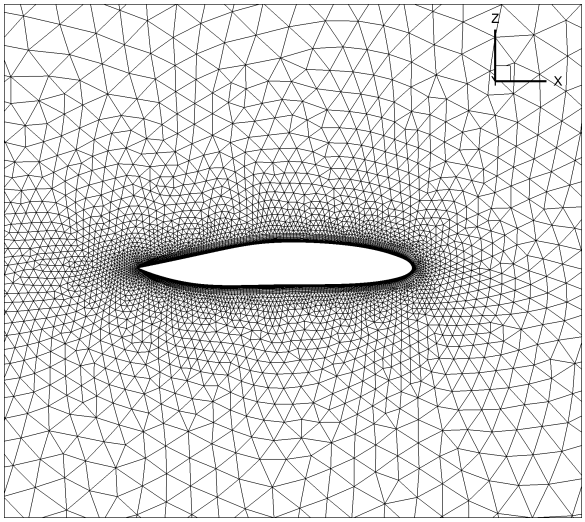

Figure 2.19: Root airfoil mesh. Side view. Flow direction from right to left.

By taking advantage of the possibility of generating polyhedral meshes in ANSYS® Fluent, three different meshes are generated to perform the CFD simulations. Polyhedral elements, with respect to tetrahedral elements, enhance better capability in calculating gradients thanks to the greater number of faces [33]. The characteristics of the mesh are reported in Table 2.12. Grid 1 is an unstructured mesh composed of tetrahedrons and wedges. Grid 2 is an unstructured grid composed of polyhedrons which is converted from Grid 1. Grid 3 is a refined version of Grid 2 composed of polyhedrons. The inflation layers are converted to polyhedral elements as well.

2.3.3. Simulation Setup

The outer faces of the mesh are grouped as presented in Fig.2.20. The applied boundary conditions are presented Table 2.13.

Table 2.11: Wing and Volume Meshing Discretization.

Grid	Number of Points Chordwise	Number of Points Spanwise	Growth Rate
1	150	450	1.05
2	150	450	1.05
3	200	600	1.05

Table 2.12: Grids Specifications.

Grid	Element Topology	Number of Cells	Number of Faces	Number of Nodes
1	Tetrahedrons/Wedges	$10.50 \cdot 10^6$	$25.30 \cdot 10^6$	$4.78 \cdot 10^6$
2	Polyhedrons	$9.46 \cdot 10^6$	$42.18 \cdot 10^6$	$25.16 \cdot 10^6$
3	Polyhedrons	$14.49 \cdot 10^6$	$63.84 \cdot 10^6$	$37.30 \cdot 10^6$

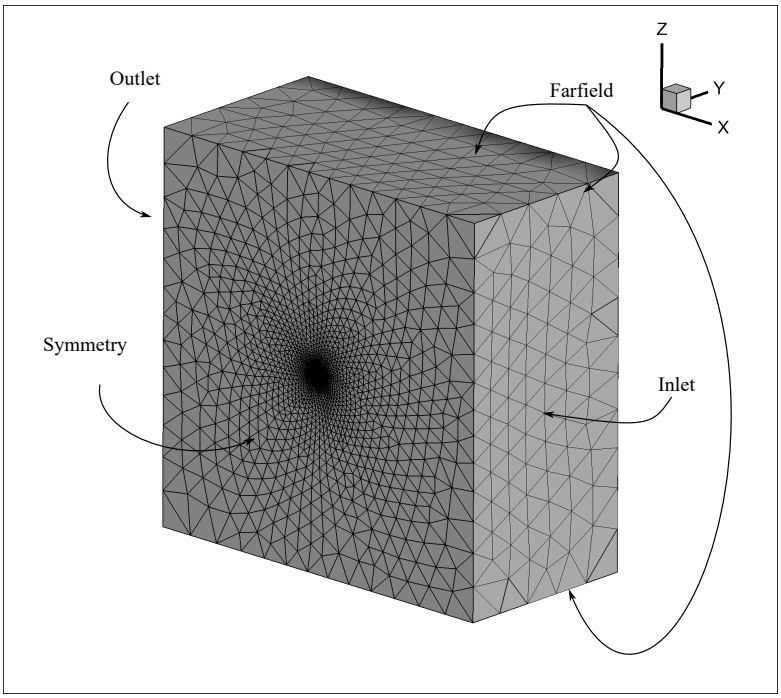

Figure 2.20: Mesh boundary conditions.

Table 2.13: Applied boundary conditions.

Name group	Boundary condition	Flow direction components	Velocity magnitude
Inlet	Velocity inlet	$(\cos\alpha, 0, \sin\alpha)$	V_∞
Farfield	Velocity inlet	$(\cos\alpha, 0, \sin\alpha)$	V_∞
Outlet	Pressure outlet		
Sym	Symmetry		
Wing	Wall (no-slip, no roughness)		

As the simulations are representative of iposonic conditions, free stream Mach number about 0.06, the energy equation is deactivated to reduce the computational effort. *Air* is chosen as fluid material. The density and viscosity values are modified to match the data registered during the wind tunnel campaign. Density is set

equal to 1.2024 [kg/m^3]. Viscosity is set to 1.5594 10^{-5} [kg/(ms)].

Spalart-Almaras one equation eddy viscosity model [34] is selected to model turbulence according to the good predictions by Huber et al. [35] on lift, drag and pitching moment characteristics at a relatively low computational cost. The *Strain/Vorticity-Based* production term incorporated in ANSYS® Fluent, proposed by Dacles-Mariani et al.[36], and *Curvature correction* options are used to prevent build-up of turbulence viscosity in vortex cores [37]. Based on the considerations by Spalart [38], the turbulent viscosity ratio is set to 3 at the boundaries of the domain to achieve fully turbulent behavior of the flow.

Second order schemes are used for the discretization of all the flow variables. The *Pseudo Transient* formulation is used to calculate the solution as it has been found to speed up convergence [39]. Standard initialization from inlet boundary conditions is used for the initialization of the flow-field.

2.4. Flight Mechanic Framework

This section describes:

- The methodology applied for the development of the trim algorithm.
- An explaination of the optimization routine developed to identify the optimal location of a statically stable Flying V model.

2.4.1. Development of the Trim Algorithm

The Flying V configuration is representative of a vehicle with *multi-redundant control surfaces* [40]. Such a vehicle configuration presents the possibility of performing control allocation studies to identify the best control strategies to perform maneuvers or trim analyses.

A trim algorithm is developed in MATLAB environment to perform longitudinal trim analyses of the Flying V configuration using the two inner control surfaces in different flight conditions. The trim algorithm is formulated using the *fmincon* function of MATLAB. The algorithm gets as input the mass of the aircraft, angle of climb, flight speed and the processed data from the wind tunnel experiments.

By making use of the wind tunnel data, the algorithm can therefore evaluate the mutual effects between the two control surfaces induced by different deflections of the control surfaces. The angle of attack of the aircraft, α, and the deflections of the two used control surfaces, δ_{CS1} and δ_{CS2}, are used as control variables to look-up into the wind tunnel data and are modified by the non linear programming solver to achieve equilibrium in the Body axes of the aircraft centered in the selected center of gravity location.

$$\bar{x} = [\alpha; \delta_{CS1}; \delta_{CS2}] \tag{2.9}$$

The deflections of the two control surfaces are primarily used to influence the pitching moment of the aircraft while the angle of attack is used to influence the lift. The influence of the control surfaces on the produced lift is taken into account as well. The horizontal force is estimated but not taken into account during the trim estimation since the available wind tunnel data are representative of the power-off configuration.

As described by Garmendia [40], a failure to find a trim solution can happen due to three reasons: insufficient control authority, or poor initial guesses or too strict tolerances. The options of fmincon are tuned for tolerances. To overcome the poor initial guess possibility, the trim algorithm starts trimming the aircraft at high

airspeed conditions and it gradually reduces the speed making use of the previous solution as initial guess for the lower airspeed. This approach allows to identify when insufficient control authority cases take place or when other constraints, such as static stability margin requirements, are not satisfied.

The achievement of equilibrium conditions is formulated using residuals in equality or inequality constraints.

$$R_{F_z} = \frac{q_\infty S_{\text{Ref}} C_z(\alpha, \delta_{CS1}, \delta_{CS2}) + W\cos(\gamma)}{W\cos(\gamma)} \tag{2.10}$$

$$R_{M_y} = C_M(\alpha, \delta_{CS1}, \delta_{CS2}) \tag{2.11}$$

When more control authority than required by the flight condition is available on multi-redundant control surfaces vehicles, the equilibrium equations present more control parameters than unknowns thus allowing an infinite number of solution. To overcome this possibility, an optional equality constraint is defined to set a fixed gain between the two control surfaces. The gain is referred as *control surface deflection ratio* (CSDR) and it is presented in Eq. (2.12). The optional constraint can be used by the trim algorithm to set a constant gain between the used control surfaces is presented in Eq. (2.15). The use of CSDR reduces the number of control parameters from three to two as a relationship between the two control surfaces is set. This approach reduces the number of control parameters influencing the system of equations formed by Eq. (2.10) and (2.11) from three to two: by formulating the trim problem using CSDR to fix the ratio between the deflections of the available control surfaced, the solution of the trim problem can either exist, and be unique, or not be feasible.

$$\text{CSDR} = \frac{\delta_{CS2}}{\delta_{CS1}} \tag{2.12}$$

The constraints used to ensure equilibrium and stability are hereafter presented. The static stability constraint can be deactivated to perform analysis on the unstable configuration.

$$c_{\text{in}_1} = C_{M_\alpha} - C_{M_\alpha}\big|_{Ref} < 0 \tag{2.13}$$

$$c_{\text{eq}_1} = {R_{F_z}}^2 + {R_{M_y}}^2 = 0 \tag{2.14}$$

$$c_{\text{eq}_2} = \delta_{CS1} - \text{CSDR}\cdot\delta_{CS2} = 0 \tag{2.15}$$

2.4.2. Identification of the Optimal Center of Gravity Location for a Statically Stable Model

An optimization routine is developed to identify the optimal position of the center of gravity for flying wings to maximize the max trimmed lift coefficient while ensuring trimmability within the entire range of angle of attack from the zero lift angle of attack to the maximum lift angle of attack. The routine makes use of the previously presented trim algorithm. The optimization routine assumes the available control surfaces to be working as pure elevators.

The idea behind the proposed optimization is to find the location of the center of gravity that ensures an optimal use of the deflections of the control surfaces. Shifting the center of gravity induces a variation in C_{M_α} value. Low C_{M_α} values cause the use only of positive deflections to trim the aircraft up to the maximum angle of attack. High C_{M_α} values limit the maximum angle of attack because of lack of control authority.

The optimization routine is formulated as follows:

$$\min -C_{L_{\text{Max}}} = f(x_{\text{CoG}}, \delta_{\text{CS1}}, \delta_{\text{CS2}}, \alpha) \tag{2.16}$$

Subject to:

$$c_1 = C_{M_\alpha}\big|_{C_{L_{\text{Max}}}} < C_{M_\alpha}\big|_{\text{Ref}}, @\delta_{\text{CS1}}, \delta_{\text{CS2}} \text{ full-up} \tag{2.17}$$

$$c_2 = -C_M\big|_{C_{L_{\text{Max}}}} < 0, @\delta_{\text{CS1}}, \delta_{\text{CS2}} \text{ full-up} \tag{2.18}$$

$$c_3 = -C_M\big|_{C_L=0} < 0, @\delta_{\text{CS1}}\delta_{\text{CS2}} \text{ full-up} \tag{2.19}$$

$$c_4 = C_{M_\alpha}\big|_{C_{L_{\text{Max}}}} < C_{M_\alpha}\big|_{\text{Ref}}, @\delta_{\text{CS1}}, \delta_{\text{CS2}} \text{ full-down} \tag{2.20}$$

$$c_5 = C_M\big|_{C_{L_{\text{Max}}}} < 0, @\delta_{\text{CS1}}, \delta_{\text{CS2}} \text{ full-down} \tag{2.21}$$

$$c_6 = C_M\big|_{C_L=0} < 0, @\delta_{\text{CS1}}, \delta_{\text{CS2}} \text{ full-down} \tag{2.22}$$

Eq. (2.17) and (2.20) are required to ensure longitudinal static stability at the maximum lift coefficient both with control surfaces deflected upwards and downwards. Eq. (2.18) ensures that the pitching moment of the aircraft is greater than zero when flying at maximum lift coefficient in steady state horizontal flight, this constraint naturally converges to zero when coupled with the others, an inequality constraint was still preferred to an equality constraint. Eq. (2.21) ensures the aircraft controls are still effective for positive deflections and can produce a pitching-down moment to reduce the angle of attack when flying at maximum lift coefficient in steady state horizontal flight. Eq. (2.19) and (2.22) ensure the aircraft can be trimmed at the zero lift coefficient in steady state horizontal flight.

3

Verification and Validation

The following verification and validation activities are performed:

- The repeatibility of the wind tunnel data is validated using two dataset.
- The CFD methodology is verified by:
  - Analyzing the mesh quality of the grid based on three mesh metrics: skewness, maximum corner angle, and orthogonal quality.
  - Definining the convergence criteria based on the analysis of the convergence history of a test simulation.
  - Presenting the max y+ distributions from all the performed simulations to validate the boundary layer is solved.
- A comparison between wind tunnel and CFD aerodynamic characteristics of the model is presented.

3.1. Wind Tunnel Data Repeatibility Analysis

Short term repeatibility is assessed by comparing different dataset collected on the same day during the wind tunnel campaign. Two datasets related to the deflections of the third control surface have been repeated to assess the repeatibility of the effects of control surfaces on the wing. The repeated measurements are collected at an airspeed equal to 20 m/s. The first repeated dataset, Dataset 1, is representative of model polar between -10 and 35 degrees, at each angle of attack a complete sweep of deflections is performed on the third control surface, the second control surface is hold at -6.5 degrees. The first dataset is made of 220 measurements, 110 per repetition. The second repeated dataset, Dataset 2, is representative of model polar between -10 and 20 degrees, at each angle of attack a complete sweep of deflections is performed on the third control surface, the second control surface is hold at -9.2 degrees. The second dataset is made of 140 measurements, 70 per repetition.

The deviations are computed per each dataset with respect to the average value. The deviations are used as population to evaluate confidence intervals [41] using T-Student distributions assuming nor the angle of

attack or the control surface deflection influenced the quality of the measurements. Four horizontal lines are presented in the deviation plots, these are indicative of the 95%, dashed line, and 99%, dot-dashed line, confidence intervals. The confidence intervals related to Fig.3.1 are reported in Tab.3.1. The confidence intervals related to Fig.3.2 are reported in Tab.3.2. All the confidence intervals reported in the presented tables are presented in counts, $1 \cdot 10^{-4}$.

The deviations of each dataset are presented in Fig. 3.1 and 3.2. The pitching moment deviations of both the dataset appear to be less precise at 15 degrees, which might indicate to the onset of unsteady aerodynamic phenomena. Lowered precision of the measurements is present on the data from Dataset 1 at 30 and 35 degrees on the deviations of the pitching moment, lift coefficient, and drag coefficient. Both the dataset present lower repeatibility at 10 and 20 degrees angle of attack on the drag coefficient.

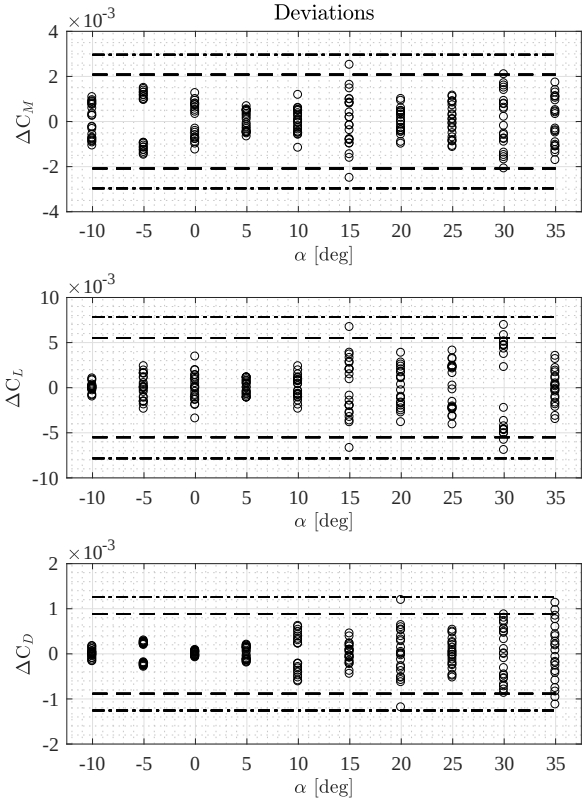

Figure 3.1: Data repeatibility. Dataset 1.

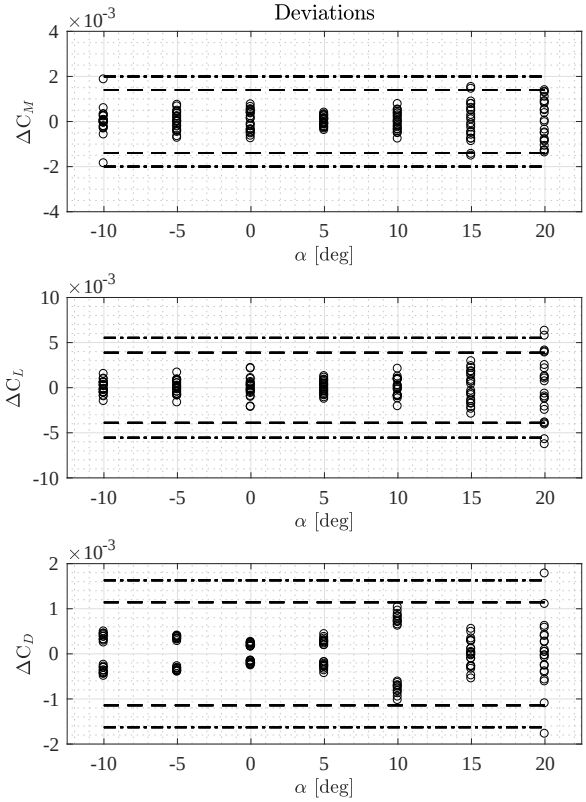

Figure 3.2: Data repeatibility. Dataset 2.

Table 3.1: Confidence intervals of Dataset 1. Relative to Fig.3.1. Values reported in counts.

	Confidence intervals	
	$\rho_{95\%}$	$\rho_{99\%}$
C_M	21	30
C_L	55	78
C_D	8.8	13

Table 3.2: Confidence intervals of Dataset 2. Relative to Fig.3.2. Values reported in counts.

	Confidence intervals	
	$\rho_{95\%}$	$\rho_{99\%}$
C_M	14	20
C_L	39	55
C_D	11	16

Based on 99% confidence intervals presented in Table 3.1, the precision in terms of lift and drag forces, and pitching moment are evaluated at the reference test conditions which presented a dynamic pressure about 240 Pascal and the reference dimensions presented in Table 2.3. An accuracy of the measurements equal to 0.55 Nm is calculated on the pitching moment. An accuracy of the measurements equal to 1.75 N is calculated on the lift force. An accuracy of the measurements equal to 0.29 N is calculated on the drag force.

3.2. Verification and Validation of the Numerical Investigations

3.2.1. Quality Assessement of the Tetrahedral Grid

The generated grid presents 150 elements in spanwise direction per each of the three trunks of the wing and 120 elements in chordwise direction on the suction and on the pressure side. Although no grid convergence study is performed on the mesh, different meshes have been generated and the setup parameters have been tuned to improve the quality of the mesh as much as possible. The quality of the final grid is hereafter presented, the grid features about 4.8 millions nodes and 10.5 millions cells. The skewness, maximum corner angle [42], orthogonal quality [43] metrics are calculated to assess the quality of the mesh.

As observable in Fig. 3.3, the elements of the grid are mostly concentrated in proximity of the wing, the size of the tetrahedral elements of the grid increases away from the wing. Fig. 3.3 presents three iso-surfaces of the mesh at three different cell volume levels equal to 10^-9, boundary layer cells, 0.01, and 0.1 m^3.

The "Diagonal Skewness 1" and "Diagonal Skewness 2" metrics are presented from Fig. 3.4 to Fig. 3.7. These metrics are calculated in TECPLOT and their mathematical meaning is given by Eq. (3.1). Low skewness values imply the diagonals are similar so the cells are not skewed. Indications on skewness quality are provided in Table 3.3.

As presented in Fig. 3.4 and 3.6, the most of the elements of the grid present a quality from good to excellent according to the indications provided by Ansys [3]. The cumulative distributions of elements are presented in Fig. 3.5 and 3.7, from these it is observable that about the 93% of the elements of the grid present skewness values lower than 0.50. Only the 7% of the elements of the mesh present a quality between fair and bad: about the 5.5% of the elements presents a fair skewness cell quality, and about the 1.5% presents poor skewness cell quality. The presence of a small amount of cells with lower quality in 3D meshes is reported by Ansys *"In 3D meshes, most cells should be rated good or better, but a small percentage will generally be in the fair range and there are usually even a few poor cells [...]"* [3].

$$\text{Diagonal Skewness} = 1 - \frac{\text{Length shorter diagonal}}{\text{Length longer diagonal}} \tag{3.1}$$

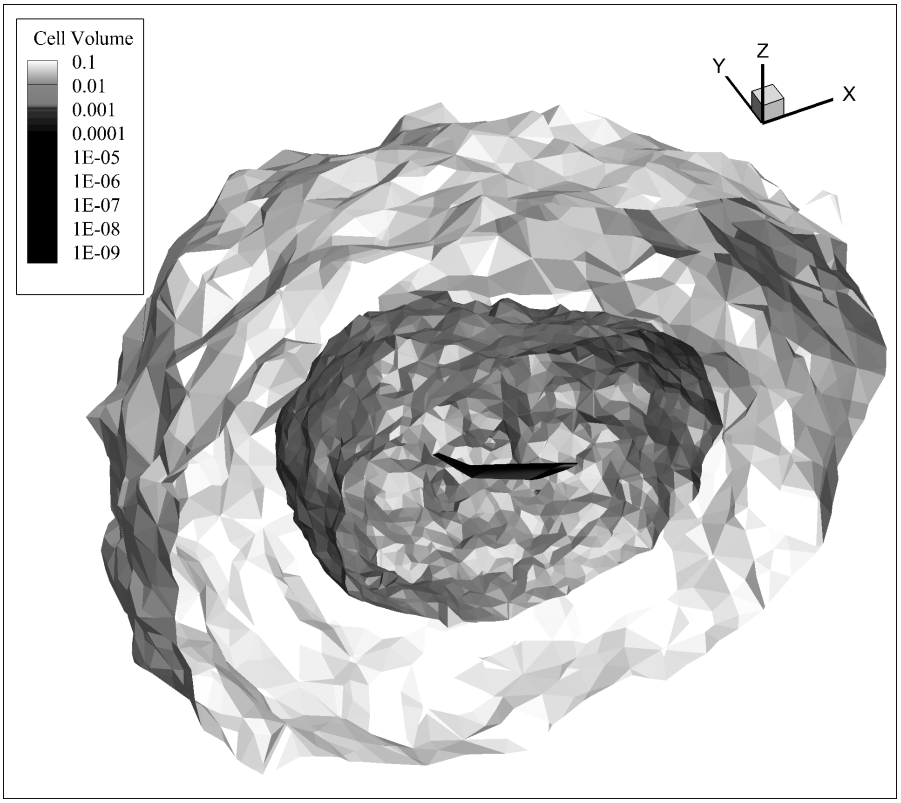

Figure 3.3: Grid isosurfaces at cell volume levels equal to 10^{-9}, 0.01, and 0.1 m^3.

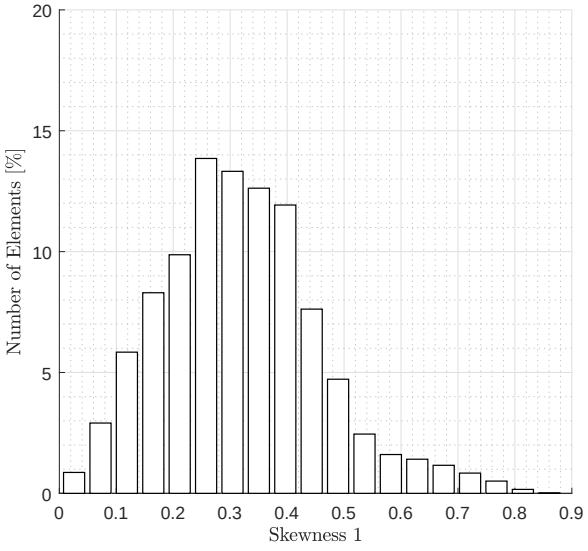

Figure 3.4: Metrics distribution. Diagonal Skewness 1.

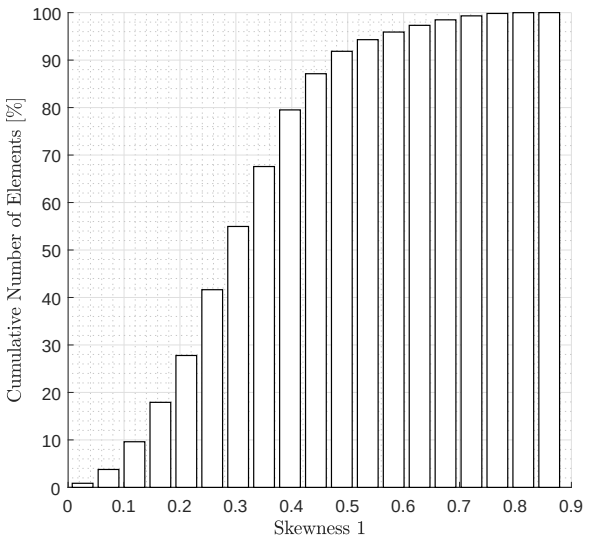

Figure 3.5: Metrics cumulative distribution. Diagonal Skewness 1.

Table 3.3: Skewness Ranges and Cell Quality [3].

Skewness range	Cell Quality
1	Degenerate
0.9 <1	Bad
0.75 – 0.9	Poor
0.5 – 0.75	Fair
0.25 – 0.5	Good
0 – 0.25	Excellent
0	Equilateral

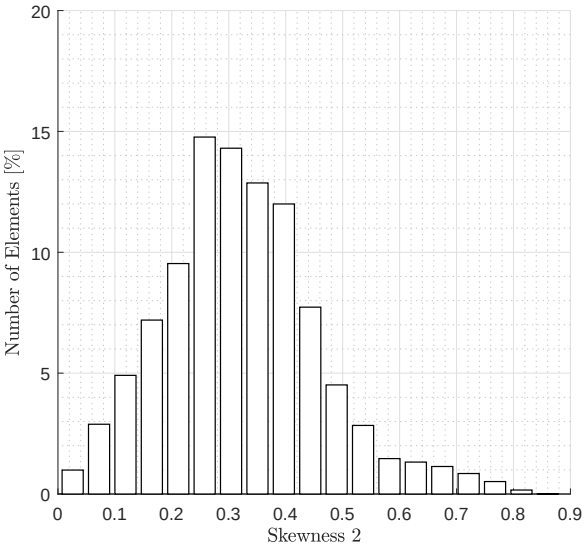

Figure 3.6: Metrics distribution. Diagonal Skewness 2.

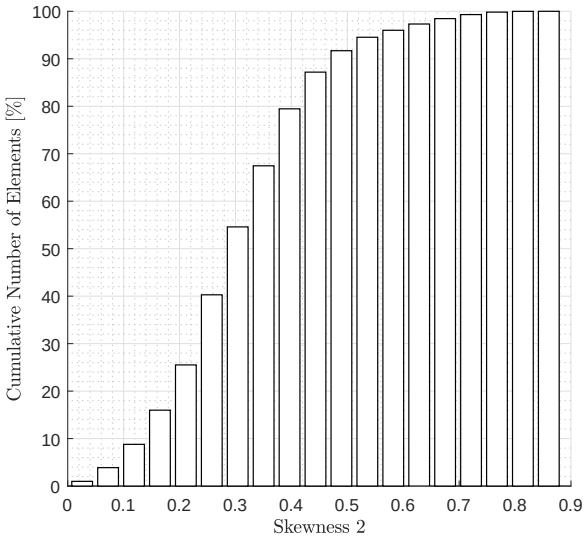

Figure 3.7: Metrics cumulative distribution. Diagonal Skewness 2.

The maximum corner angle metrics are presented in Fig. 3.9 for the wedge elements, used for meshing the inflation layer, and in Fig. 3.10 for the tetrahedral elements, used for meshing the rest of the domain. The maximum angle is computed using the edges of each element. For tetrahedrons, the best possible maximum angle is 60 degrees as it means the faces of the element is made of equilateral triangles. Good practice is to keep the maximum corner angle lower than 160 degrees. The effects of high maximum angles are presented in Fig. 3.8.

The orthogonal quality metrics is presented in Fig. 3.11 for the wedge elements, used for meshing the inflation layer, and in Fig. 3.12 for the tetrahedral elements, used for meshing the rest of the domain. Recommendations about the mesh quality [4] suggest to try to keep minimum orthogonal quality greater than 0.1. The reference values of the orthogonal quality mesh metrics and the relative cell quality are presented in Table 3.4.

The orthogonal quality metrics distribution relative to the tetrahedral elements presents values greater tha 0.2, which indicates a good cell quality in Table 3.4. The orthogonal quality metrics distribution relative to the wedge elements ranges between 0 and 1. About the 2% of the wedge elements presents orthogonal quality values lower than 0.125, indicating those cell having poor quality. About the 4% of the wedge elements ranges in an acceptable cell quality value, while the remaining 94% present a grid quality between good and

excellent, according to Table 3.4.

As Ansys Meshing is used for the generation of the grid, and modifications in grid setup have global impact on the entire generated mesh which might lead to reduction of mesh quality, the presented mesh is considered to be sufficient.

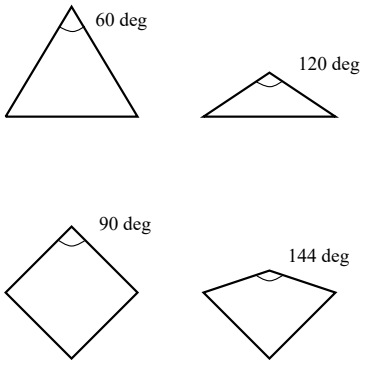

Figure 3.8: Effects of large Maximum Corner Angles on faces geometry.

Table 3.4: Orthogonal Quality mesh metrics spectrum [4].

Skewness range	Cell Quality
0.95 - 1.00	Excellent
0.7 - 0.95	Very good
0.20 - 0.69	Good
0.15 - 0.20	Acceptable
0.001 - 0.14	Bad
0 - 0.001	Unacceptable

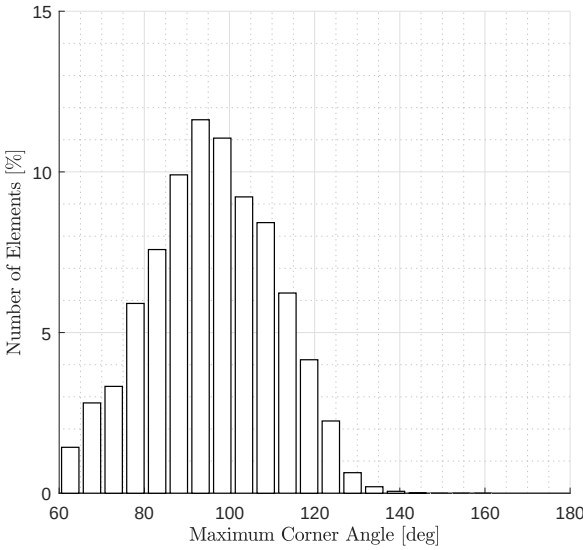

Figure 3.9: Metrics distribution. Maximum Corner Angle. Wedge elem.

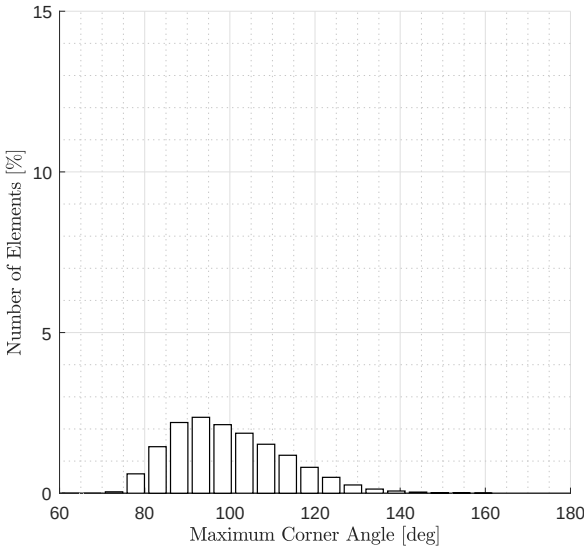

Figure 3.10: Metrics distribution. Maximum Corner Angle. Tetra elem.

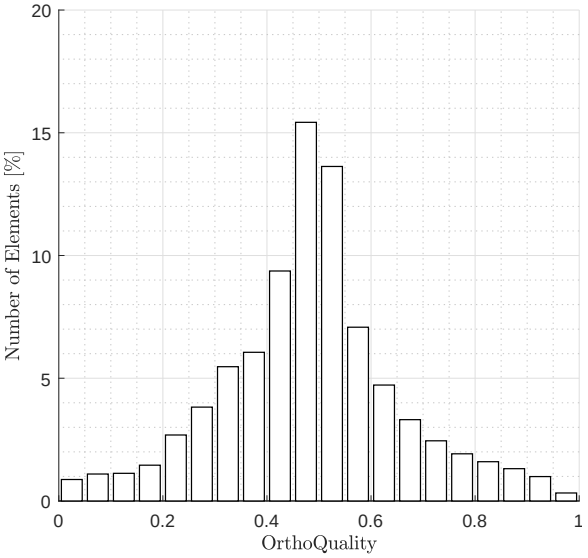

Figure 3.11: Metrics distribution. Orthogonal Quality. Wedge elem.

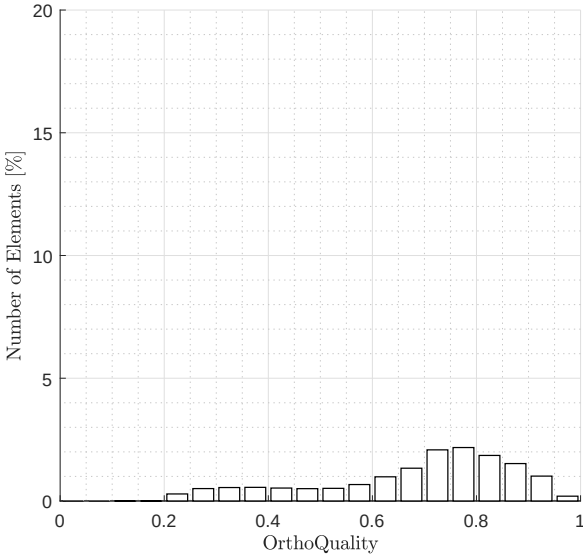

Figure 3.12: Metrics distribution. Orthogonal Quality. Tetra elem.

3.2.2. Definition of the Convergence Criteria

To define the convergence criteria, a simulation of the wing is performed at 20 degrees, such that 3D aerodynamic phenomena over the wing are present and the convergence criteria can be considered valid both at low and high angles of attack. The simulation is performed using the pseudo-transient method. The simulation is stopped when the residual of the continuity equation converges to a constant value. The residuals, the forces in x and z directions, and the pitching moment values are monitored during the test simulation.

As the residuals do not give a clear indication about the error of the solution, which has not been calculated, the error on the monitored forces and moments acting on the wing is computed as presented in Eq. (3.2). In Eq. (3.2), F^{i-th} is the force or moment acting on the wing evaluated at the iteration i-th, F^{end} is the force or moment acting on the wing at the last solved iteration. Therefore, the error is computed with respect to 1.0001 such that when the force, or moment, at the iteration i-th approaches the final value the error becomes equal to 10^{-4} and the convergence of forces and moments can be easily recognized on a semi-logaritmic scale.

$$\varepsilon = \left| 1.0001 - \frac{F^{i-th}}{F^{end}} \right| \tag{3.2}$$

The convergence history of the residuals and of the monitored forces and moments are presented in Fig. 3.13 and 3.14. The continuity equation residual, which is normalized [44], achieves a constant values at 4 10^{-5}. The turbulent eddy viscosity residual converges to values equal to 6.8 10^{-8}. The residuals of the three velocities continues on decreasing to values lower than 10^{-11}. The errors in Fig. 3.14 highlight that converged values of forces and moments are achieved after about 200 iterations at which, as example, the residual of the continuity equation is equal to 3 10^{-3}.

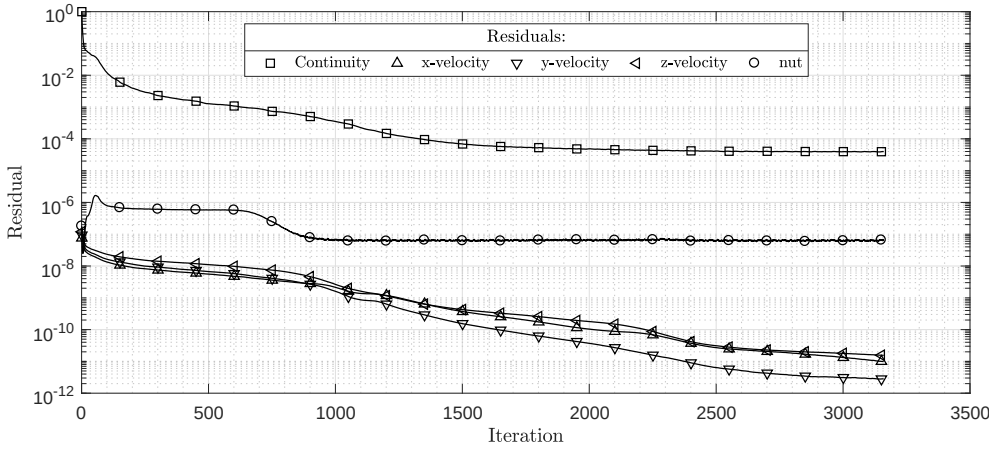

Figure 3.13: Convergence history of the test simulation for the definition of the convergence criteria.

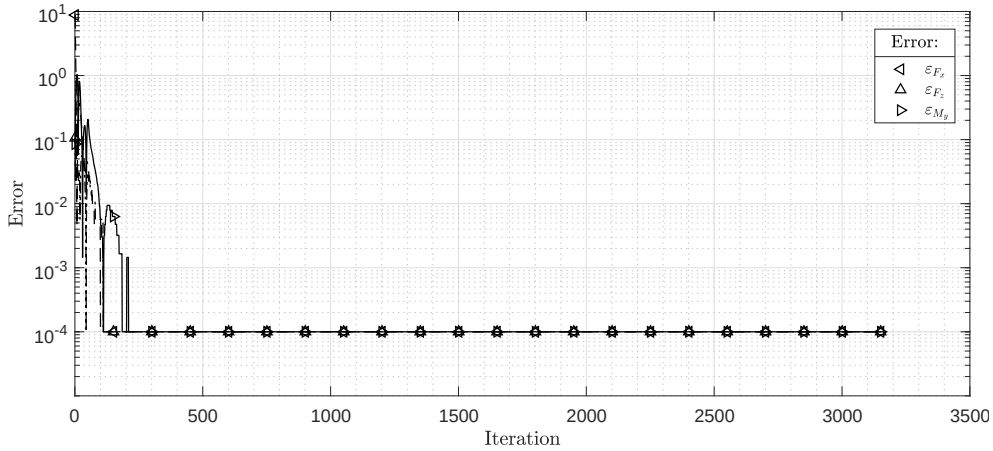

Figure 3.14: Convergence history of the test simulation for the definition of the convergence criteria.

Based on the previous considerations, all the performed simulations are considered converged when:

- The values of the monitored forces and moments converge to a constant value;
- The residual of the continuity equation is at least equal to 10^{-3};
- The total mass flux on the boundaries of the mesh converges to values lower than 10^{-5} kg/s.

3.2.3. Y+ Verification

As last check, the maximum values of y+ on longitudinal sections of the wing are analyzed. The Spalart-Allmaras turbulence model required y+ values about one to properly resolve the laminar sub-layers without making use of wall-functions. The maximum values of y+ are extracted from the results and presented as spanwise distributions in Fig. 3.15, relative to Grid 1, Fig. 3.16, relative to Grid 2, and Fig. 3.17, relative to Grid 3.

As observable in the distributions presented in Fig. 3.15, y+ values lower than 1 are always achieved for each simulation. Lower values of y+ are present in the inboard part of the wing as the height of the first cell of the inflation layer is calculated using the tip chord as reference. The local increments of y+ values in spanwise

direction for $\eta \in [0, 0.6]$ are caused by the presence of vortical structures. In vortical structures, larger velocities than the free-stream velocity used to compute the height of the first cell take place thus, as the height of the first cell is inversely proportional to the speed, the height of the first cell shall be lowered in those zones. The use of the smallest chord of the wing for calculating the height of the first cell in proximity of the wing has allowed to achieve y+ values lower than 1 also in high speed regions of the simulated flowfield.

In Fig. 3.16 and 3.17, few spanwise location at which y+ values slightly greater than one are present. Although these local y+ values greater than one are identified, Grid 2 and Grid 3 are accepted as the maximum y+ values are found to be close to the unitary value. Furthermore, Grid 2 and Grid 3 are automatically converted from tetrahedral elements to polyhedral elements by Ansys Fluent and no control is available on the conversion which might slightly influence the first layer height in some zone of the grids.

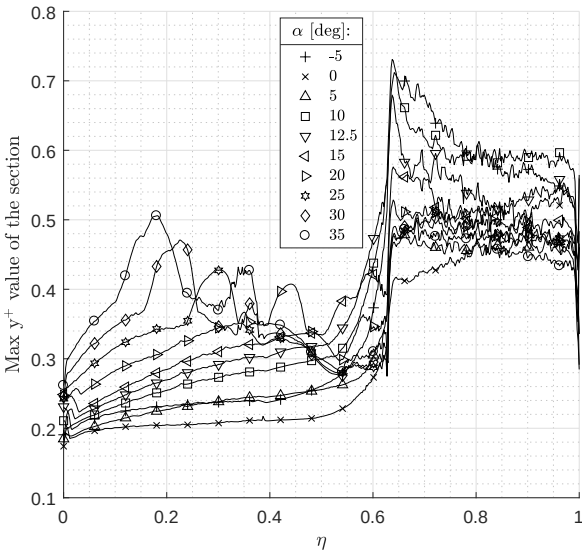

Figure 3.15: Max Y+ spanwise distribution. Grid 1.

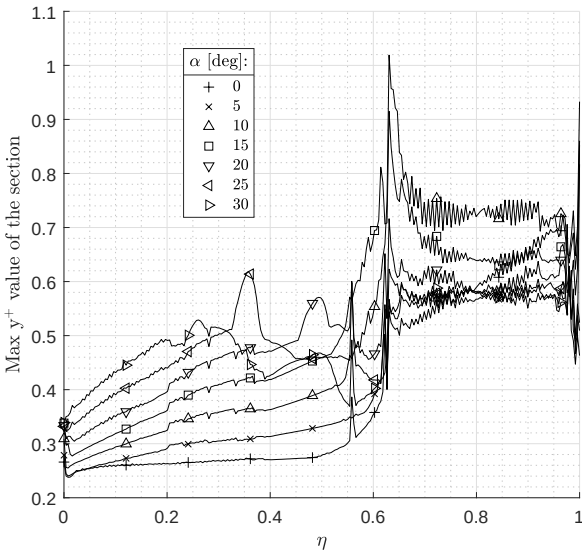

Figure 3.16: Max Y+ spanwise distribution. Grid 2.

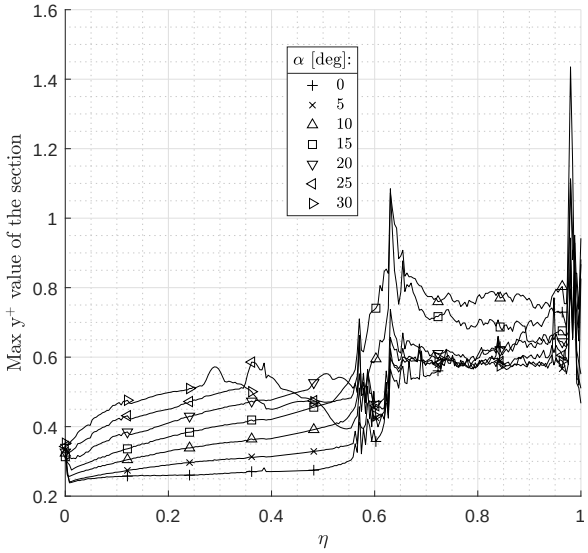

Figure 3.17: Max Y+ spanwise distribution. Grid 3.

3.2.4. Grid Dependency Study

The comparison of the lift, drag, and pitching moment coefficients with respect to the angle of attack from the three used meshes are presented in Fig. 3.18, 3.20, and 3.22. In terms of lift and drag characteristics, the results from Grid 1, Grid 2, and Grid 3 are mesh independent up to 10 degrees. This is also presented in Fig. 3.19 and 3.21 in which the deviations of the lift and drag coefficients of the three meshes with respect to their average are presented. The largest deviations of the lift coefficient and of the drag coefficient in the angle of attack range from 0 to 10 degrees is lower than 40 counts. For angles of attack larger than 15 degrees the deviations increase and follow different trends for the three used grids, still the maximum deviation relative to the lift coefficient curves is smaller than 360 counts, while the maximum deviation relative to the drag coefficient curves is lower than 100 counts.

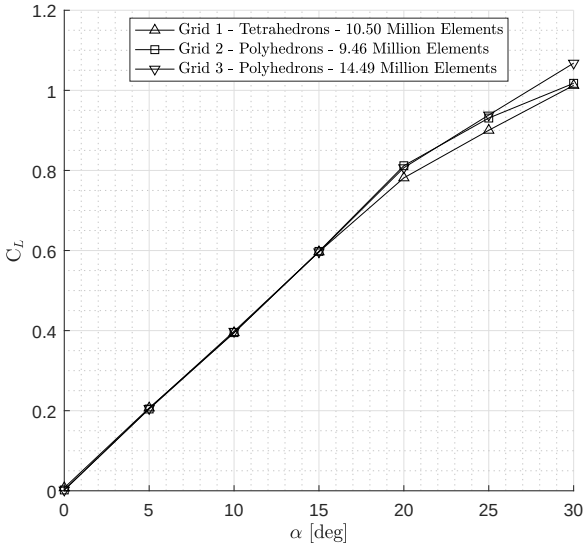

Figure 3.18: Grids comparison.
C_L - α curve.

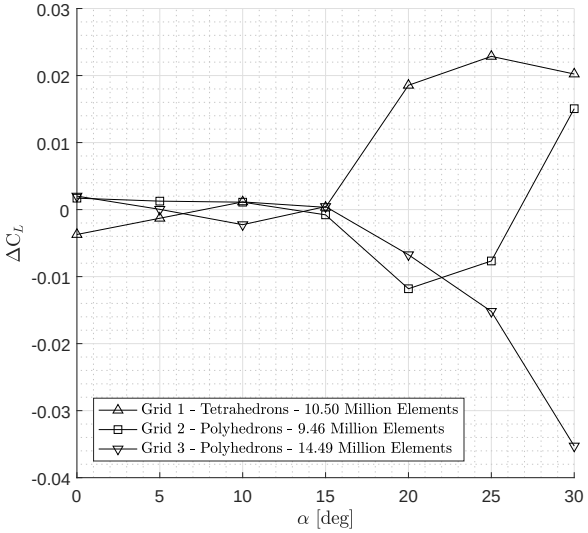

Figure 3.19: Grids comparison.
ΔC_L - α curve.

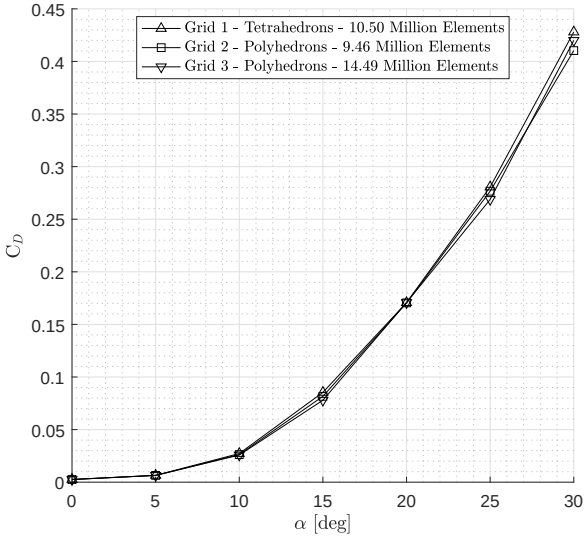

Figure 3.20: Grids comparison.
C_D - α curve.

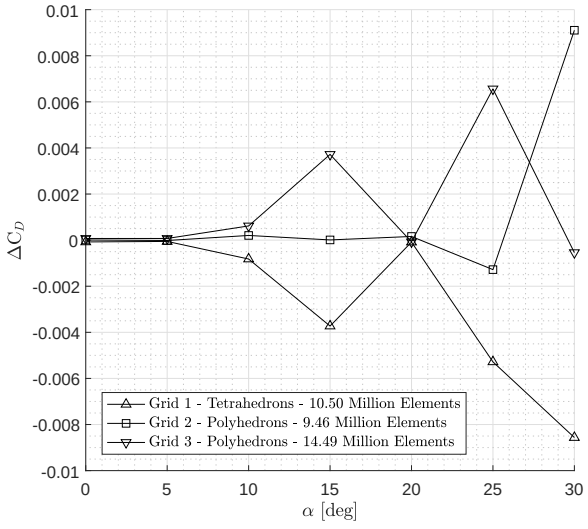

Figure 3.21: Grids comparison.
ΔC_D - α curve.

Differently from the lift and drag characteristics, the pitching moment characteristics estimated by making use of the CFD analyses are more dependent on the grid, especially at angles of attack larger than 15 degrees. The pitching moment coefficient is evaluated with respect to the leading edge point of the mean geometric chord of the investigated configuration. In the angle of attack range from 0 to 10 degrees, the pitching moment estimated is almost grid independent as observable in Fig. 3.22 and 3.23. For angles of attack larger than 15 degrees, the discrepancies between the pitching moment coefficients from the three grids become of the same order of magnitude of the pitching moment at zero angle of attack. A different behavior between the tetrahedral and polyhedral grids can be observed at 15 degrees angle of attack: the tetrahedral mesh at 15 degrees is already predicting a pitch-up break tendency, the polyhedral meshes predict the configuration is stable up to 20 degrees, angle of attack at which pitch-up break tendencies are identified. In general, the tetrahedral grid predicts the configuration experience a pitch-up break tendency already at angles of attack about 10 degrees. On the other hand, the polyhedral grids predicts the pitch up tendency to take place at 20 degrees angle of attack and similar slope of the curves is present between 20 and 25 degrees.

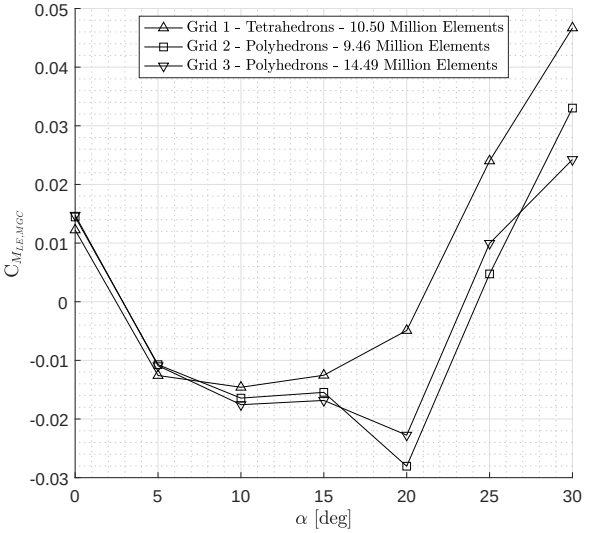

Figure 3.22: Grids comparison. C_M - α curve.

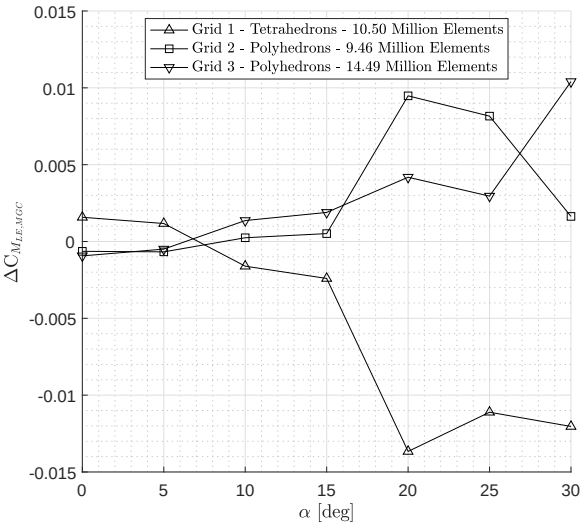

Figure 3.23: Grids compamrison. ΔC_M - α curve.

To recap, the lift coefficient and drag coefficient curves evaluated with the three grids present similar trends and discrepancies lower than 50 counts up to 15 degrees. The pitching moment characteristics of the configuration present are in good agreement up to 10 degrees angle of attack independently of the grid characteristics, the number of elements and the topology of the elements. For angles of attack larger than 10 degrees, larger discrepancies take place by comparing the results from the three grids. In particular, a similar trend is identified between Grid 2 and Grid 3 highlighting a dependency on the topology of the elements of the grid. The latter dependency can be related to the different prediction capabilities between tetrahedral elements and polyhedral elements in predicting highly the highly vortical flow which develops over the wing from 15 degrees onwards. A dependency of the CFD simulations on the estimated pitching moment is still present, however the pitch-up break tendency is predicted to take place at 20 degrees both from Grid 2 and Grid 3.

3.2.5. Comparison of Computational and Experimental Results

The polars obtained from wind tunnel testing and from the CFD simulations are hereafter compared. Both the wind tunnel and CFD flows present a free-stream velocity equal to 20 m/s and a Reynolds number about

to $1 \cdot 10^6$. The values of the aerodynamic forces and moments from the CFD simulations are computed by performing surface integrals in TECPLOT®.

The comparison of the lift characteristics is presented in Fig. 3.24. The CFD results reproduce the trend of the data collected during the wind tunnel campaign. The discrepancies consist in a slightly larger α_{Z_L}, a greater C_{L_α}, and an overprediction of lift at very high angles of attack of the CFD simulations with respect to the wind tunnel data. The α_{Z_L} extracted from the wind tunnel experiments is about -1 degree, while CFD results predict a zero lift angle of attack about 0 degrees. The results from Grid 2 at 30 degrees angle of attack highlight a reduction in slope of the lift coefficient curve.

The comparison of the drag characteristics is presented in Fig. 3.25. By comparing the drag characteristics at same angle of attack CFD simulations underpredict drag at angles of attack lower than 20 degrees and overpredict drag for angles of attack larger than 20 degrees. A discrepancy about 80 drag counts is present at zero degrees angle of attack. This can be liked to the presence of zig-zag strips both on the suction and pressure sides of the tested model, to its non-null superficial roughness, and to the presence of a gap between the reflection plane and the root section of the wing. At angles of attack greater than 20 degrees, under-prediction of drag take place, which might be related to aero-elastic twist taking place on the wind tunnel model. This hypothesis cannot be validated as no structural data have been collected during the wind tunnel testing.

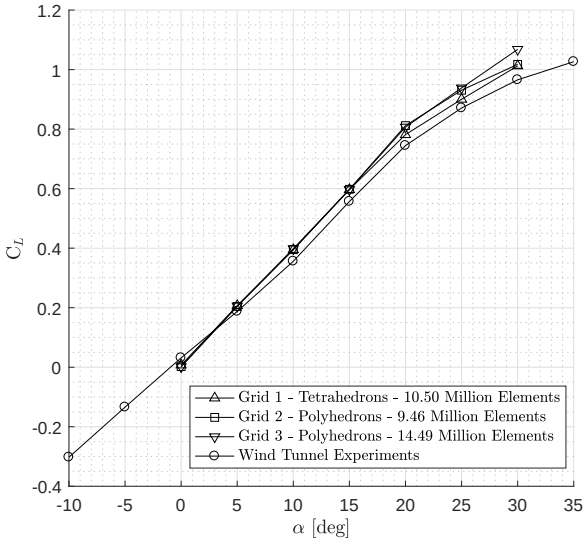

Figure 3.24: Comparison Computational and Experimental Results. C_L vs α.

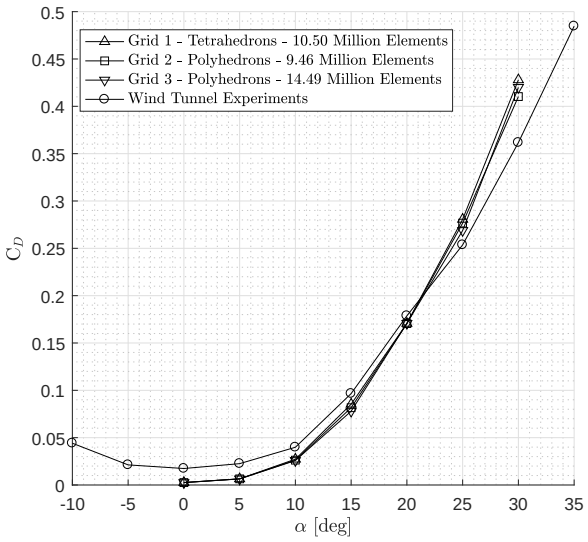

Figure 3.25: Comparison Computational and Experimental Results. C_D vs α.

The wind tunnel and CFD pitching moment characteristics are presented in Fig. 3.26 with respect to the angle of attack, and in Fig. 3.27 with respect to the lift coefficient. The pitching moment characteristics are different in terms of: zero lift pitching moment coefficients, which is underestimated by the CFD analysis of about 0.025, and pitching moment slope for angles of attack greater than 5 degrees. The pitch-up break tendency is observed at 20 degrees angle of attack on both from the experimental data, the results from Grid 2, and the results from Grid 3. By observing at the pitching moment curve against the lift coefficient, Fig. 3.27, a better agreement is observed between the Grid 2 and Grid 3 curves with the experimental data for lift coefficient larger than 0.8.

The comparison in terms of pitching moment derivative with respect to the angle of attack between the experimental and numerical results are presented by plotting the location of the aerodynamic center in longi-

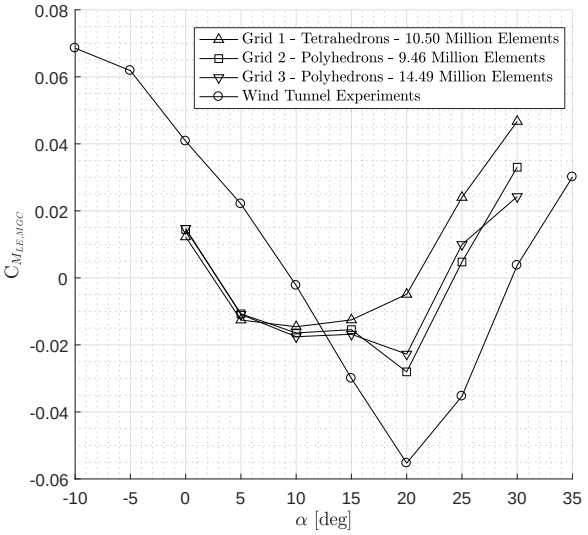

Figure 3.26: Comparison Computational and Experimental Results. C_M vs α.

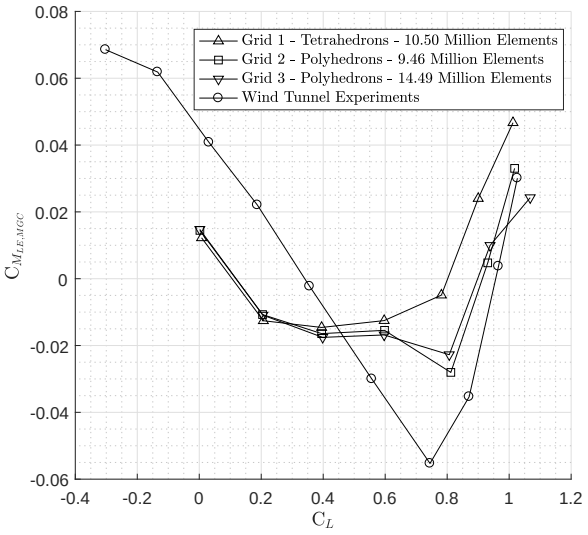

Figure 3.27: Comparison Computational and Experimental Results. C_M vs C_L.

tudinal direction from the nose of the model. The spanwise locations of the aerodynamic center are reported as well. In Fig. 3.28, the locations of the aerodynamic center are presented on the planform view of the wing. In Fig. 3.29 and Fig. 3.30, the shift of the longitudinal and spanwise location of the aerodynamic center at different angles of attack is plotted against the angle of attack.

The longitudinal locations of the aerodynamic center of the model, estimated using the CFD data, does match with the location estimated using the wind tunnel data only at null angle of attack. In general, the aerodynamic center is not properly predicted by the CFD analyses. All the simulations predict a the aerodynamic center of the configuration to be located more forward than the locations estimated using the wind tunnel data. In the range between 5 and 15 degrees, the discrepancies of the longitudinal locations of the aerodynamic center estimated using CFD and those estimated using wind tunnel data are in a range between 6 and 12 centimeters, from about 7% to 14.6% of the mean geometric chord. The best agreement on the location of the aerodynamic center is given by the results from Grid 2.

The aerodynamic center of the half-wing is better predicted in spanwise direction as presented in Fig. 3.30. Up to 25 degrees, the CFD predicts the spanwise locations of the aerodynamic center with an error lower than 5 centimeters, about 3% of the reference semi-span, with respect to the estimation based on the wind tunnel data. The best agreement with the experimental data is achieved by the results from Grid 2.

The lower slope of the wind tunnel data with respect to that from the data from CFD simulations might be related to the use of an open jet facility, which is an effect reported in literature [15]. The lower lift coefficient, and lower lift coefficient slope, of the wind tunnel data with respect to the numerical simulations can also be related to structural deformations which have not been modeled. No data has been collected about the structural deformations during the wind tunnel testing campaign. It is worth to be reported that the inboard part of the wind tunnel model is missing the two most inboard ribs to allow the installation of the model on the wind tunnel setup, therefore the torsional stiffness of the model near the root section is reduced. It has not been possible to clearly identify the causes behind the discrepancies in terms of lift and drag characteristics between the wind tunnel data and the CFD simulations. The pitching moment discrepancies can be related to the leading edge separation taking place on the rear zone of the wing, presented in Chapter 4.

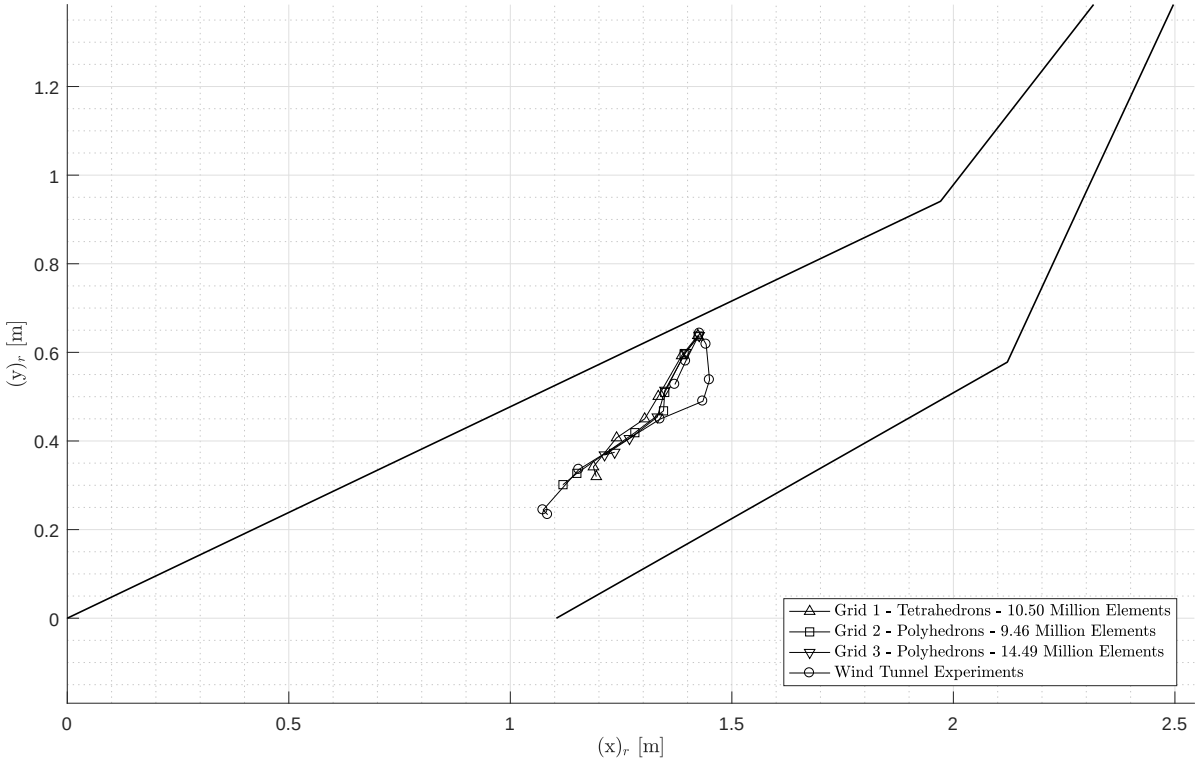

Figure 3.28: Comparison Computational and Experimental Results. Aerodynamic center locations projected on the planform view of the configuration.

In general, the discrepancies can be linked to geometrical differences due to the manufacturing of the model, the influence of the zig-zag strips on the aerodynamics of the wing, to structural deformations during the wind tunnel testing, or to eventual interference with the wind tunnel setup.

The results from the numerical investigations presented in Chapter 4 are relative to the simulations performed using the Grid 2 as these results presents the best agreement with the experimental results in terms of lift coefficient and position of the aerodynamic center both in longitudinal and spanwise directions within the investigated range of angles of attack.

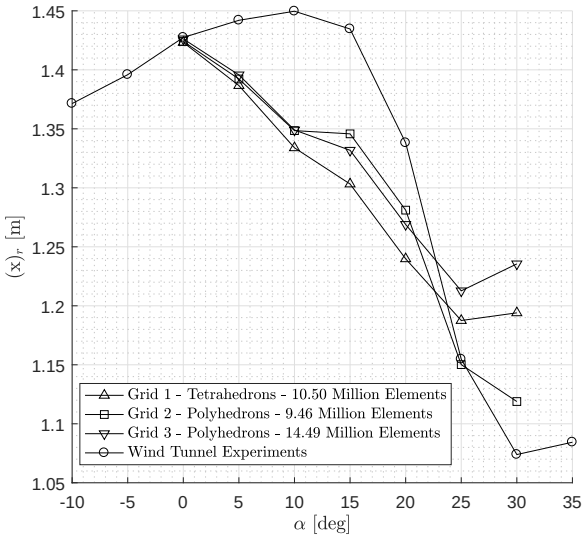

Figure 3.29: Comparison Computational and Experimental Results.
$(x_{ac})_r$ vs α.

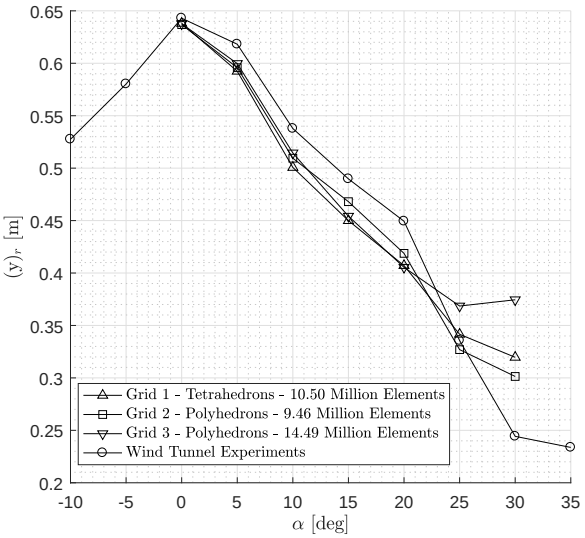

Figure 3.30: Comparison Computational and Experimental Results.
$(y_{ac})_r$ vs α.

4

Results

4.1. Wind Tunnel

The data collected during the performed wind tunnel campaign are presented in the current section. The balance measurements are unbiased assuming a linear increment of the bias over the testing time. No open jet wind tunnel corrections have been applied on the collected data.

In the current section the following activities are presented:

- Explaination of the motivation not to apply open jet wind tunnel corrections.
- Presentation of the aerodynamic characteristics of the tested model.
- Individuation of the location of the aerodynamic center within the studied range of angles of attack both in longitudinal and spanwise directions.

4.1.1. Wind Tunnel Data Corrections

Although many corrections for the wind tunnel data collected in open jet facilities are presented by Barlow et al. [15], no open-jet wind tunnel corrections have been applied to the collected data. The main reason to this choice is that the streamlines corrections identified in literature have been developed under the assumption of two dimensional flow, which is not representative of the flow over Flying V model.

Further, as the tested model is about 2.5 m long and about 1.5 m high, the application of a global streamline curvature correction factor or of a dynamic pressure correction factor over the entire wing might not be correct as well since the correction factors might change in longitudinal and spanwise directions. Based on these considerations, the airspeed is considered to be constant over the entire wing and the flow of the open-jet wind tunnel full developed over the entire setup.

No existent wind tunnel correction has been identified in literature for a testing similar to the one performed on the Flying V half model. Rather than applying a partially wrong correction factor, raw data are preferred to be used. The major effect reported by Barlow et al. [15] due to wind tunnel testing in open jet wind tunnel is a

mismatch between the geometric and the aerodynamic angle of attack. The effect would result in underestimated derivatives of forces and moments with respect to the angle of attack, therefore leading to conservative estimations.

4.1.2. Aerodynamic Characteristics of the Flying V Wind Tunnel Model

The aerodynamic characteristics of the Flying V are presented in Fig. 4.1, 4.2, and 4.3. The reference point for the estimation of the pitching moment coefficients is the projection of the leading edge point of the mean geometric chord onto the symmetry plane of the model. The leading edge of the mean geometric chord is presented in Fig. 2.4 and its location is reported in Table 2.2.

Within the investigated range of angles of attack, the Flying V configuration present the typical lift characteristics of low aspect ratio wings, low C_{L_α} and an unstable pitch break, typical of tailless aircraft. By analyzing the pitching moment characteristics of the configuration, pitch break takes place at 20 degrees in a repeatable manner.

No abrupt loss of lift typical of high aspect ratio wings can be observed in the C_L-α plot, the Flying V model does aerodynamically perform similarly to a delta wing by generating at high angles of attack a lift contribution referred in literature as "vortex lift". At about 20 degrees angle of attack, a reduction in lift coefficient slope can be observed. The impact of control surface deflections on lift coefficient is relatively small over the entire range of tested angles of attack.

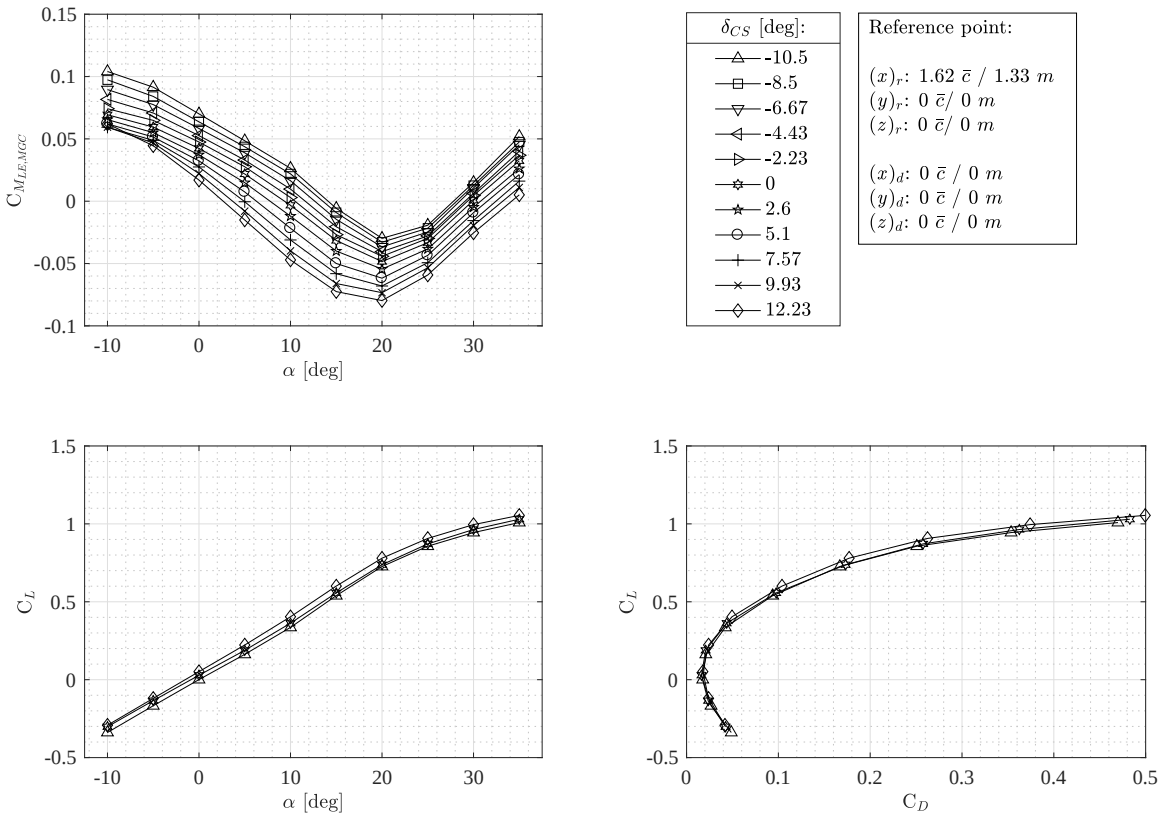

Figure 4.1: Aerodynamic effects of CS1. $V_\infty \approx 20$ m/s. $Re_{\bar{c}} \approx 1 \cdot 10^6$. $\rho \approx 1.22$ kg/m^3.

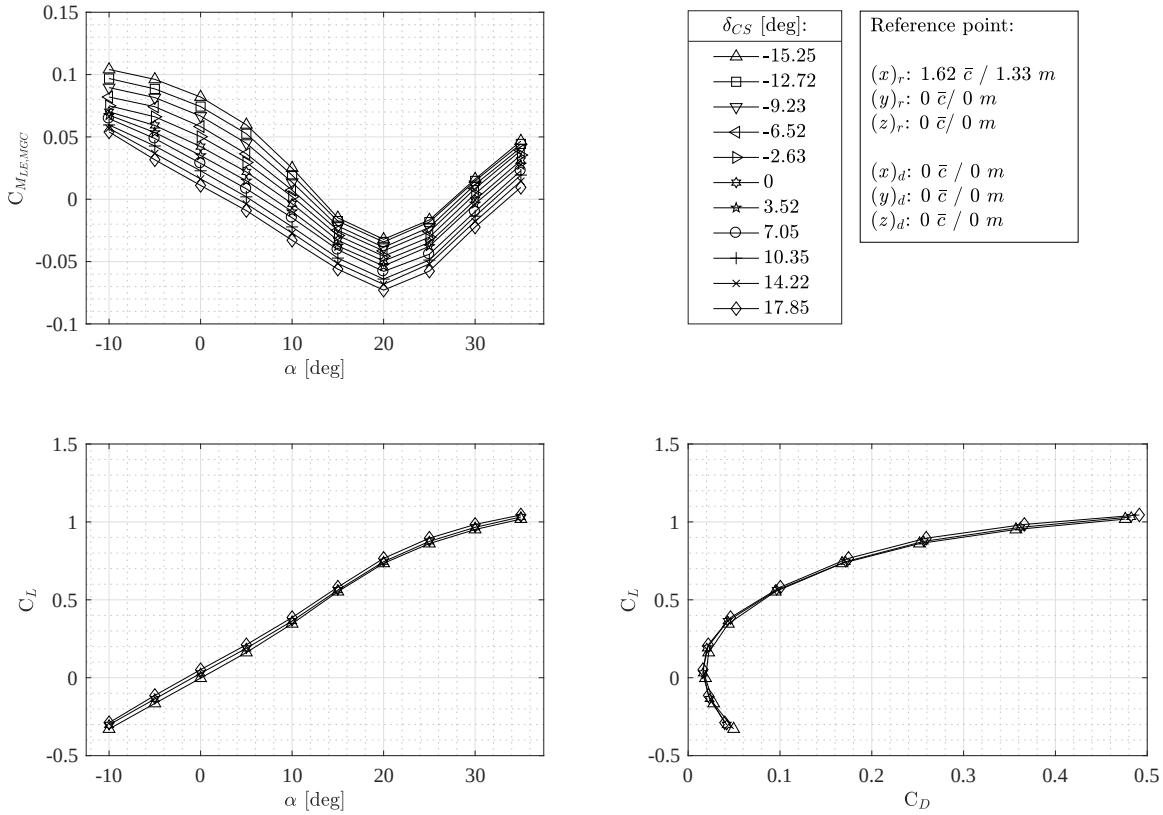

Figure 4.2: Aerodynamic effects of CS2. $V_\infty \approx 20$ m/s. $Re_{\bar{c}} \approx 1 \cdot 10^6$. $\rho \approx 1.22$ kg/m^3.

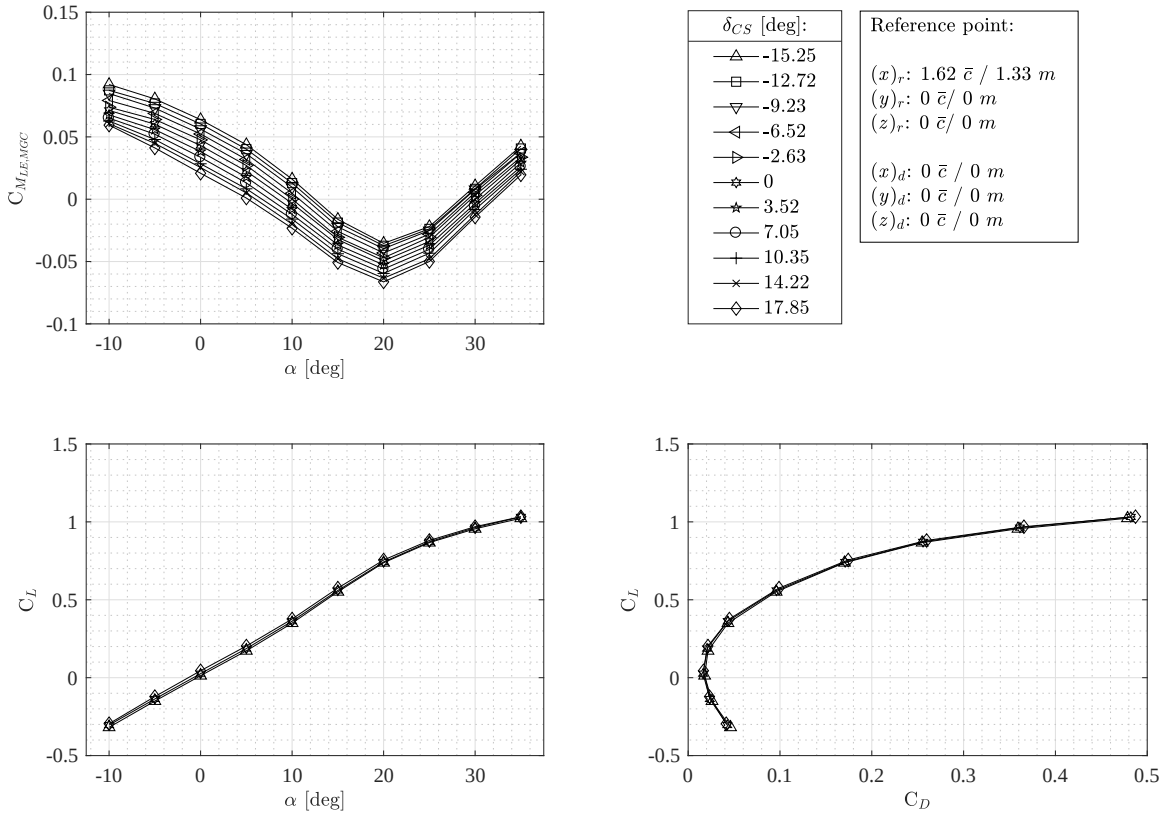

Figure 4.3: Aerodynamic effects of CS3. $V_\infty \approx 20$ m/s. $Re_{\bar{c}} \approx 1 \cdot 10^6$. $\rho \approx 1.22$ kg/m^3.

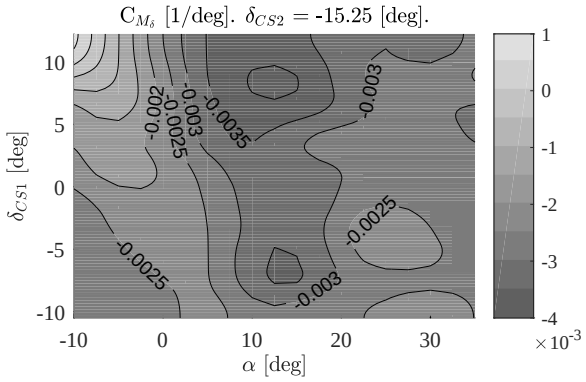

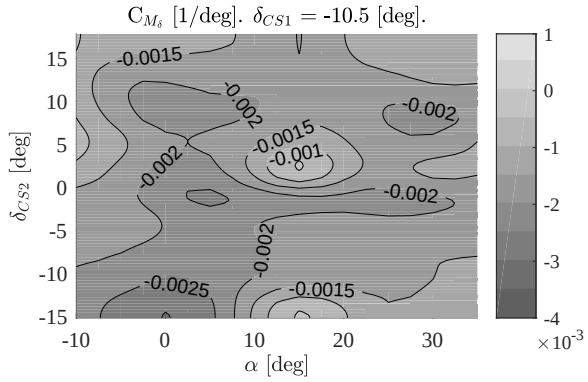

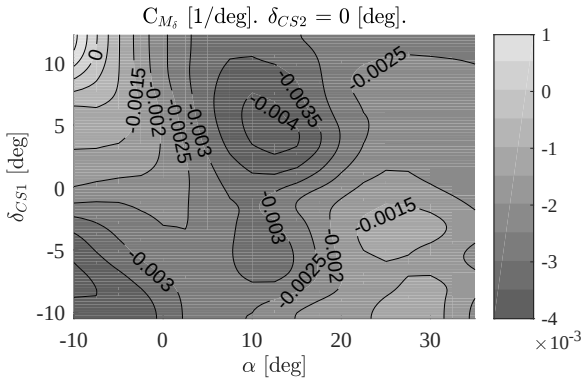

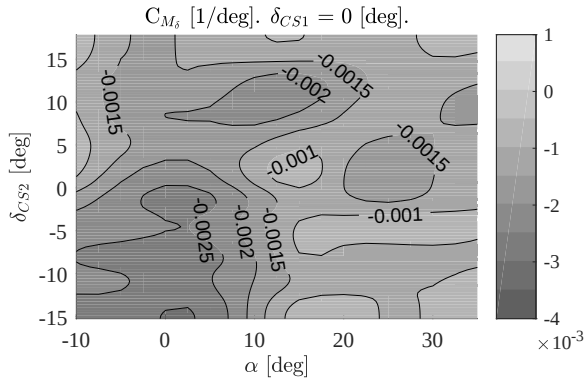

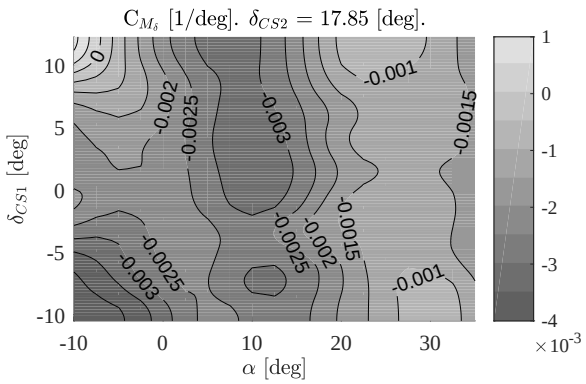

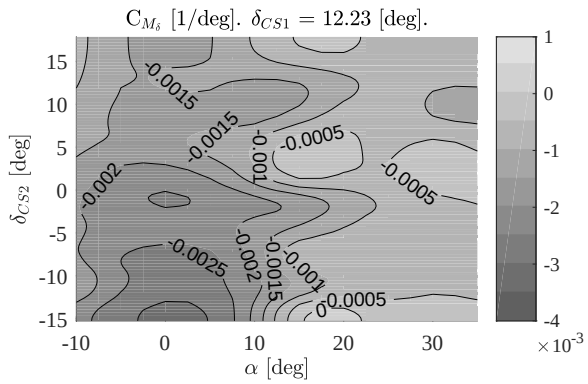

Figure 4.4: Pitching moment control power contours of CS1. $V_\infty \approx 20$ m/s. $Re_{\bar{c}} \approx 1 \cdot 10^6$. $\rho \approx 1.22$ kg/m^3.

Figure 4.5: Pitching moment control power contours of CS2. $V_\infty \approx 20$ m/s. $Re_{\bar{c}} \approx 1 \cdot 10^6$. $\rho \approx 1.22$ kg/m^3.

As expected based on the geometric characteristics and locations of the control surfaces presented in Table 2.4, the two inner control surfaces present a greater pitching moment control authority with respect to the third one, which can be observed in the pitching moment plots in Fig. 4.1, 4.2, and 4.3. Contours of the pitching moment control powers of CS1 and CS2 are presented in Fig. 4.4 and 4.5 within the investigated range of angles of attack. The pitching moment control power are presented for full-up, null and full down deflection of the consecutive control surface. At positive angles of attack, reductions of control power of the inboard control surface, CS1, are observed as the deflection of the second control surface is more positively deflected. The same trend is observed for the second control surface. At 20 degrees, when the pitch-up break take place, the pitching control power of the inboard control surface tends to decrease at larger angles of attack for fixed control surface deflections. The maximum values in pitching moment control power of CS1 are in the range of angles of attack between 10 and 20 degrees, during the wind tunnel campaign a vortex

has been noticed to be released from the kink on the leading edge of the model. No pictures are available of this phenomena although the presence of a vortex released from the leading edge kink region has been reproduced by the CFD simulations. A positive control power region is identified for full-down deflected values of the inboard control surface at about -10 degrees angle of attack. The control power of CS2 appears to be more influenced by the deflection of CS1. This effect can be related to the outboard crossflow tendencies that take place over back-swept wings or to eventual influences of the deflection of CS1 on the vortex released from the leading edge kink zone. No data is available to identify the causes. All the control surfaces still present negative control power in the range of angles of attack between 0 and 35 degrees. Although some loss of effectiveness of the control surfaces take place at larger deflections, by increasing the gearing ratio of the leverages of the control surfaces more control authority could be gained. No deep-stall characteristics are observable.

In case the control surfaces are used singularly, the angle of attack range in which pitch-trim conditions can be achieved about the selected reference point is quite small:

- $\alpha_{\text{trim}}\big|_{\text{CS1}} \in [2.2; 14]$ degrees;
- $\alpha_{\text{trim}}\big|_{\text{CS2}} \in [2.2; 12]$ degrees;
- $\alpha_{\text{trim}}\big|_{\text{CS3}} \in [5; 12]$ degrees;

To widen the range of angles of attack in which trim conditions can be achieved, the two possibilities are either to use multiple control surfaces for pitch control, to aft-shift the location of the center of gravity thus reducing C_{M_α}. While the first solution does not present any major drawback, the second solution does. By aft-shifting the center of gravity, the static stability margin is reduced and the natural forward shift of the aerodynamic center at high angles of attack might limit the maximum trimmed lift coefficient in case ultimate static stability margin requirements are set on the configuration.

4.1.3. Individuation of the Aerodynamic Center

The longitudinal locations of the aerodynamic center of the aircraft are estimated from the collected data. To give an idea of the location of the aerodynamic center traveling within the investigated range of angles of attack, the identified aerodynamic centers are plotted over the planform view of the model in Fig. 4.6 relatively to the cases of full-up, null, and full-down deflections of the inboard and central control surfaces. The same data are presented as longitudinal and spanwise locations of the aerodynamic center as function of the angle of attack in Fig. 4.7.

The data presented in Fig. 4.7 highlight the non-linear aerodynamic phenomena taking place on the wing which have been found to be dependent both on the angle of attack as well as the deflection of the control surfaces. Three intervals of angles of attack, for which trends can be identified in relations to fixed deflections of the control surfaces, are found. The bounds of the three intervals are presented in Fig. 4.7 as vertical dashed gray lines.

- I_1: $\alpha \in [-10; \alpha_{I_1}]$ degrees;
- I_2: $\alpha \in [\alpha_{I_1}; \alpha_{I_2}]$ degrees;
- I_3: $\alpha \in [\alpha_{I_2}; 35]$ degrees;

The values α_{I_1} and α_{I_2} are dependent on the deflection of the second control surface, which is already explanatory of complex aerodynamic phenomena. The values of α_{I_1} and α_{I_2} for three deflections of the second

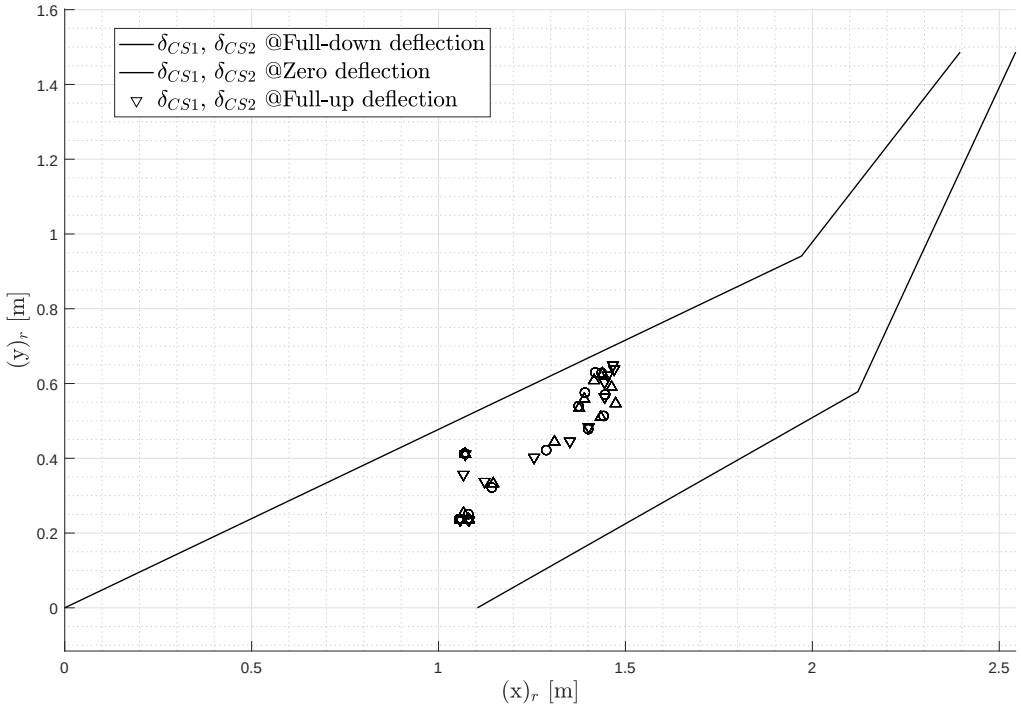

Figure 4.6: Aerodynamic center locations on the wing planform top view within the investigated range of angles of attack at different deflections.

control surface are presented in Tab. 4.1. The variations of α_{I_2} for different deflections of the second control surface are smaller compared to the variation of α_{I_1}, which can be interpreted as a greater influence of the control surfaces on the aerodynamic flow-field over the wing at lower angles of attack rather than at higher angles of attack. The variation of α_{I_1} might highlight the influence of the second control surface on the development of the vortices observed during the wind tunnel campaign on the suction side of the wing. In general, in Fig. 4.7 the effects of both the inboard, referred as CS1, and the central, referred as CS2, control surfaces on the aerodynamic center are observable and non negligible.

Table 4.1: α_{I_1} and α_{I_2} values for three deflections of the second control surface.

δ_{CS2}	-15.2	0	17.8
α_{I_1}	12.5	10.5	9.5
α_{I_2}	27.3	27.4	28

The effects of the angle of attack and of the deflections of the control surfaces on the longitudinal location of the aerodynamic center are described for the three identified intervals of angles of attack.

- $\alpha \in I_1$: the aerodynamic center shifts after when the angle of attack increases. Negative deflections of the first control surface induce aft-shift. Positive deflections of the first control surface induce forward shift. When the first control surface is deflected negatively and the angle of attack approaches α_{I_1}, the aerodynamic center start shifting forward.
- $\alpha \in I_2$: the aerodynamic center shifts forward when the angle of attack increases. Negative deflections of the first control surface induce the aerodynamic center to shift forward. Positive deflections of the first control surface induce the aerodynamic center to shift rearward.
- $\alpha \in I_3$: the aerodynamic center tends to stabilize for null and negative deflections of the first control

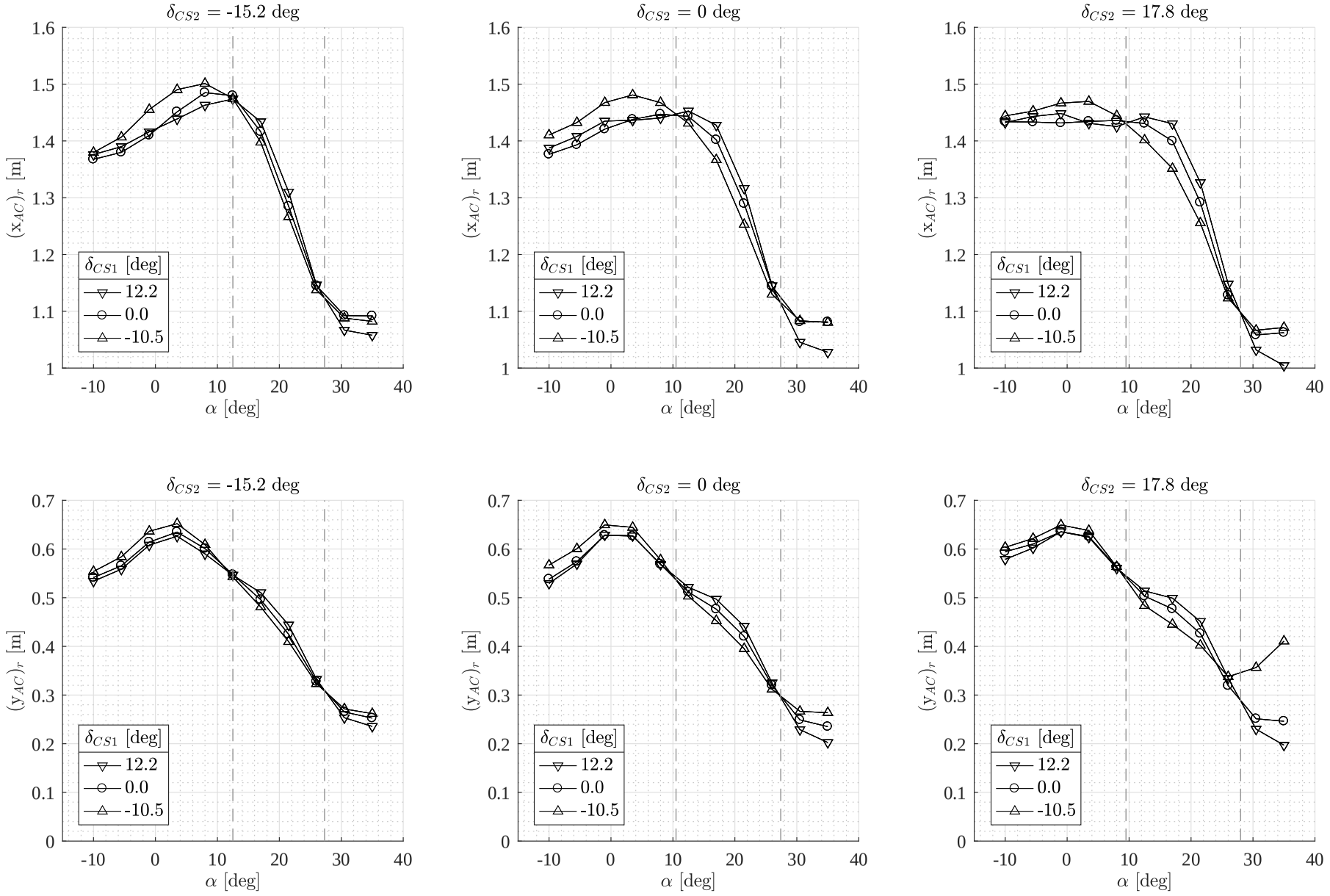

Figure 4.7: Longitudinal and spanwise locations of the aerodynamic center over the tested half-wing as functions of the angle of attack for different control surface deflections.

surface. Positive deflections of the first control surface induce the aerodynamic center to shift forward, this phenomena is more and more empathized as the second control surface is more positively deflected.

The effects of the angle of attack and of the deflections of the control surfaces on the spanwise location of the aerodynamic center are described for the three identified intervals of angles of attack.

- $\alpha \in I_1$: the aerodynamic center shifts inboard when the angle of attack increases in magnitude. Negative deflections of the first control surface induce outboard shifts. Positive deflections of the first control surface induce inboard shifts.
- $\alpha \in I_2$: the aerodynamic center shifts inboard when the angle of attack increases. Negative deflections of the first control surface induce inboard shifts. Positive deflections of the first control surface induce outboard shifts.
- $\alpha \in I_3$: the aerodynamic center tends to stabilize for null and negative deflections of the first control surface for null and negative deflections of the second control surface. The aerodynamic center shifts inboard when CS1 is positively deflected and the inboard-shifting tendency increases if the second control surface is positively deflected as well. When the second control surface is positively deflected at 17.8 degrees, if the first control surface is deflected negatively at -10.5 degrees, the aerodynamic center seems to shift outboard of about 170 mm with respect to the location relative to null deflection of the first control surface.

Although no data visualization or balance measurements of CS1, CS2, and CS3 have been collected, a physical explanation for the forward shifting of the aerodynamic center at 35 degrees with both CS1 and CS2 fully positively deflected is presented. The positive deflections both of CS1 and CS2 might induce the vortex released at the kink to flow in a more streamwise direction, thus causing a loss of effectiveness on the most outboard sections of the wing. The presented speculation is supported by the fact that the aerodynamic center longitudinal location decrease, shift forward, as the second control surface passes from negative to positive deflections. The presented explaination is also in agreement with the spanwise shifting tendency of the aerodynamic center at 35 degrees. A possible check, beside the use of flow visualization techniques, might be the collection of balance data of CS3 data at 35 degrees for full down deflections of CS1 and CS2 to check whether the most outboard control surface is still effective or not.

4.2. Numerical Investigation

The results of the RANS simulations are analyzed to:

- Allow the visualization of the vortical structures developing over the configuration at relatively high angles of attack.
- Assess the influence of the vortices over the pressure coefficient distributions over the wing.
- Present the effects of the vortices on the spanwise distributions of the aerodynamic forces.

4.2.1. Vortex Visualization

Vortex cores are identified by making use of the λ_2 criterion [45, 46]. Top and isometric views of the iso-λ_2-surfaces over wing are presented in Figs. from 4.8 to 4.17.

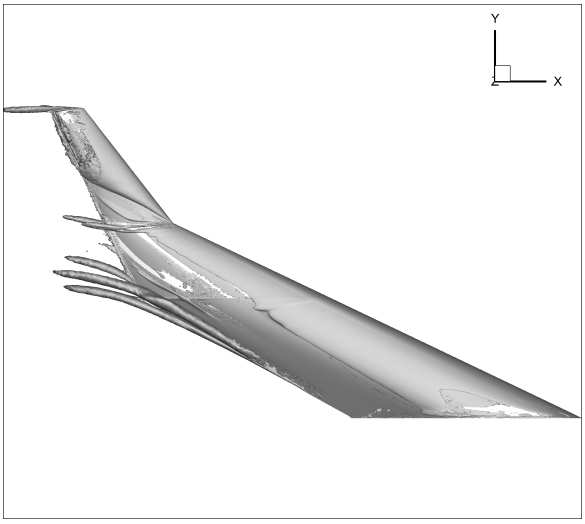

Figure 4.8: Vortical structures visualization. Top view.
α = 10 degrees.

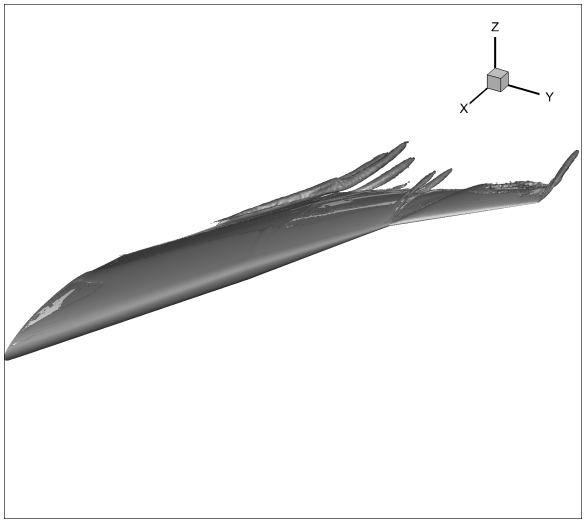

Figure 4.9: Vortical structures visualization. Isometric view.
α = 10 degrees.

In Fig. 4.8 and 4.9, the identified vortical structures around the wing at 10 degrees angle of attack are presented. Many vortexes start developing at this angle of attack. Two vortices are identified flowing over the inboard trunk of the wing one developing over the suction side and one rolling up along the trailing edge from the pressure to the suction side. In proximity of the leading edge kink, a vortex is released and flows towards over the central trunk of the wing. No vortices other than the tip vortex can be identified on the outer trunk of the wing. The iso-surface highlights the tendency of the flow in flowing outboard.

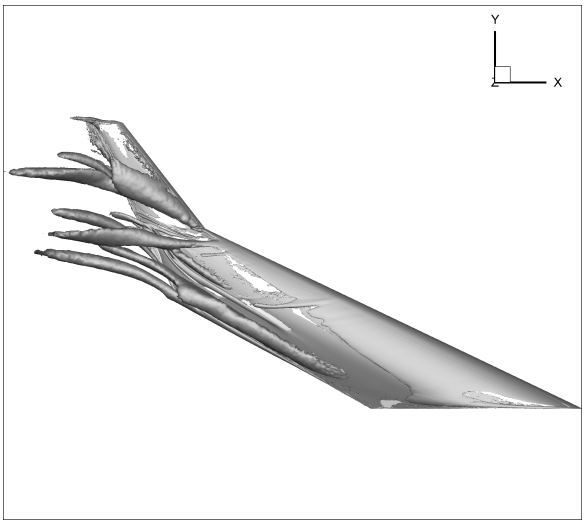

Figure 4.10: Vortical structures visualization. Top view.
α = 15 degrees.

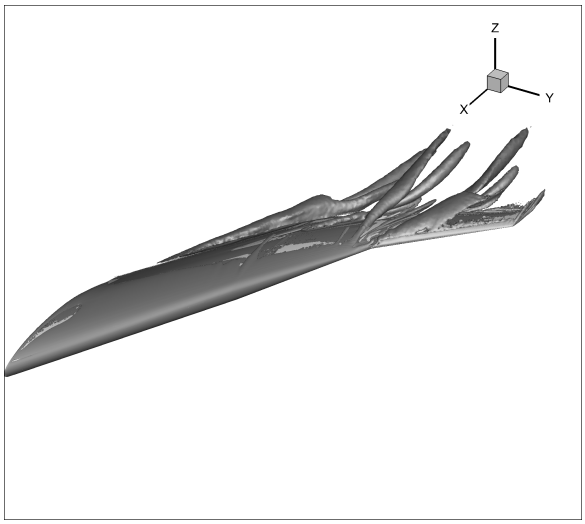

Figure 4.11: Vortical structures visualization. Isometric view.
α = 15 degrees.

In Fig. 4.10 and 4.11, the identified vortical structures around the wing at 15 degrees angle of attack are presented. The two vortical structures identified at 10 degrees starts developing and rolling towards the suction side more inboard. In proximity of the leading edge kink, two vortices develop: one on the central trunk and one on the outboard trunk. Leading edge separation is observable on the outer trunk.

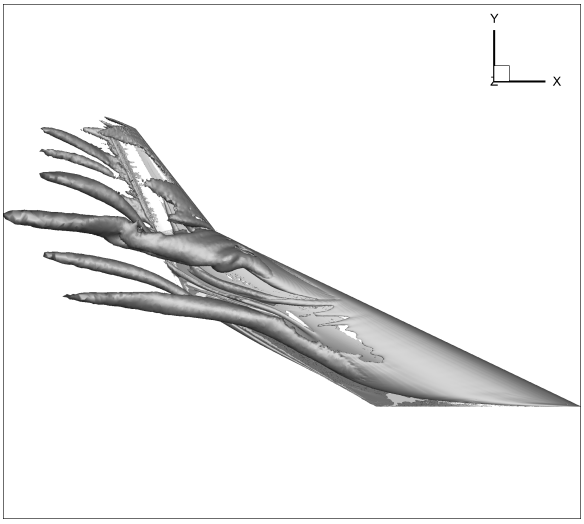

Figure 4.12: Vortical structures visualization. Top view.
α = 20 degrees.

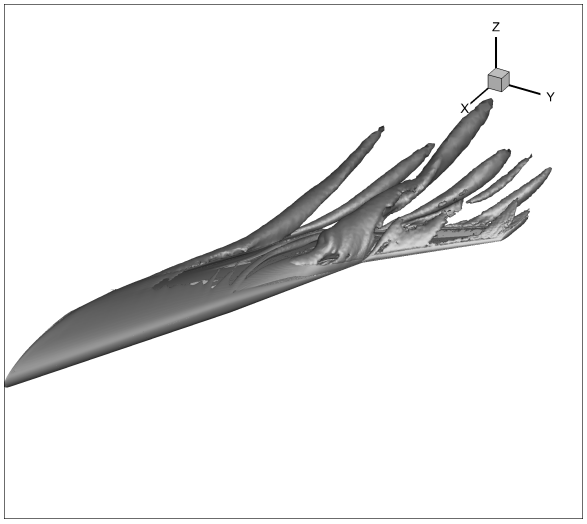

Figure 4.13: Vortical structures visualization. Isometric view.
α = 20 degrees.

In Fig. 4.12 and 4.13, the identified vortical structures around the wing at 20 degrees angle of attack are presented. Over the inboard trunk, the vortical structure developing on the suction side separates from the surface of the wing near the end of the end of the inboard trunk and flows away from the wing. The vortex rolling up from the pressure towards the suction side is still present. A large vortical structure is identified near the leading edge kink. A vortex starts developing at the inboard section of the outer trunk of the wing. Leading edge separation is observed to take place at the leading edge of the outer trunk of the wing.

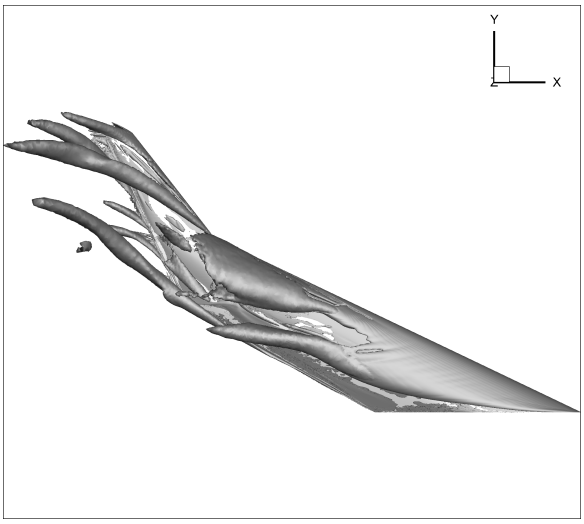

Figure 4.14: Vortical structures visualization. Top view.
α = 25 degrees.

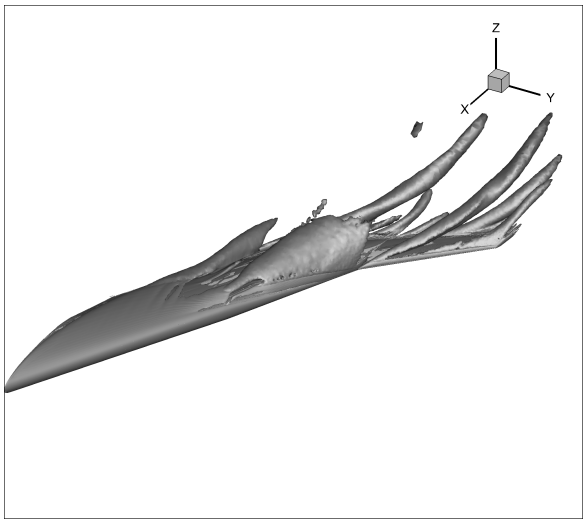

Figure 4.15: Vortical structures visualization. Isometric view.
α = 25 degrees.

In Fig. 4.14 and 4.15, the identified vortical structures around the wing at 25 degrees angle of attack are presented. The separation of the vortex that develops on the inboard trunk of the wing takes place more inboard than at 20 degrees. The vortical structure present near the leading edge of the wing develops more inboard. A vortex starts in proximity of the leading edge kink on the outer trunk of the wing and separates.

Leading edge separation is observed on the leading edge of the outer trunk of the wing.

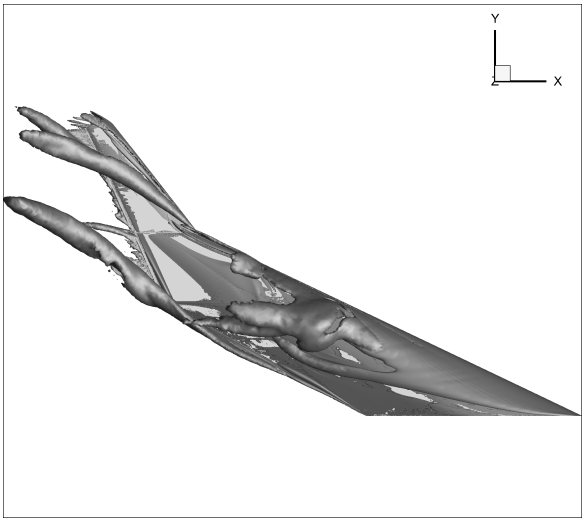

Figure 4.16: Vortical structures visualization. Top view.
α = 30 degrees.

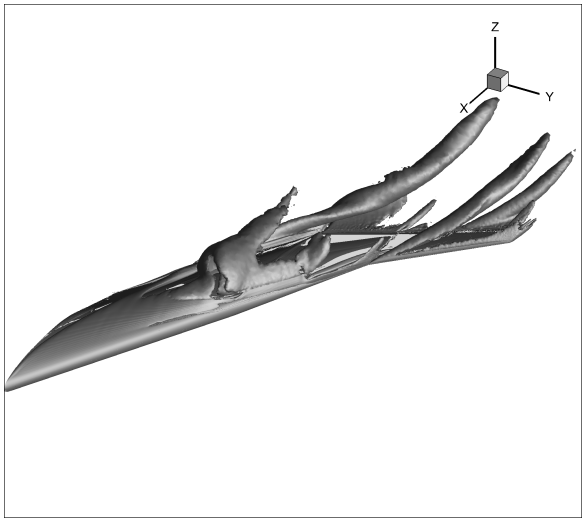

Figure 4.17: Vortical structures visualization. Isometric view.
α = 30 degrees.

In Fig. 4.16 and 4.17, the identified vortical structures around the wing at 30 degrees angle of attack are presented. Three main vortical structures are present: one near the leading edge of the wing near the end of the first trunk; one vortex rolling up from the pressure towards the suction side of the wing of the inboard trunk; a vortex developing from the leading edge kink which separates from the wing surface and flows away.

To recap, four vortical structures have been identified in the investigated range of angles of attack:

- A vortical structure flowing from the pressure towards the suction side which at higher angles of attack starts rolling up more inboard.
- A vortical structure, which is present from 10 to 25 degrees angle of attack, flowing over the suction side of the wing in proximity of the trailing edge.
- A vortical structure which starts developing at 15 degrees in proximity of the leading edge kink. At higher angles of attack this vortical structure starts developing more inboard.
- A vortical structure which develops in proximity of the leading edge over the inboard and central trunks of the wing. At higher angles of attack this vortical structure starts developing more inboard.

4.2.2. Effects of Vortical Structures on Pressure Coefficient Distributions Over The Wing

To assess the effects of the vortical structures on the forces acting on the wing, the local pressure coefficient distributions are extracted from the CFD data and presented as:

- Chordwise pressure coefficient distributions at different sections of the wing at fixed angle of attack to visualize at which spanwise location the effects of the vortices fade. Presented from Fig. 4.18 to Fig. 4.23.
- Chordwise pressure coefficient distributions at fixed spanwise locations in two ranges of angles of attack. Presented in Fig. 4.24 and Fig. 4.25.

From Fig. 4.18 to Fig. 4.23, the local pressure distributions at different spanwise location are presented in isometric view to allow a qualitative comparison of the effects of the vortical structure between consecutive sections of the wing at different angles of attack. In Fig. 4.24 and Fig. 4.25, the pressure coefficients are plotted at fixed spanwise positions to allow a quantitative comparison of the performance of the local airfoil at different angles of attack and in presence and absence of eventual vortices. The effects of the previously identified four main vortical structures on the pressure coefficient distributions are hereafter analyzed. In general, the effects of the presence of a vortex flowing over the wing are an increment of supervelocities, thus a reduction of local pressure coefficient. Finally, the aerodynamic characteristics of the sections of the outer trunk of the wing are analyzed.

Effects of the vortex rolling up from the pressure towards the suction side. Observable from Fig. 4.19 to Fig. 4.23, the effects of this vortex at different angles of attack result in a peak near the trailing edge zone of the local section. In the referred figures the effects of this vortex can be clearly observed on the third, fourth, and fifth sections of the wing. These effects are also visible in Fig. 4.24 and Fig. 4.25, by looking at the pressure coefficient distributions on the sections at η 0.35 and 0.45.

Effects of the vortical structure flowing over the suction side of the inboard trunk of the wing. Observable from Fig. 4.20 to Fig. 4.22, the effects of this vortex at different angles of attack result in a bell-shaped reduction of local pressure coefficient on the affected zones. The bell-shaped pressure distribution can be clearly observed on the third, fourth, and fifth sections of the wing. These effects are also visible in Fig. 4.25, by looking at the pressure coefficient distributions on the sections at η 0.25, 0.35, and 0.45. In particular, by analyzing the effect on the wing section located at η 0.25, the upstream shift of the vortex can be observed.

Effects of the leading edge kink vortex. Observable from Fig. 4.20 to Fig. 4.23, the effects of this vortex at different angles of attack result a local overexpansion of the flow in the outer trunk of the wing. With respect to the two vortices previously described, this vortex presents a reduced influence on the pressure distributions because of the tendency of the natural tendency of the flow to separate from the wing surface. The influence of this vortex can be observed on two sections located at η 0.65 and 0.75 in Fig. 4.25. On the section located at η 0.65, at 15 degrees angle of attack the flow experiences an overexpansion for x/c(η) within 0 and 0.3 then followed by separation. The influence on the section located at η 0.75 mainly consists of the bell-shaped expansion, which has a lowered magnitude compared to the expansion taking place on the previous section.

Effects of the vortical structure developing near the leading edge of the inboard and central trunks of the wing. Clearly observable from Fig. 4.21 to Fig. 4.23, this vortex presents the strongest influence on the local pressure coefficients of the presented sections. Its effects become clear at 20 degrees, in Fig. 4.21, on the fifth section inducing a second expansion peak on the pressure coefficient distribution. This second expansion can also be observed in Fig. 4.25 relatively to the section at η 0.45 for x/c(η) values about 0.35. At larger angles of attack this vortex starts developing more inboard and its effects move as well. In Fig. 4.25, at 25 degrees angle of attack this vortex is influencing the most the pressure coefficient distribution of the section located at η 0.35; while at 30 degrees angle of attack, the largest influence takes place on the section located station at η 0.25.

Aerodynamic characteristics of the sections of the outer trunk of the wing. All the sections located between η 0.65 and 1 suffer of leading edge stall for angles of attack equal or larger than 20 degrees when no

vortices are acting on them. As observable from Fig. 4.24 and 4.25, the sections between η 0.65 and 0.75 start experiencing leading edge stall from 15 degrees onwards, while the most outboard sections of the wing, $\eta \in [0.85; 1.00]$ start suffering of leading edge stall already from 10 degrees angle of attack onwards. The presence of leading edge stall on these outer sections of the wing at relatively low angles of attack is identified as one of the possible causes of discrepancies in pitching moment coefficient between the numerical and experimental investigations, Fig. 3.26 in Chapter 3. By making the outer sections of the wing ineffective at 10 degrees angle of attack, the leading edge stall phenomena induces the magnitude reduction in C_{M_α}.

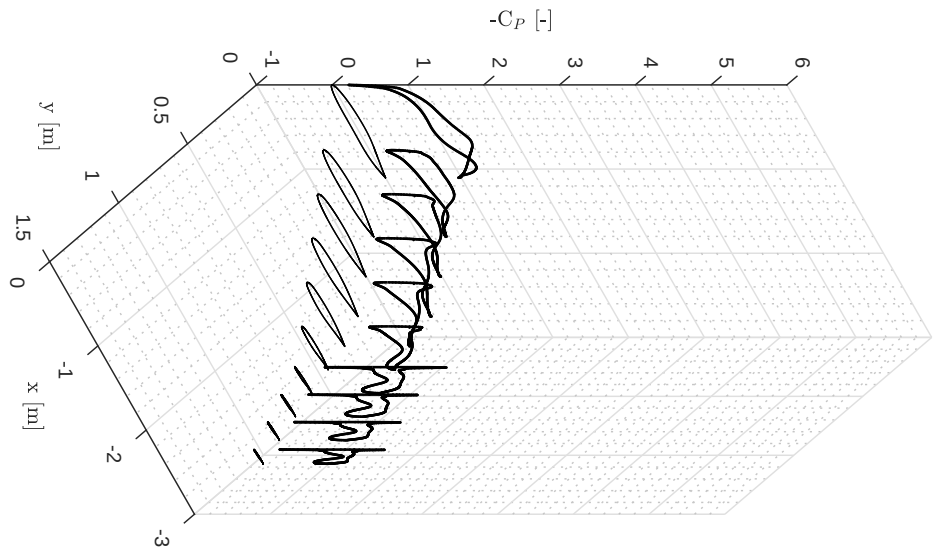

Figure 4.18: Pressure distributions on wing sections. Isometric view. $\alpha = 5$ degrees.

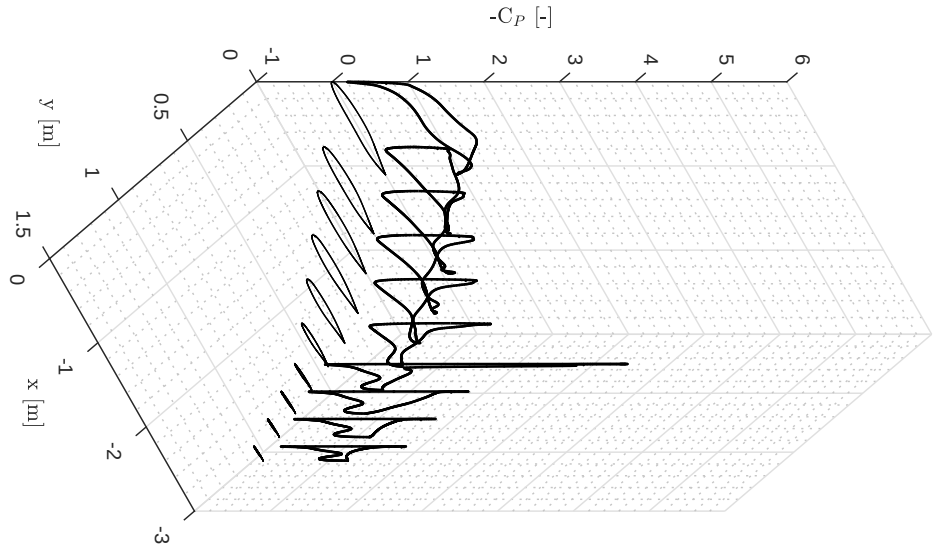

Figure 4.19: Pressure distributions on wing sections. Isometric view. $\alpha = 10$ degrees.

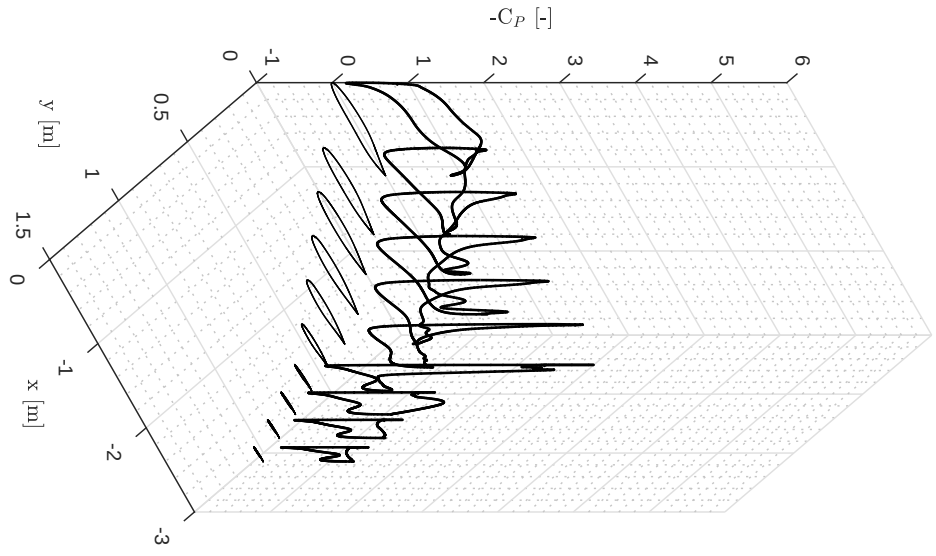

Figure 4.20: Pressure distributions on wing sections. Isometric view. $\alpha = 15$ degrees.

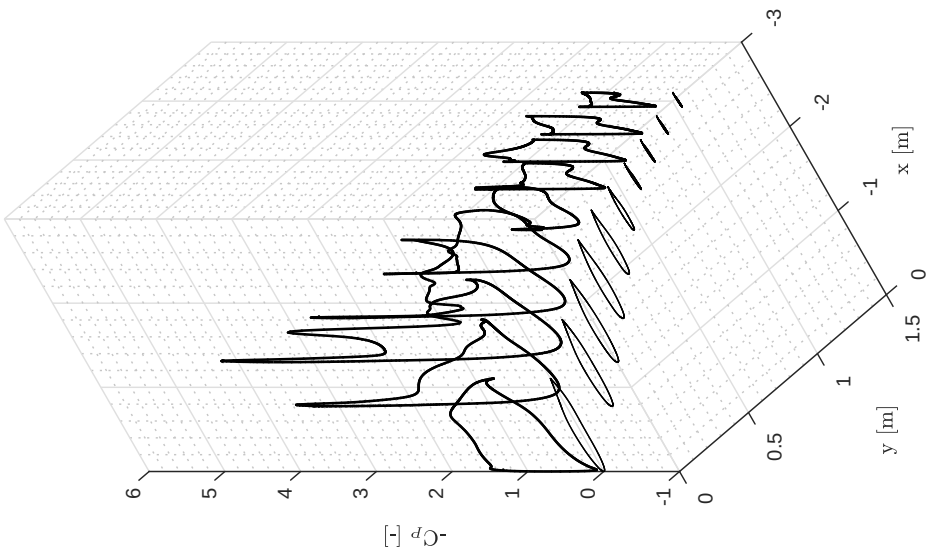

Figure 4.23: Pressure distributions on wing sections. Isometric view. $\alpha = 30$ degrees.

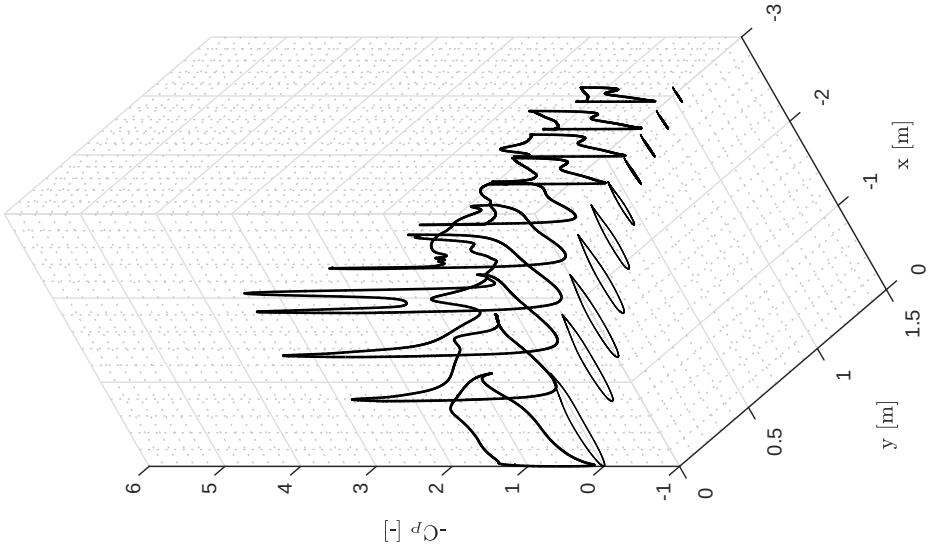

Figure 4.22: Pressure distributions on wing sections. Isometric view. $\alpha = 25$ degrees.

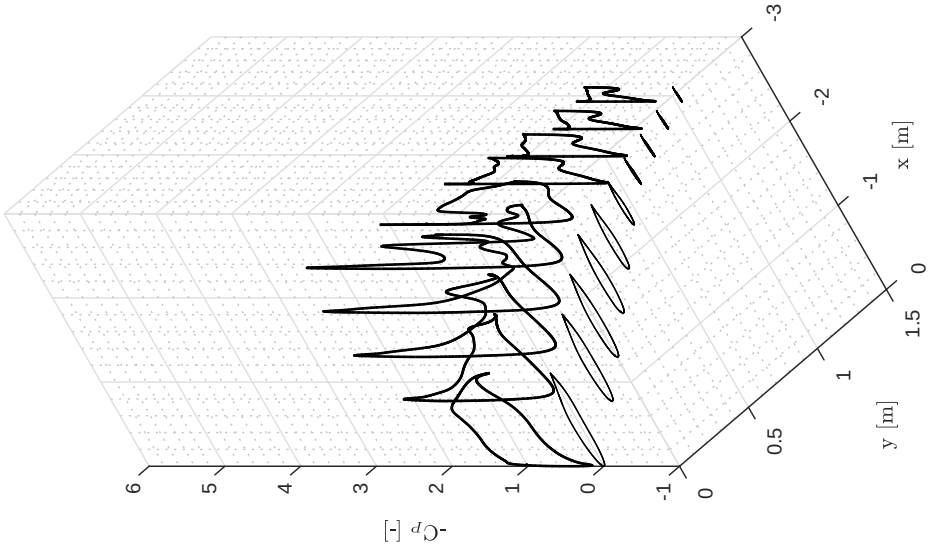

Figure 4.21: Pressure distributions on wing sections. Isometric view. $\alpha = 20$ degrees.

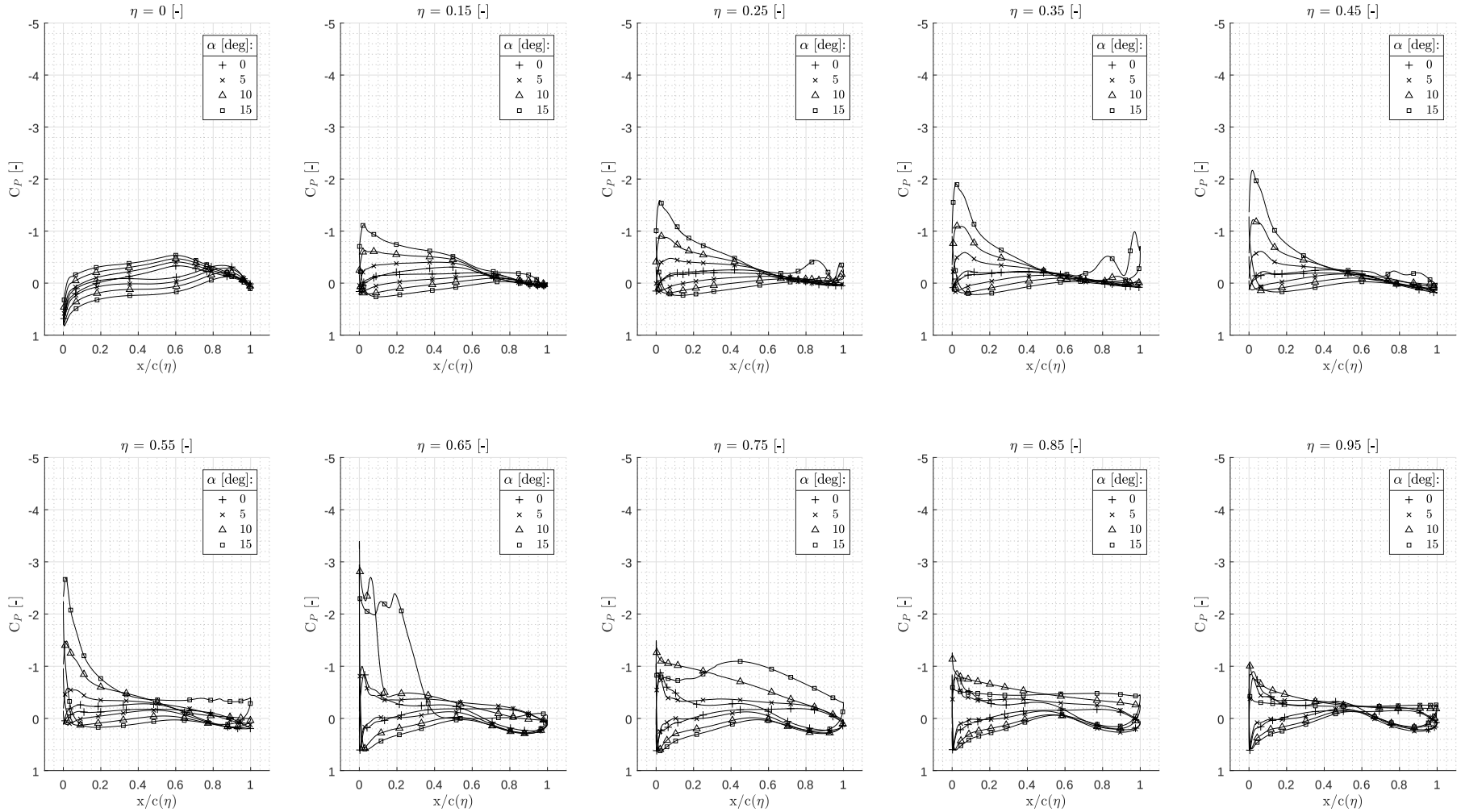

Figure 4.24: Pressure distributions at different wing spanwise locations. $\alpha \in [0; 15]$ degrees.

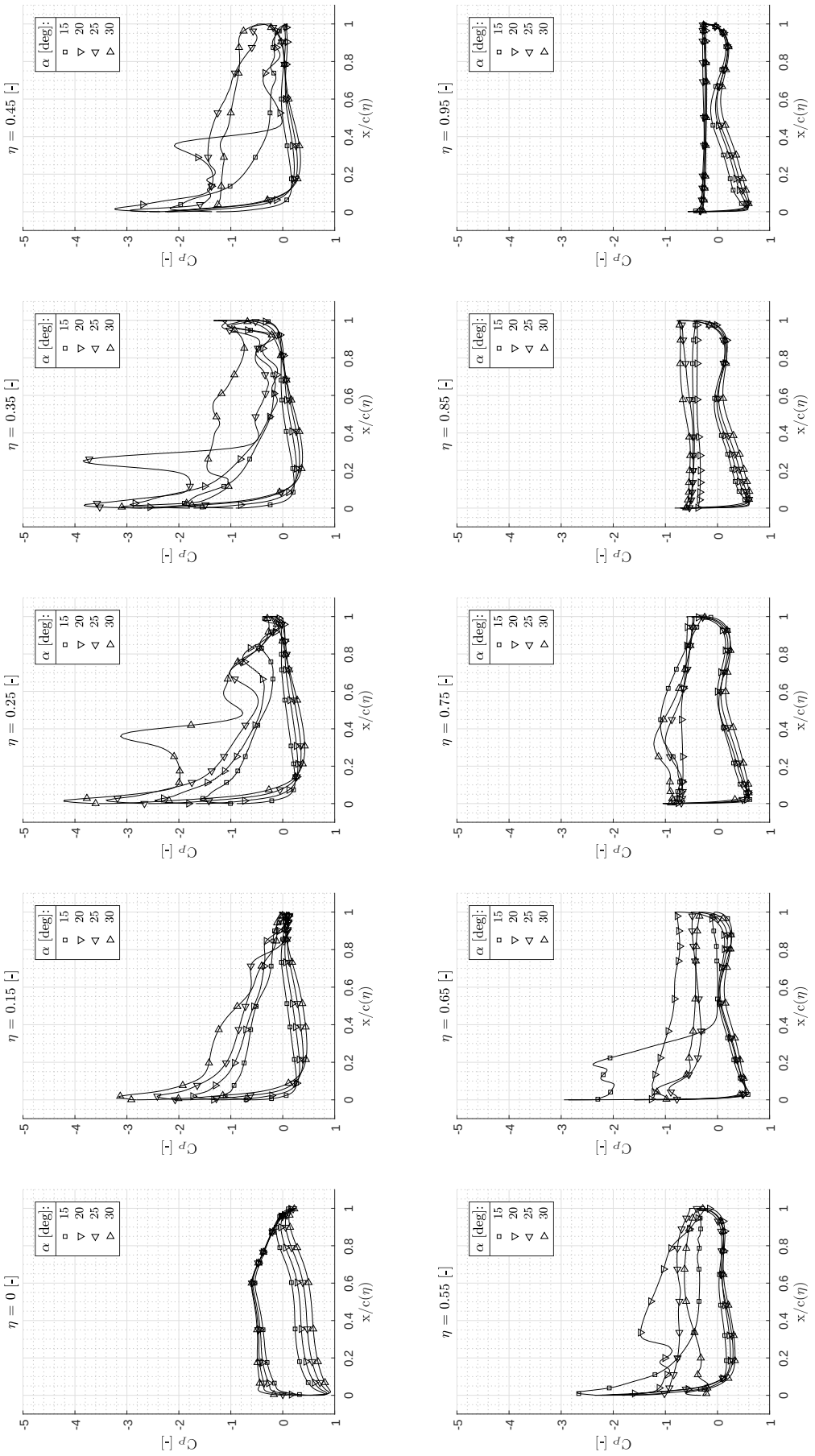

Figure 4.25: Pressure distributions at different wing spanwise locations. $\alpha \in [15; 30]$ degrees.

4.2.3. Aerodynamic Forces Spanwise Distributions

After the qualitative description of the vortical structures and the assessment of the effects of the vortices flowing over the wing on the pressure coefficient over the, the lift and drag force distributions extracted from the CFD data are hereafter discussed.

Lift force distributions are presented in terms of load distribution, defined in Eq. (4.1), and normalized load distribution, defined in Eq. (4.2). While the load distribution gives an idea of the lift produced by each section, the normalized load distribution allows to compare the contribution of each section to the overall lift coefficient. Drag force distributions are presented as defined in Eq. (4.3), which is representative of the drag produced by each section of the wing.

$$cC_l(\eta) = \frac{l(\eta)}{qc(\eta)} \tag{4.1}$$

$$\frac{cC_l(\eta)}{\bar{c}C_L} = \left(\frac{l(\eta)}{qc(\eta)}\right)\left(\frac{1}{\bar{c}C_L}\right) \tag{4.2}$$

$$cC_d(\eta) = \frac{d(\eta)}{qc(\eta)} \tag{4.3}$$

Normalized load distributions are presented in Fig. 4.27, in the angles of attack range within 0 and 15 degrees, and in Fig. 4.29, in the angles of attack range within 15 and 30 degrees. Load distributions are presented in Fig. 4.26, in the angles of attack range within 0 and 15 degrees, and in Fig. 4.28, in the angles of attack range within 15 and 30 degrees. Spanwise drag distributions are presented in Fig. 4.30, for angles of attack between 0 and 15 degrees, and in Fig. 4.31, for angles of attack between 15 and 30 degrees. In addition, the pressure coefficient contours of the suction side of the wing are presented from Fig. 4.32 to Fig. A.4 to give a visualization of the "root-tip" effect typical of backswept wings which explains the negative drag coefficients observable in Fig. 4.30.

Lift Spanwise Distributions. The following observations are reported based on the data presented in Fig. 4.26 and 4.27. Angles of attack range between 5 and 20 degrees.

1. The contribution of lift produced by the inboard trunk of the wing, $\eta \in [0, 0.38]$, increases at higher angles of attack. The vortices flowing near the trailing edge on this trunk of the wing, observable in Fig. 4.8, and 4.10, induce the peak in local load to shift outboard. At 15 degrees angle, the presence of these two vortices induce a non linear increment in normalized load of the section located within $\eta \in [0.20, 0.38]$ which can be observed in Fig. 4.27.

2. The contribution of lift produced by the central trunk of the wing, $\eta \in [0.38, 0.63]$, increases at higher angles of attack. The development of the vortical structures near the leading edge kink at 15 degrees angle of attack induces detrimental effects on the sections located within $\eta \in [0.55, 0.63]$. As it can be observed, at 15 degrees angle of attack the referred sections produce about as much lift as at 10 degrees.

3. The contribution of lift produced by the outer trunk of the wing, $\eta \in [0.63, 1.00]$, increases at higher angles of attack. The inner sections of the outer trunk, $\eta \in [0.63, 0.80]$, increase their production of lift up to 15 degrees angle of attack, while the outer sections, $\eta \in [0.80, 1.00]$, experience stall at 10 degrees not increasing anymore the production of lift at higher angles of attack. The loss of aerodynamic effectiveness of the outboard sections of the outer trunk for angles of attack larger than 10 degrees might be one

of the causes behind the previously presented discrepancies between the wind tunnel and CFD data in terms of pitching moment characteristics, and longitudinal locations of the aerodynamic centers at different angles of attack.

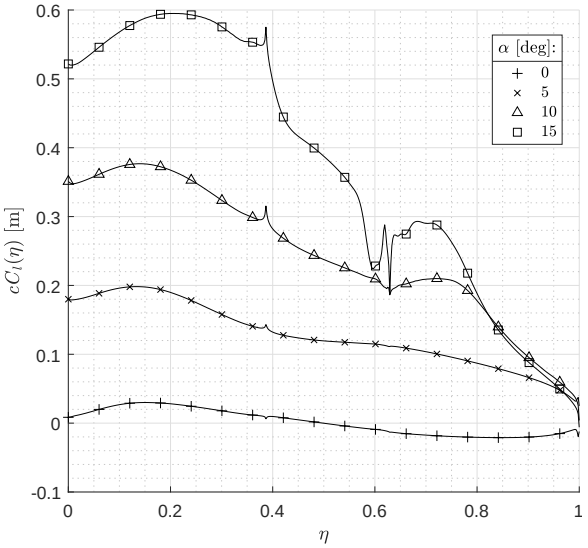

Figure 4.26: Spanwise distribution.
Aerodynamic Load.
$\alpha \in [0; 15]$ degrees.

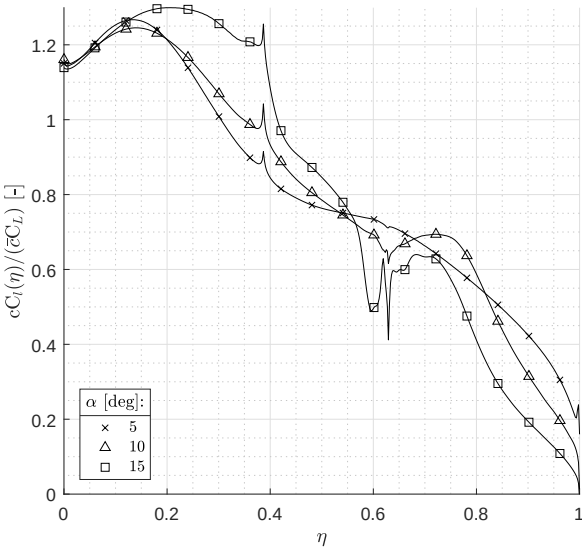

Figure 4.27: Spanwise distribution.
Normalized aerodynamic load.
$\alpha \in [0; 15]$ degrees.

The following observations are reported based on the data presented in Fig. 4.28 and 4.29. Angles of attack between 15 and 30 degrees.

1. The aerodynamic load of the inboard trunk of the wing, $\eta \in [0, 0.38]$, increases at higher angles of attack up to the location at which the leading edge vortex bursts. The presence of the vortices flowing near the trailing edge of the wing at 15, 20 and 25 degrees angle of attack is highlighted by the load peaks reported in Table 4.2. The inboard shift is due to the tendency of the vortex to separate from the wing surface at higher angles of attack. The onset of the vortex near the leading edge of the wing also contributes to the production of aerodynamic load on this section of the wing. The spanwise location of the peaks in aerodynamic load induced by the presence of the vortex flowing over the leading edge are reported in Table 4.3.

2. The contribution of the central trunk of the wing, $\eta \in [0.38, 0.63]$, to the normalized aerodynamic load decreases at higher angles of attack from 20 degrees onwards.

3. The aerodynamic load is about constant on the outer trunk of the wing, $\eta \in [0.63, 1.00]$. The sections of the outer trunk are stalled. However, between 25 and 30 degrees angle of attack the aerodynamic load increases due to the presence of the vortex released at the leading edge kink. The leading edge kink vortex acts as a vortex generator until it remains attached on the wing.

Table 4.2: Approximate spanwise locations of the load peaks due to rolling up vortex and trailing edge suction side vortex.
$\alpha \in [15; 30]$ degrees.

α	15	20	25
η	0.25	0.30	0.24

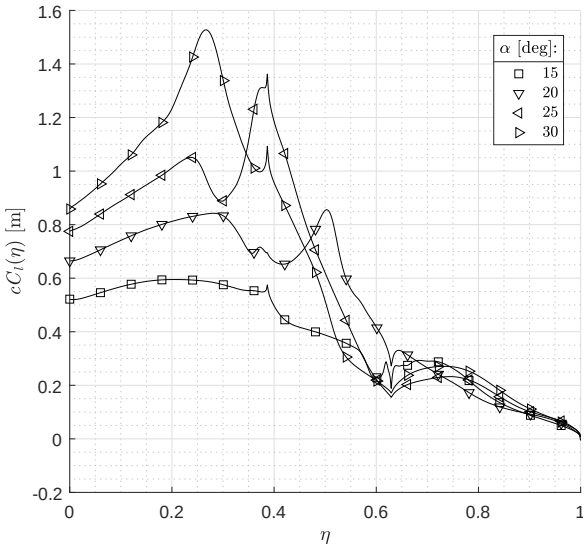

Figure 4.28: Spanwise distribution.
Lift load distribution.
$\alpha \in [20; 35]$ degrees.

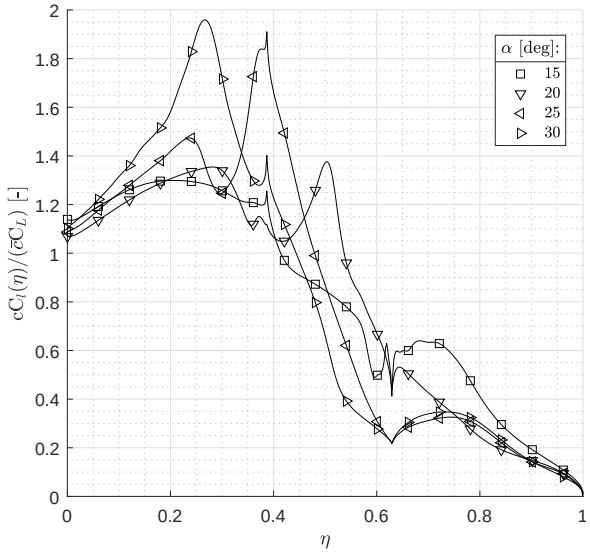

Figure 4.29: Spanwise distribution.
Normalized lift load distribution.
$\alpha \in [20; 35]$ degrees.

Table 4.3: Approximate spanwise locations of the load peaks due to the vortex developing in proximity of the leading edge of the wing. $\alpha \in [20; 30]$ degrees.

α	20	25	30
η	0.50	0.40	0.27

Drag Spanwise Distributions The following observations are reported based on the results presented in Fig. 4.30 and 4.31.

1. The larger drag produced at the root is a direct effect of the phenomena referred as "root effect" [47]. Observable from Fig. 4.32 to Fig. 4.34.

2. Up to 15 degrees regions of negative drag are present over the wing. The negative drag is a direct effect of the isobar patterns on very swept-back wings. This phenomenon is usually due as "tip effect" [47]. On the Flying V this phenomenon take place on the sections in proximity of the trailing edge kink. The sections of the wing in which this aerodynamic phenomenon takes place are visible in Fig. 4.30. The pressure coefficient distributions, which is the main cause for this phenomena, over the suction side of the wing are presented in Fig. 4.32, 4.33, and 4.34.

3. Large amount of drag is produced where vortical structures are present, which can be linked to the higher velocities induced by vortical structures.

4. The kink present at η 0.38 triggers drag production.

5. The drag produced by the outer trunk of the wing increases as higher angles of attack.

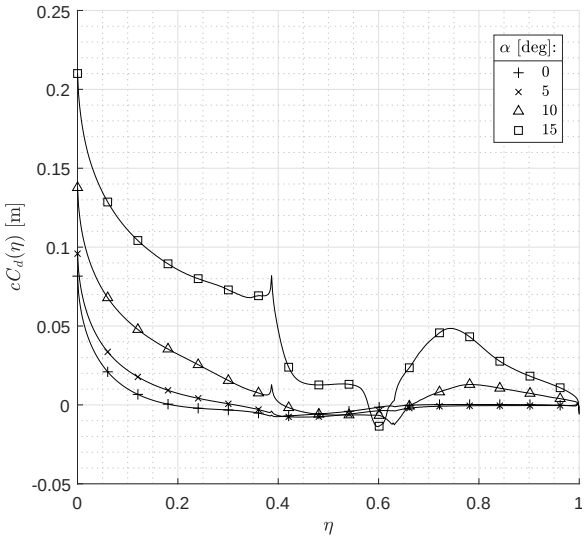

Figure 4.30: Spanwise distribution. Drag load distribution. $\alpha \in [5; 20]$ degrees.

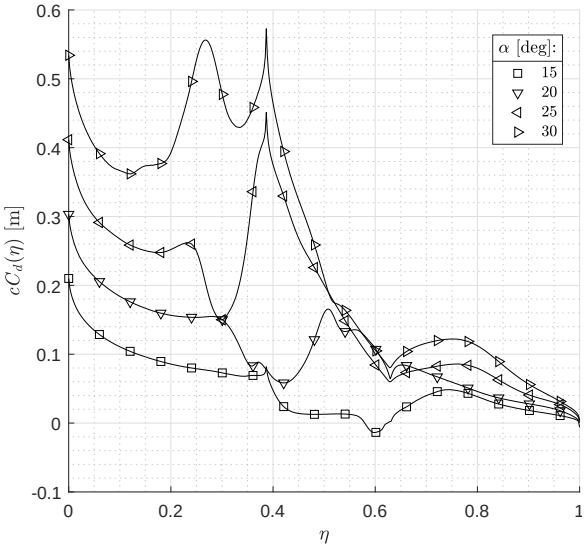

Figure 4.31: Spanwise distribution. Drag load distribution.
$\alpha \in [20; 35]$ degrees.

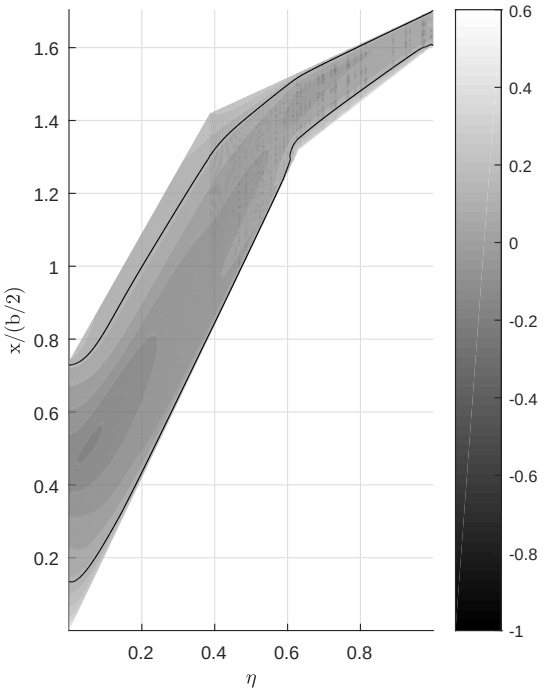

Figure 4.32: C_P contour on the suction side.
Black edge: contour line at $C_P = 0$.
$\alpha = 0$ degrees.

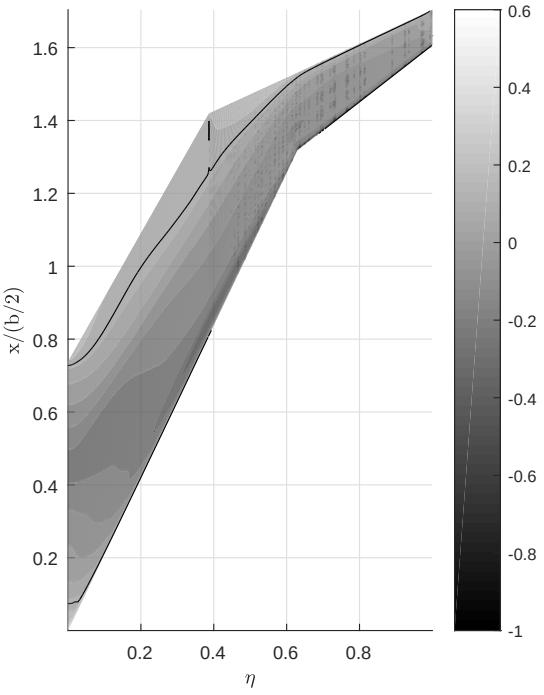

Figure 4.33: C_P contour on the suction side.
Black edge: contour line at $C_P = 0$.
$\alpha = 5$ degrees.

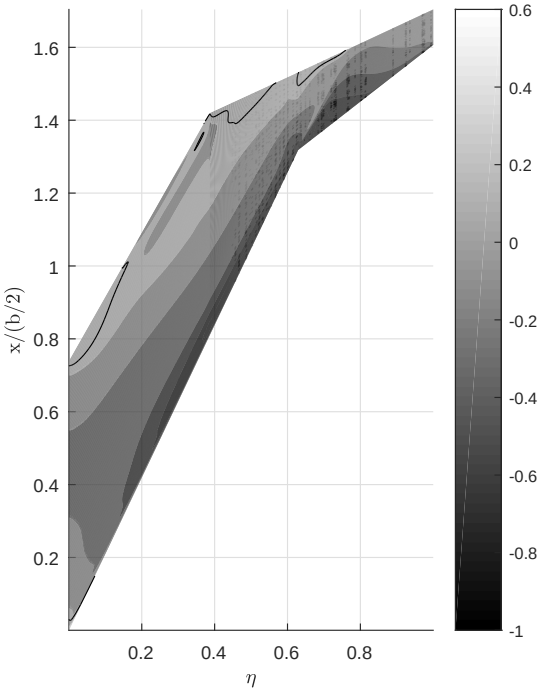

Figure 4.34: C_P contour on the suction side.
Black edge: contour line at $C_P = 0$.
α = 10 degrees.

4.3. Flight Mechanic Analyses

Trim analyses are performed using the developed trim algorithm to estimate the conditions in which the model can be trimmed based on the collected wind tunnel data. The aircraft is attempted to be trimmed in an range of airspeed between 15 and 40 m/s. Therefore, the wind tunnel data are assumed to be independent on the Reynolds number. The range of airspeed used for trimming the aircraft has been selected based on the requirement set by the incoming European regulations of flying in line of sight. All the analyses assumed ISA sea level conditions. The third control surface of the Flying V is left unused in the performed analyses foreseeing the need of using it for roll control and it has been proved to present the smallest pitching moment control authority from the previously presented aerodynamic data.

In the current section the following activities are presented:

- Identification of an optimal center of gravity to maximize the lift coefficient for a stable Flying V scaled model.

- Estimation of the influence of the center of gravity on the maximum lift coefficient achievable in trimmed horizontal steady state flight conditions using the two inboard control surfaces of the model as pure elevators.

- Estimation of the influence of the center of gravity on the maximum lift coefficient achievable in trimmed horizontal steady state flight conditions by sweeping the CSDR parameter to estimate the effects of lowering the pitching moment control authority.

4.3.1. Identification Optimal Center of Gravity Location

The *optimal location* of the center of gravity for the Flying V to maximize the trimmed lift coefficient achievable in trimmed conditions is evaluated using the optimization routine presented in the Chapter 2. An unitary CSDR is selected to make use of the maximum available longitudinal control authority. The $C_{M_\alpha}\big|_{\text{Ref}}$ used is equal to -0.0015 [1/deg], which corresponds to a -4.4% ultimate static stability margin, -3.6 cm. According to Donlan [10] ultimate static margins from -0.08 to -0.02 are reasonable for tailless airplanes.

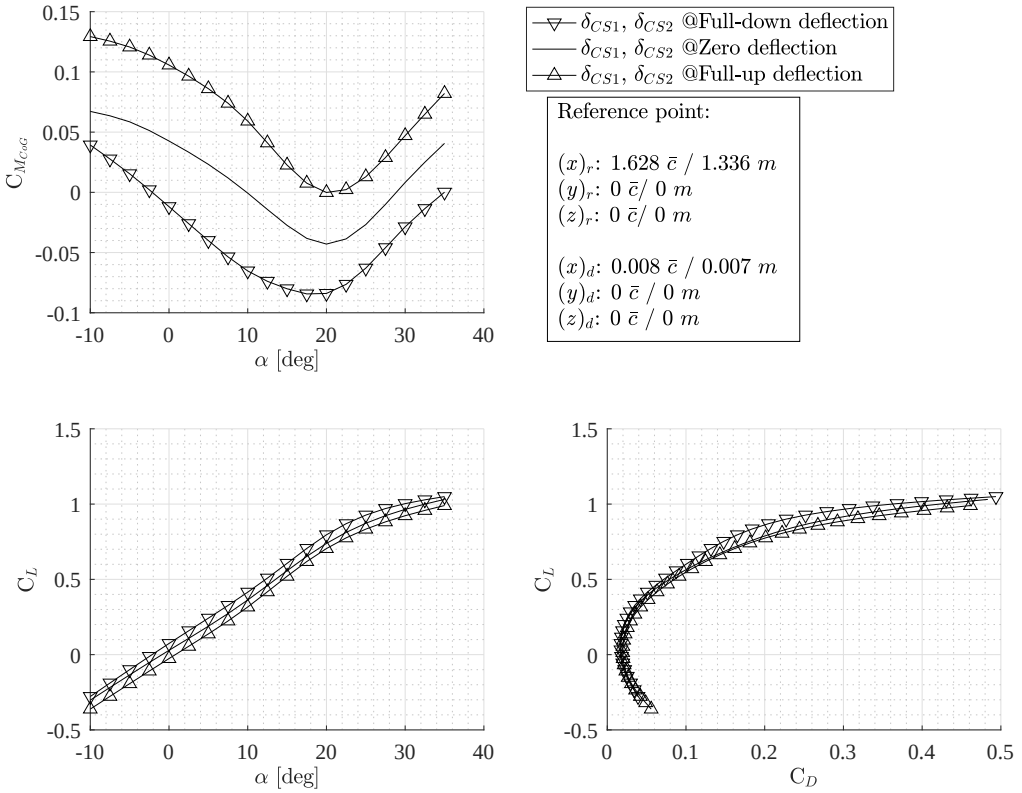

Figure 4.35: Aerodynamic characteristics of the Flying V with the center of gravity located at the optimal location.

The optimal longitudinal position of the center of gravity to achieve the maximum lift coefficient is located at a longitudinal position about to the leading edge of the mean geometric chord, 1.336 m from the nose of the aircraft, 0.008 $\bar{c}$ from the leading edge of the mean geometric chord of the model.

The pitching, lift and drag characteristics of the Flying V with a center of gravity located in the proposed location are presented in Fig. 4.35 for the cases of full-up, null and full-down deflections of the two inner control surfaces. The pitch-up break tendency of the configuration is clearly visible at about 20 degrees angle of attack for all the deflections of the control surfaces. The full-up deflection data are representative of the pitching moment polar curve that leads the Flying V model to its maximum lift coefficient in trimmed and stable conditions at about 20 degrees, based on the available wind tunnel data. Although a pitch-up break tendency is present, control power is still available which allows the model to be recovered if immediate action is taken.

A comparison between the clean and trimmed lift and drag characteristics of the Flying V is presented in Fig. 4.36 and 4.37. The trimmed lift polar presents larger lift coefficients for angles of attack lower than 10 degrees with respect to the clean lift polar curve, and lower for angles of attack larger than 10 degrees, which is a direct consequence of the deflections required for trimming the aircraft. From the pitching moment characteristics

in Fig. 4.35, it can be noticed that the proposed optimal center of gravity location makes the use of positive deflections of the control surfaces to trim the model in the angles of attack range between 0 and 10 degrees and of negative deflections of the control surfaces to trim the model in the angles of attack range between 10 and about 20 degrees.

The effect on the trimmed drag polar consists of lower drag at low lift coefficients in trim conditions, up to $C_L \approx 0.4$, and larger drag at higher lift coefficients with respect to the clean polar data. For C_L values lower than about 0.4, the control surfaces do generate lift to balance the aerodynamic moment of the aircraft about the center of gravity, therefore a lower angle of attack of the wing is required to achieve the $C_{L_{\text{trim}}}$ at a given airspeed. For C_L values larger than about 0.4, the control surfaces do generate downforce to balance the aerodynamic moment of the aircraft about the center of gravity, therefore a larger angle of attack of the wing is required to achieve the $C_{L_{\text{trim}}}$ at a given airspeed.

The aerodynamic efficiency in trimmed conditions is reported in Fig. 4.38, a maximum value about 10.4 is observed at a lift coefficient about 0.22. The trimmed drag plot versus airspeed and airspeed versus trimmed lift are presented in Fig. 4.39 to identify the range of airspeed in which the model is unstable for negative airspeed disturbances. Based on the available data, the model will be unstable for negative variation up to 31 m/s.

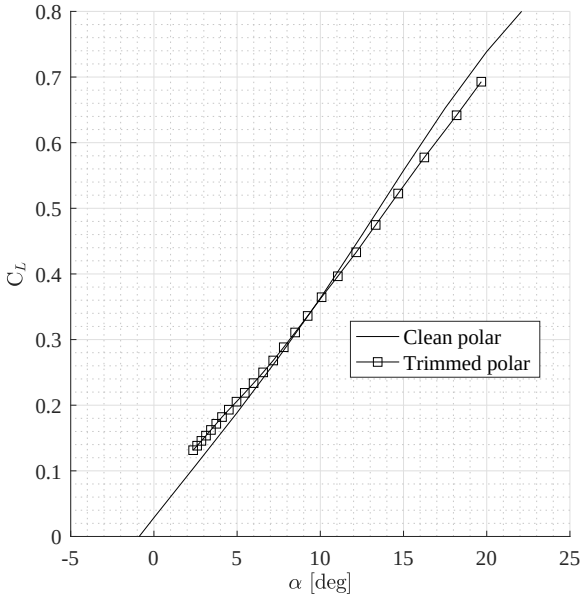

Figure 4.36: Comparison clean and trimmed C_L versus α.

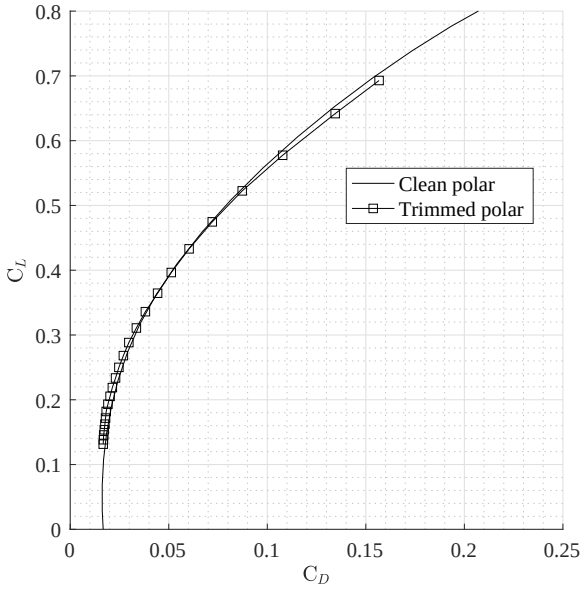

Figure 4.37: Comparison clean and trimmed C_L versus C_D.

4.3.2. Center of Gravity Influence on Max Trimmed Lift Coefficient

A parametric study is performed to estimate the effects of the longitudinal location of the center of gravity on the maximum lift coefficient achievable in trim conditions.

The evaluations of the center of gravity effects on the maximum lift coefficients are here estimated assuming an unitary CSDR and an ultimate stability margin equal to -4.4%, the same used during for the identification of the optimal center of gravity location. To highlight the potentialities of designing an unstable flying wing, the same analyses are performed without any stability requirements thus allowing the trim algorithm to trim the aircraft in unstable equilibrium points.

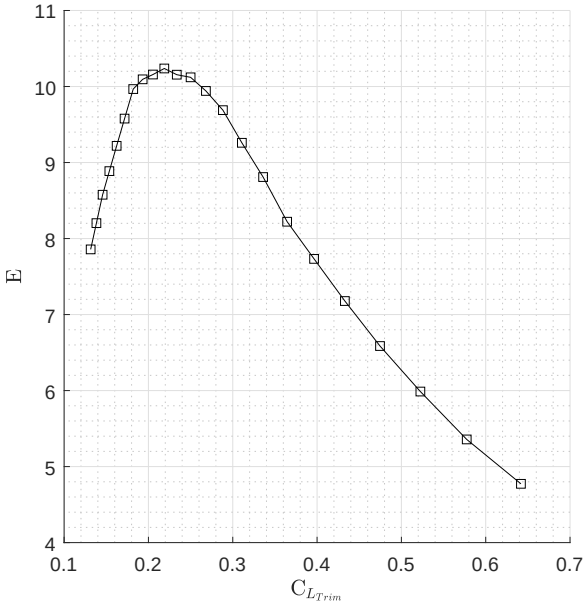

Figure 4.38: Comparison clean and trimmed C_L versus α.

The study allows to quantify the variation in terms of max trimmed lift coefficient caused by a shift of the center of gravity away from the identified optimal location, therefore to propose a most forward and aft locations of the center of gravity. The center of gravity is assumed to lay in the symmetry plane of the model. The longitudinal location of center of gravity is shifted in the range from 1.0 to 1.5 meters from the nose of the aircraft, from -0.4 $\bar{c}$ to about 0.2 $\bar{c}$ with respect to the projection of the leading edge of the mean geometric chord on the symmetry plane of the model.

The results are presented in Fig. 4.40, in which: maximum and minimum trimmed lift coefficients, trimmed drag coefficients and pitching moment derivative with respect to the angle of attack are presented at minimum and maximum lift as functions of the location of the center of gravity. In Fig. 4.41, the trim algorithm variables, α, $\%\delta_{CS1}$, and $\%\delta_{CS2}$, are presented in the estimated trim conditions at maximum and minimum lift coefficient.

Stable model configuration. Equilibrium points are identified within the range of investigated airspeed to identify the effects of center of gravity shifting in stable conditions on the maximum trimmed lift coefficient. Results are presented in Fig. 4.40. The influence of the center of gravity location on the maximum trimmed lift coefficients for a stable Flying V model is presented by identifying three sub-intervals of the analyzed center of gravity locations:

- *Forward positions*:
  - $(\bar{x}_{CoG})_d \in$ [-0.4; 0]
  - $(x_{CoG})_r \in$ [1.0; 1.33] m

  Towards the left side of this CoG locations interval the maximum trimmed lift coefficients are limited by large static stability characteristics of the configuration caused by the large distance between the center of gravity and the aerodynamic center: the available control power cannot withstand the nose-down pitching moment. In this region, the maximum trim lift coefficient increases as the center of gravity is aft-shifted thanks to the decrease in magnitude of C_{M_α}.

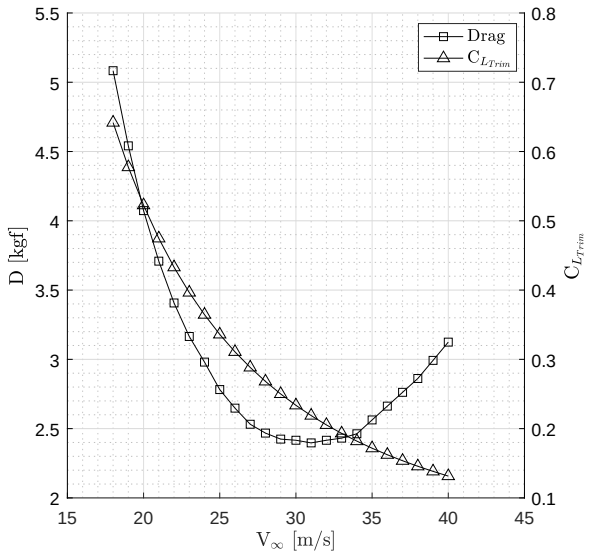

Figure 4.39: Drag versus flight speed in MTOM configuration (on the left axis). Flight speed versus lift coefficient in trim conditions in MTOM configuration (on the right axis).

- *Central locations*:
  - $(\bar{x}_{CoG})_d \in [0; 0.08]$
  - $(x_{CoG})_r \in [1.33; 1.39]$ m

  In this region the center of gravity effect turns into a reduction of maximum trimmed lift coefficient as the center of gravity location is aft-shifted. The reduction in maximum trimmed lift coefficient is caused by the reduction of static stability margin due to the aft-shifting of the center of gravity: to respect the constraint set on the stability margin, the maximum angle of attack has to reduce as the center of gravity is aft-shifted and so does the maximum lift coefficient. By recalling the trend of the aerodynamic center longitudinal positions with the angle of attack, presented in Fig. 4.7, the aerodynamic center quickly shifts forward between 15 and 20 degrees angle of attack.

- *Aft locations*:
  - $(\bar{x}_{CoG})_d \in [0.08; 0.12]$
  - $(x_{CoG})_r \in [1.39; 1.43]$ m

  As for the previous interval, the maximum trimmed lift coefficient reduces as the center of gravity aft-shifts. A steep reduction in maximum trimmed lift coefficient takes place for center of gravity locations next to the lower bound of the aft positions interval. The steep reduction is caused by the approaching of the center of gravity location to the zone in which the aerodynamic center is located in the angle of attack range within 0 and 10 degrees, $(x_{AC}) \approx 1.45$ m from the nose of the model, about 0.14 $\bar{c}$ from the leading edge of the mean geometric chord.

Unstable model configuration Equilibrium points are identified within the range of investigated airspeed to identify the effects of center of gravity shifting in unstable conditions on the maximum trimmed lift coefficient. When unstable equilibrium conditions are not identified, if possible, the equilibrium point is the stable one. The results are presented in Fig. 4.40. The influence of the center of gravity location on the maximum trimmed lift coefficients for an unstable Flying V model is presented by identifying three sub-intervals of the

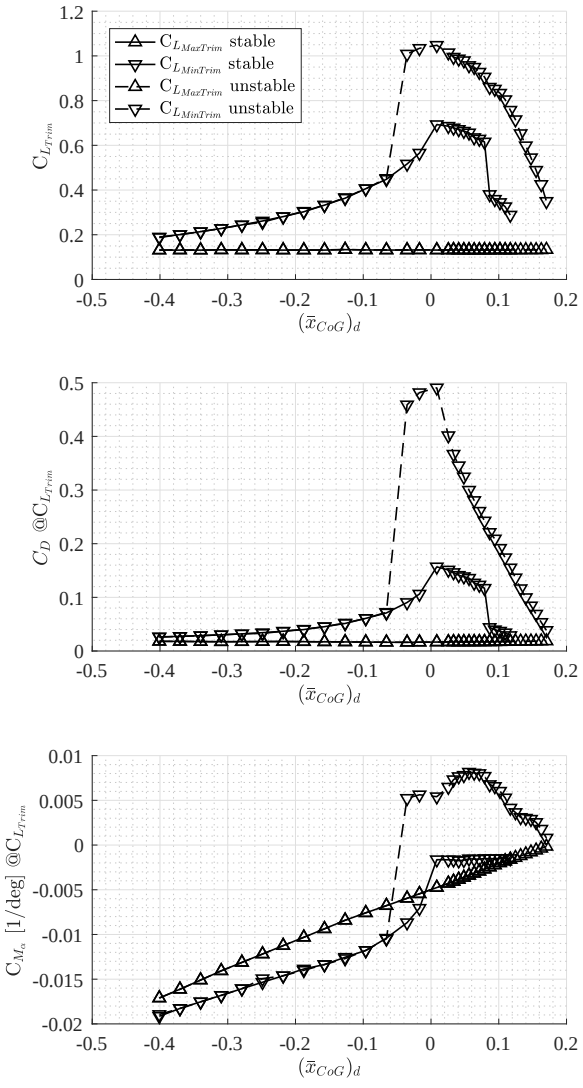

Figure 4.40: CoG effects on C_L, C_D, and C_{M_α} in trim conditions.

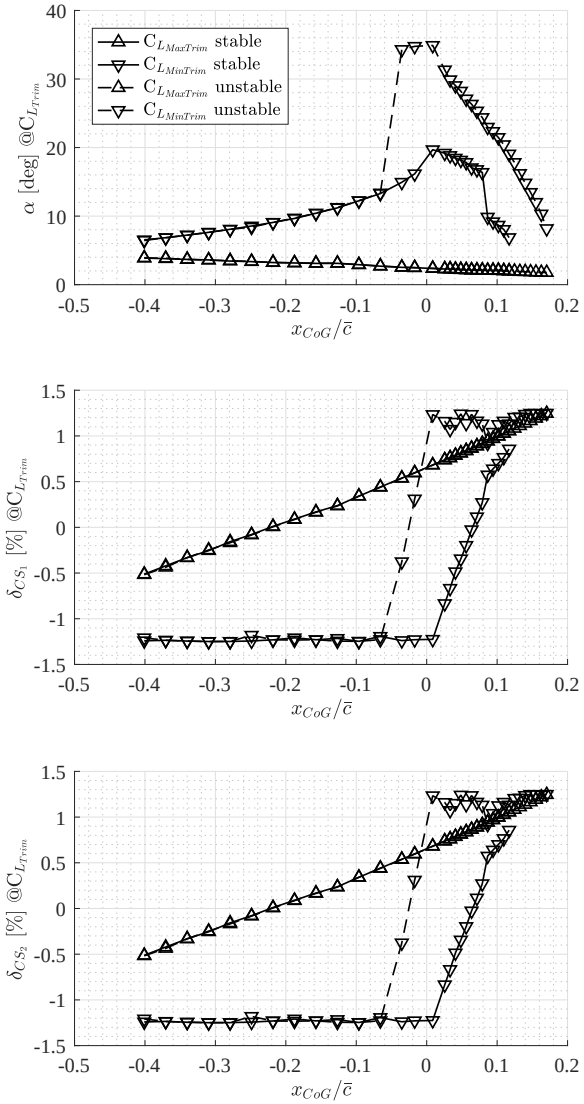

Figure 4.41: CoG effects on α, δ_{CS1}, and δ_{CS1} in trim conditions.

analyzed center of gravity locations:

- *Forward positions*:
  - $(\bar{x}_{CoG})_d \in$ [-0.4; -0.04]
  - $(x_{CoG})_r \in$ [1.0; 1.33] m

  The curve of maximum lift coefficient is overlapped with the curve relative to the stable configuration. Greater longitudinal control authority is required to achieve equilibrium in unstable conditions in this range. The data to support this statement are reported in Fig. B.1.

- *Central locations*:
  - $(\bar{x}_{CoG})_d \in$ [-0.04; 0.008]
  - $(x_{CoG})_r \in$ [1.33; 1.336] m

  The curve of maximum lift coefficient highlights the potentialities of flying in unstable conditions.

Within this interval of center of gravity locations, maximum lift coefficient values between 0.8 and 1.05 can be achieved. By comparing the maximum lift coefficient in stable and unstable conditions for a center of gravity located at the previously identified optimal CoG location, about 50% more lift can be produced by the unstable configuration ($C_L \approx 1.05$) with respect to the maximum lift coefficient achievable in a statically stable equilibrium condition ($C_L \approx 0.7$). On the drag coefficient the unstable model ($C_D \approx 0.48$) presents a value about 300% larger than the value relative to the stable model ($C_D \approx 0.16$).

- *Aft locations*:
  - $(\bar{x}_{CoG})_d \in [0.008; 0.164]$
  - $(x_{CoG})_r \in [1.336; 1.464]$ m

  The maximum lift coefficient trend highlight the increment pitching moment derivative at high angles of attack, which is also presented in the support material in Fig. B.3 and B.4. As the available control authority is constant, and the configuration becomes more and more unstable lower angles of attack can be trimmed. Still larger lift coefficients than for the stable configurations can be achieved per each center of gravity location.

4.3.3. Identification Most Forward and Aft Center of Gravity Location for a Stable SSFT Model

By selecting the three center of gravity locations relative to the bounds of the central locations and aft locations intervals, and a point belonging to the forward locations interval, the curves $C_{M_\alpha} - \alpha$, $\%\delta_{CS} - \alpha$, $V_\infty - \alpha$ are calculated in trimmed conditions. These curves are presented per each one of the above mentioned center of gravity sample locations in Fig. 4.42 (a).

As already presented, the center of gravity locations belonging to the central locations interval can achieve the largest maximum trimmed lift coefficient compared to those of the other intervals, therefore achieve the lowest values in terms of minimum airspeed required to trim the aircraft. The two bounds of the central locations of the center of gravity are therefore proposed as the most forward and aft locations as these locations comply with the requirement of landing operations at airspeed lower than 20 m/s, which has been set during the preliminary calculations presented in Chapter 2.

As observable in the trim diagram relative to the proposed most forward and aft center of gravity locations in Fig. 4.42 (b), during future SSFT activities:

- To trim the flying model with the center of gravity located in the most forward CoG position, the required deflections are positive for lift coefficient values lower than 0.4 (angles of attack lower than 10 degrees), and negative for lift coefficient larger than 0.4, observable in Fig. 4.42 (a), $\%\delta_{CS} - \alpha$ plot.
- To trim the flying model with the center of gravity located in the most aft CoG position, positive deflections are required to trim the model from low to high angles of attack. In the $\%\delta_{CS} - \alpha$ plot presented in Fig. 4.42 (a): the remote control input required to trim the model at the largest angle of attack is 40% while to trim at the lowest angle of attack the input required is equal to 90%. The relatively small difference between the remote control inputs required to trim the Flying V model during future SSFT activities at low and high attitudes might increase the complexity of remotely piloting the model.

Finally, the effects of full positive or negative deflections of the first and second control surfaces on the $C_L - C_M$ curve are clearly observable in Fig. 4.42 (b). In general the lines relative to full positive and full negative

deflections cannot be overlapped and it is clearly visible they have different derivatives with respect to the lift coefficient. This highlights the influence of the inboard and central control surfaces on the derivative of the pitching moment coefficient with respect to the lift coefficient. Although the magnitude is independent on the center of gravity location, these effects are more evident when considering the most aft location due to greater variation in percentage of the static stability margin due to a deflection of the control surfaces.

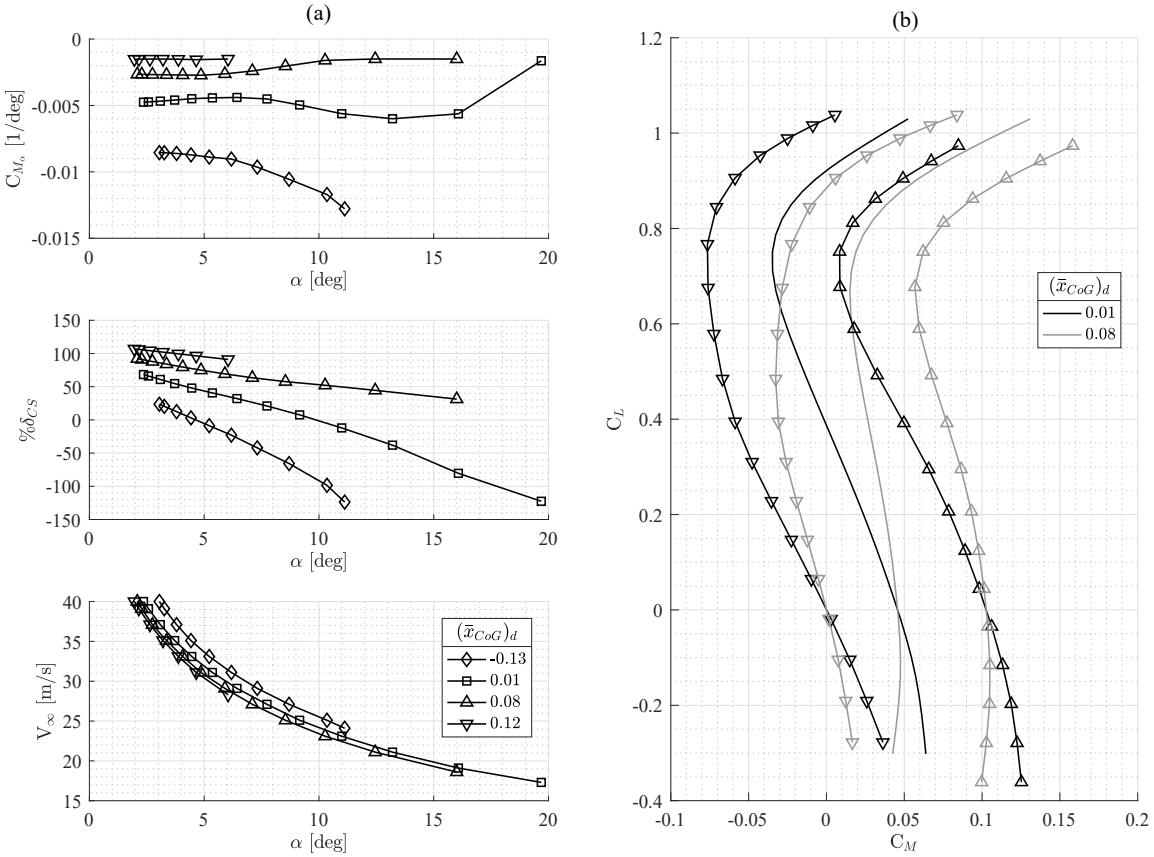

Figure 4.42: **(a)**: C_{M_α}, $\%\delta_{CS}$, V_∞ vs α for different CoG locations in trim conditions. **(b)**: Trim diagrams of the proposed most forward and aft CoG locations for an unitary value of CSDR. Solid lines: null deflections. Triangles up lines: first and second control surfaces deflected fully upwards.

4.3.4. CoG Longitudinal Location and CSDR Effects on Max Trimmed Lift Coefficient

The combined effects of center of gravity locations and control surface deflection ratio are here presented to analyze the influence of using not unitary gains between the deflections of the inboard and central control surfaces.

The analysis is performed by shifting the center of gravity location on the symmetry plane of the model. The center of gravity location ranges between the leading edge point of the mean geometric chord and the center of gravity proposed by Faggiano [2]. The latter is representative of a very aft location of the center of gravity that, in case longitudinal static stability is required, negatively affects the maximum lift coefficient achievable as previously presented.

The control surface deflection ratio is varied between in the range CSDR $\in [0; 4]$. Negative values are not taken into account as those would reduce the maximum achievable lift coefficient in trimmed conditions: the two

control surfaces would produce pitching moments opposite in sign.

$$\%\delta_{CS1} = \text{CSDR}\,\%\delta_{CS2} \tag{4.4}$$

Firstly, the analyses are performed using the same static requirement as in the previously performed analyses conducted with an unitary values of CSDR: $C_{M_\alpha} - 1.5 \cdot 10^{-3}$ [1/deg]. The results of the analyses are presented in Fig.4.43 and 4.44. Fig.4.43 is divided in two columns of sub-plots. The left column present to present the maximum and minimum lift coefficient achievable per each values of center of gravity longitudinal position and CSDR in the selected ranges lift coefficient, drag coefficient, and static stability margin at maximum and minimum trimmed lift coefficients. Fig.4.44 is divided in two columns of sub-plots to present the angle of attack, required deflection of CS1 and required deflection of CS2 at maximum and minimum trimmed lift coefficient.

Fig.4.45 and 4.46 present the results of the same analysis performed without any stability requirement in the same center of gravity and CSDR ranges. The analyses are also performed with the static stability requirement completely released to identify the CSDR ranges in which the aircraft cannot be trimmed due to lack of control authority.

In Fig.4.43, a region of maximum lift coefficients is identified with lift coefficients larger or equal to 0.69 when the center of gravity is in the range $(\bar{x}_{\text{CoG}})_d \in [0,\ 0.04]$. The identified optimal location, evaluated using an unitary CSDR, represents the most forward position of the center of gravity of the model which belongs to the range of longitudinal positions and CSDR that allow to maximize the lift coefficient in trimmed conditions. If CSDR values different from an unitary value are considered, a maximum lift coefficient about 0.69 can still be achieved for some combination of CSDR and longitudinal location of the center of gravity. However the center of gravity would have to be aft shifted, thus reducing the distance between the most aft and forward center of gravity locations.

By forward or aft-shifting the center of gravity, reductions in max trimmed lift coefficient take place at fixed CSDR values. The reduction is faster when the center of gravity is shifted forward due to lack of control authority. By aft-shifting the center of gravity location, the maximum trimmed lift coefficients decrease due to the set stability requirement, as observable in the MSS-plot at max lift coefficient in Fig.4.43.

According to these observations, a region of very aft-center of gravity location can be identified when $(\bar{x}_{\text{CoG}})_d$ is greater than 0.08. In this region a fast reduction in max trimmed lift coefficient takes place, this region might be considered as a bound for aft-locations of the center of gravity during sub-scaled flight test activities as aft-shifts would result in drastic reductions in max lift coefficients due to the approaching of the center of gravity to the aerodynamic center of the aircraft.

The range of center of gravity locations in $(\bar{x}_{\text{CoG}})_d \in [0.08;\ 0.15]$ is of poor interest as the maximum trimmed lift coefficient decrease to lift coefficient values about 0.4. By merging the information from Fig. 4.43 and 4.44 with those from Fig.4.45 and Fig.4.46, the reason for the blanked areas can be identified:

- CSDR > 1.5: stability requirement not satisfied.
- CSDR < 0.8: stability requirement not satisfied and then lack of control authority.

Trim conditions at the largest considered airspeed can be achieved for any combinations of control surface deflection ratio when $(\bar{x}_{\text{CoG}})_d \in [0, 0.09]$, although for CSDR values in [0; 0.5] and [2; 4] the minimum lift coefficients achievable in trimmed conditions increase due to a progressive reduction of longitudinal control authority.

Very aft locations of the center of gravity, $(\bar{x}_{\mathrm{CoG}})_d > 0.09$, do not satisfy the stability requirement as observable in the MSS at minimum lift coefficient in Fig.4.43.

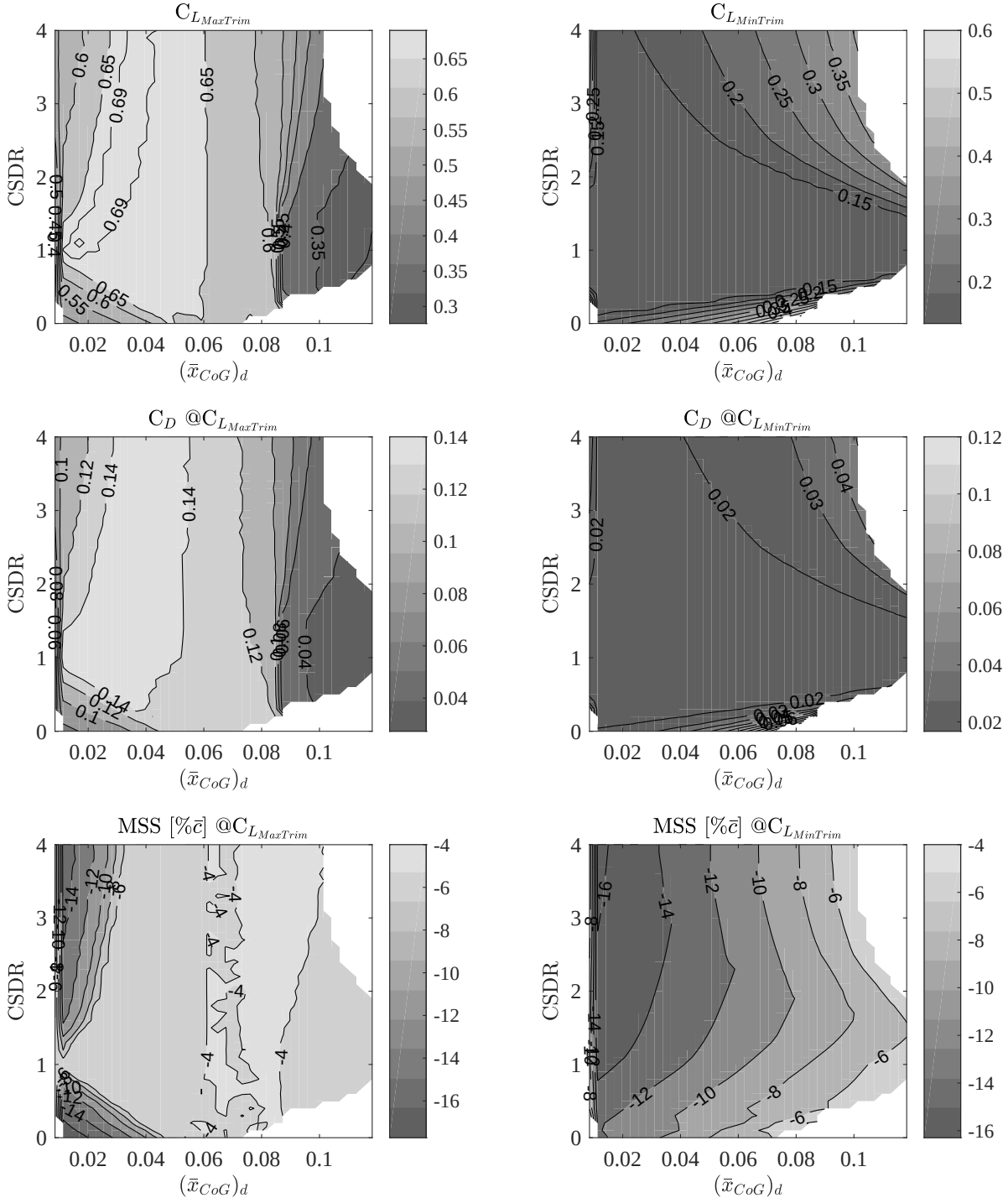

Figure 4.43: Trim algorithm variables at maximum and minimum trimmed lift coefficient.

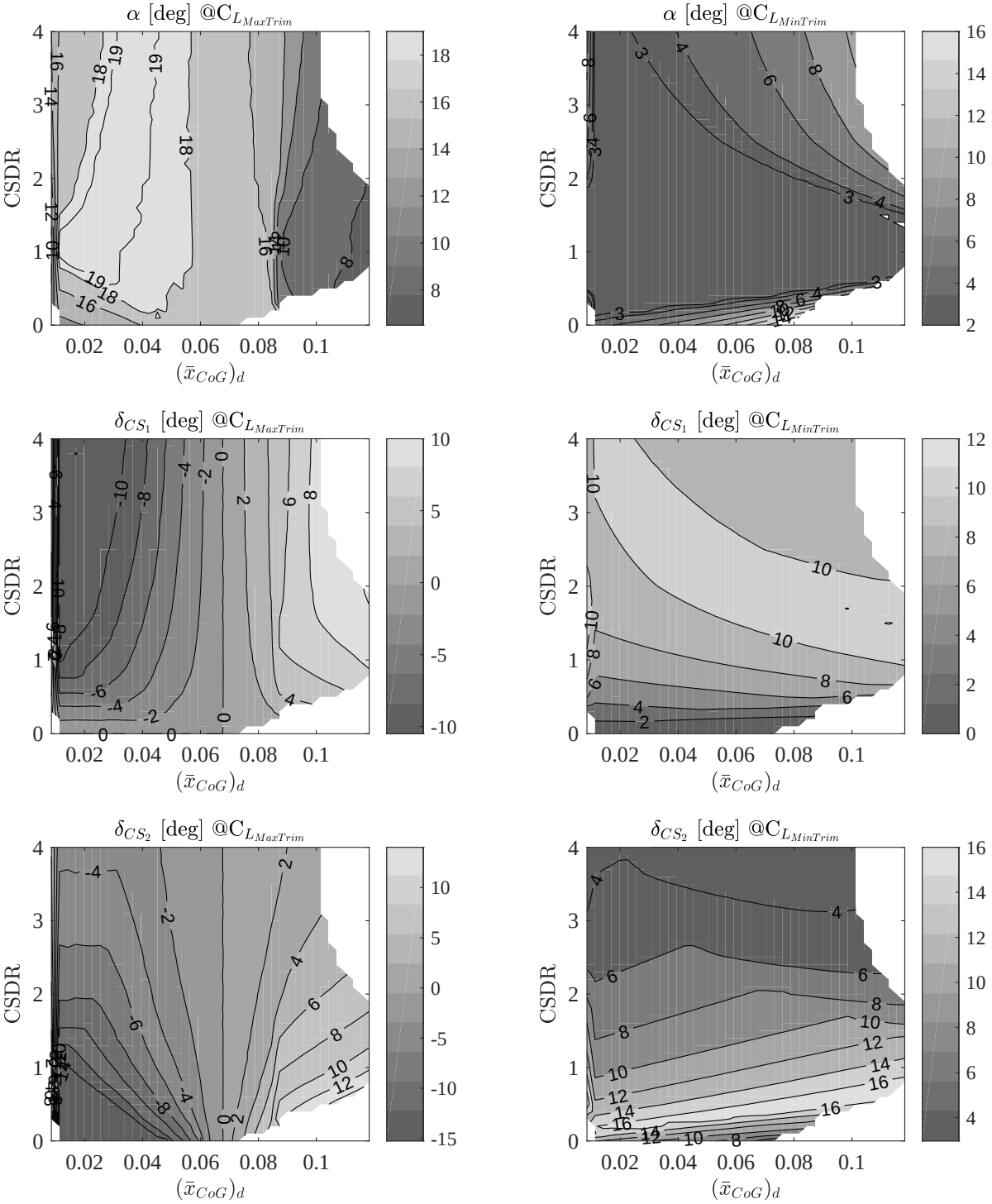

Figure 4.44: Trim algorithm variables at maximum and minimum trimmed lift coefficient.

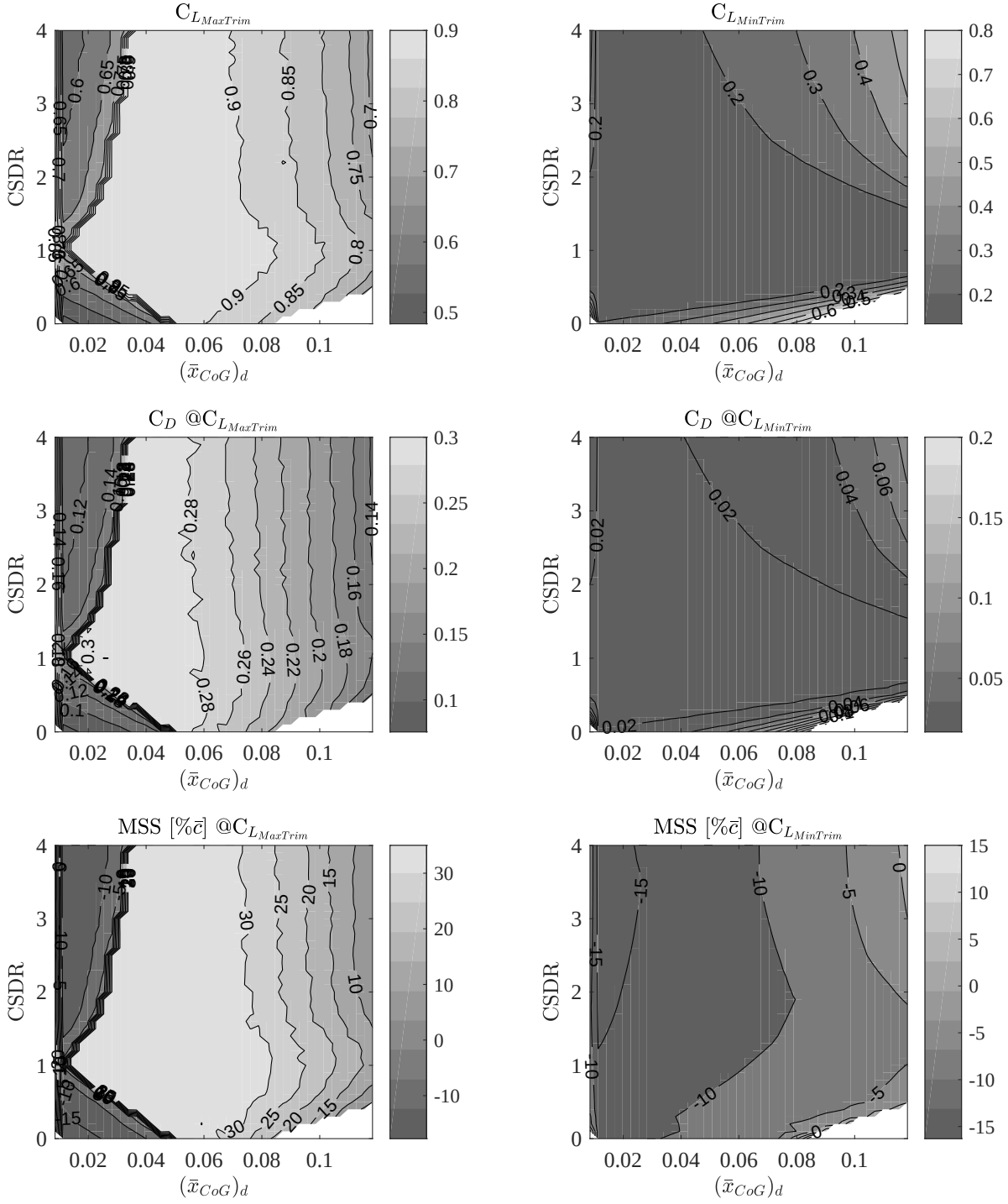

Figure 4.45: Trim algorithm variables at maximum and minimum trimmed lift coefficient.

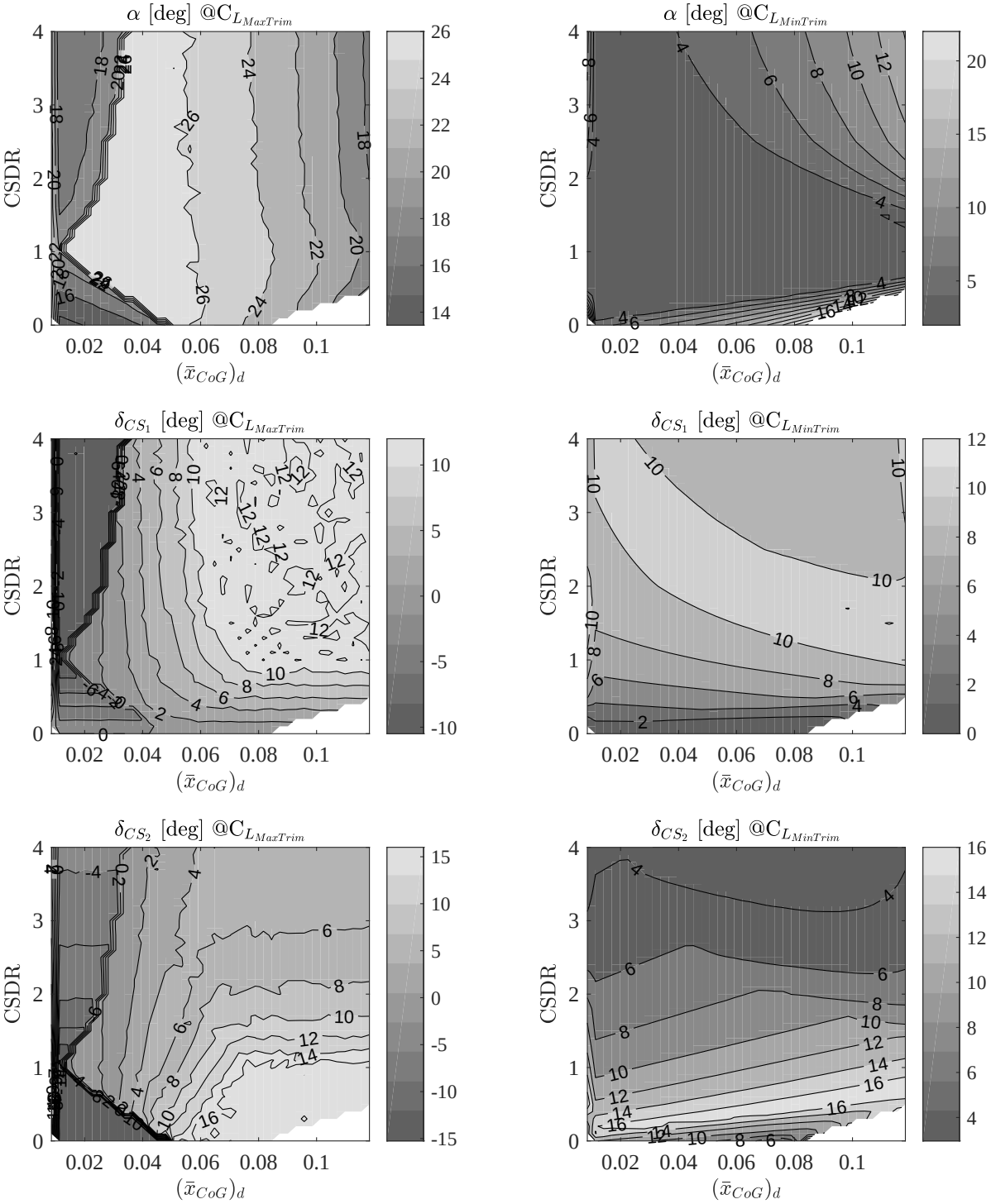

Figure 4.46: Trim algorithm variables at maximum and minimum trimmed lift coefficient.

5

Conclusions and Recommendations

The needed activities to perform the wind tunnel testing on the sub-scaled Flying V model have been presented in the report. The current design of the internal structure successfully sustained the loads during the wind tunnel tests up to about 310 Newton, equivalent to 2.5 g, and resisted longer than 200 hours of wind tunnel testing. The aerodynamic characteristics have been recorded and used to analyze the influence of the center of gravity on the maximum lift coefficient achievable in trimmed conditions. A parametric study is performed to assess whether the control surfaces are oversized or not. Finally, CFD simulations are performed to try to reproduce the recorded wind tunnel characteristics and get a better understanding of the aerodynamic phenomena taking place over the tested configuration at high angles of attack.

5.1. Conclusions

The aerodynamic characteristics of the tested model have been collected both in clean configuration and with the control surfaces deflected. Similar aerodynamic characteristics to low aspect ratio wings are identified for the Flying V scaled model, such as the presence of vortex lift and pitch-up break tendencies, can be identified from the collected wind tunnel data. No deep-stall characteristics are identified from the wind tunnel data as all the control surfaces never suffer of drastic loss of effectiveness within the entire range of tested angles of attack, from -10 to 35 degrees, both for positive and negative deflections.

The aerodynamic center of the half model and the effects of the control surfaces on its location are calculated. In clean configuration, the aerodynamic center of the tested model is located at null angle of attack at 1.42 meters from the nose of the aircraft in longitudinal position. For angles of attack between -10 and 20 degrees, the longitudinal position of the aerodynamic center moves in the range between 1.32 and 1.42 meters from the nose of the aircraft, about 11% $\bar{c}$ afterward with respect to the leading edge of the mean geometric chord of the vehicle. The effects of the deflections of the inboard and central control surfaces are estimated based on the collected dataset. In the range between 0 and 20 degrees, the combined deflections of the inboard and central control surfaces can induce the aerodynamic center to shift of about 5 centimeters, about 6% $\bar{c}$, in longitudinal direction, thus producing non negligible effects on the stability characteristics.

The optimal longitudinal location of the center of gravity of a 4.6% geometrically scaled flying model is iden-

tified to maximize the lift coefficient achievable in trimmed conditions under the requirement of ultimate static stability margin equal to -4.4% of the mean geometric chord. This position is located at 1.336 meters from the nose of the model, which is about the longitudinal position of the leading edge of the mean geometric chord of the wing. Trimmed polars are computed for a model flying with the center of gravity located at the optimal point and the maximum lift coefficient achievable in horizontal steady state flight is calculated to be about 0.7. In MTOM conditions, the airspeed required to fly at maximum lift coefficient is equal to 17.3 m/s, although statically stable on the pitching moment, at this attitude the flying wing would be unstable for negative airspeed disturbances. A maximum aerodynamic efficiency about 10.4 is estimated from the trimmed polars.

The influence of the longitudinal location of the center of gravity on the maximum lift coefficient achievable in trimmed condition is estimated assuming the use of the inboard and central control surfaces, CS1 and CS2, as pure elevators and an ultimate longitudinal static stability margin equal to -4.4% $\bar{c}$. Three ranges of center of gravity locations are identified for the statically stable configuration. The bounds of the "central locations" interval are proposed as most forward and aft center of gravity locations for future sub-scaled flight testing activities on the 4.6% scaled Flying V model. A statically stable flying model is foreseen to be able to achieve a maximum lift coefficient about 0.7 when the center of gravity located in the proposed most forward location, 1.33 meters from the nose of the configuration, and a maximum lift coefficient about 0.6 when the center of gravity is located in the proposed most aft location, 1.39 meters from the nose of the configuration.

A parametric study is performed to highlight whether the designed control surfaces are oversized for the pitching moment authority required to trim a flying model. The study highlights the effects of reducing the available pitching moment control authority on the maximum achievable lift coefficient in trimmed conditions in a range of longitudinal positions of the center of gravity. In general, by reducing the usable control authority, the maximum lift coefficient achievable in steady state horizontal flight conditions decreases. The most detrimental effects of a reduced control authority take place for forward center of gravity locations, $(\bar{x})_d \in [0;\ 0.03]$, by reducing the maximum lift coefficient achievable in trimmed conditions up to the 20% of the maximum lift coefficient achievable by making use of the entire available control authority and by locating the center of gravity in the optimal location.

The performed estimations identify the requirement of placing the center of gravity during future sub-scaled flight test activities within the range $(\bar{x})_d \in [0;\ 0.08]\ \bar{c}$. From the presented analyses, the same design of the control surfaces of the wind tunnel model is suggested to be used for the future SSFT model, in order to be able to trim the model at high angles of attack and reduce as much as possible the landing speed.

Finally, the performed numerical simulations highlighted challenges in reproducing aerodynamic flows over wing in presence of vortical structures. Three grids, featuring different refinements and topology of the elements, have been tested. Polyhedral grids present advantages with respect to tetrahedral grids in simulating vortical flows thanks to the larger number of faces of each cell. While on lift and drag characteristics the different grids produce similar results, different trends are observed at high angles of attack for tetrahedral and polyhedral grids. The lift characteristics have been reproduced with a maximum error about 9%. Larger discrepancies between numerical and experimental data are identified especially on the drag and pitching moment characteristics, and on the location of the aerodynamic center, as also found in literature. Vortical structures are identified around the wing and their effects on the aerodynamics of the investigated flying wing model are presented in terms of local pressure distributions on the different stations of the wing and as influence on the spanwise production of lift and drag.

5.2. Recommendations

The experimental study has estimated the in-flight characteristics based on the wind tunnel polars, much work has to be conducted for the development of the flying model to proceed towards the future steps of the project. A new wind tunnel campaign might be useful to estimate the aerodynamic characteristics of the model in "ground effects" and the integration effects of the landing gear system, of the engines, and of the winglets.

The control surfaces, with the current gearing ratio of the leverages, provide sufficient pitching moment to trim the aircraft up to lift coefficients about 0.7 by properly positioning the center of gravity. The deflections of the control surfaces might be increased to reduce the spanwise extension of the control surfaces. Hence, a caveat has to be given on increasing the deflections of the control surfaces as these have been noticed to influence the shift of the aerodynamic center of the Flying V configuration.

The RANS performed simulations using the Spalart-Allmaras turbulence model resulted in poor pitching moment estimation characteristics. Two researches [35, 48] suggest the use of SADES or LES to simulate vortex systems at higher angles of attack when vortex breakdown occurs.

Bibliography

[1] J Benad. Technical report: Design of a commercial aircraft for high-subsonic speed as a flying wing configuration. *Airbus*, 2015.

[2] Francesco Faggiano, Roelof Vos, Max Baan, and Reinier Van Dijk. Aerodynamic Design of a Flying V Aircraft. In *17th AIAA Aviation Technology, Integration, and Operations Conference*, page 3589, 2017.

[3] Ansys Documentation - Quality Measure. `https://www.sharcnet.ca/Software/Ansys/17.2/en-us/help/tgd_usr/tgd_user_report_qualitymeasure.html`, . Accessed: 01-01-2019.

[4] ANSYS Meshing Advanced Techniques, PADT Lunch & Learn Series. `http://www.padtinc.com/blog/wp-content/uploads/2017/04/Advanced-Techniques-in-ANSYS-Meshing_Blog.pdf`, . Accessed: 01-01-2019.

[5] R Martinez-Val. Flying wings. A new paradigm for civil aviation? *Acta Polytechnica*, 47(1), 2007.

[6] Bolsunovsky, AL and Buzoverya, NP and Gurevich, BI and Denisov, VE and Dunaevsky, AI and Shkadov, LM and Sonin, OV and Udzhuhu, AJ and Zhurihin, JP. Flying wing-problems and decisions. *Aircraft design*, 4(4):193–219, 2001.

[7] R Martinez-Val, E Perez, P Alfaro, and J Perez. Conceptual design of a medium size flying wing. *Proceedings of the Institution of Mechanical Engineers, Part G: Journal of Aerospace Engineering*, 221(1):57–66, 2007.

[8] Egbert Torenbeek. Blended-wing-body and all wing airliners. In *8th European Workshop on Aircraft Design Education*, 2007.

[9] Liebeck, Robert H. Design of the blended wing body subsonic transport. *Journal of aircraft*, 41(1):10–25, 2004.

[10] Donlan, Charles. An interim report on the stability and control of tailless airplanes. 1944.

[11] Mialon, Bruno and Fol, Thierry and Bonnaud, Cyril. Aerodynamic optimization of subsonic flying wing configurations. In *20th AIAA applied aerodynamics conference*, page 2931, 2002.

[12] Vassberg, John C and DeHaan, Mark A and Rivers, S Melissa and Wahls, Richard A. Development of a common research model for applied CFD validation studies. *AIAA paper*, 6919:2008, 2008.

[13] F.Bremmers L.C.Eveleens. Free flying scale model flight testing: future or fiction? In *NLR internal document*, 2016.

[14] Deck, Sébastien and Gand, Fabien and Brunet, Vincent and Khelil, Saloua Ben. High-fidelity simulations of unsteady civil aircraft aerodynamics: stakes and perspectives. Application of zonal detached eddy simulation. *Phil. Trans. R. Soc. A*, 372(2022):20130325, 2014.

[15] Jewel B Barlow, William H Rae, and Alan Pope. Low-speed wind tunnel testing. 1999.

[16] Daniel Kuehme, Nicholas R Alley, Caleb Phillips, and Bruce R Cogan. Flight Test Evaluation and System Identification of the Area-I Prototype-Technology-Evaluation Research Aircraft (PTERA). In *AIAA Flight Testing Conference*, page 2577, 2014.

[17] Thomas L Jordan and Roger M Bailey. NASA Langley's AirSTAR testbed: A subscale flight test capability for flight dynamics and control system experiments. In *AIAA Guidance, Navigation and Control Conference and Exhibit*, pages 18–21, 2008.

[18] Dan Vicroy. X-48b blended wing body ground to flight correlation update. 2011.

[19] Dan D Vicroy. Blended-wing-body low-speed flight dynamics: summary of ground tests and sample results. 2009.

[20] Chester H Wolowicz, JS Brown Jr, and William P Gilbert. Similitude requirements and scaling relationships as applied to model testing. 1979.

[21] Luuk van der Schaft. Development, Model Generation and Analysis of a Flying V Structure Concept. 2017.

[22] 'Prototype' Commission Regulation on Unmanned Aircraft Operations. `https://www.easa.europa.eu/sites/default/files/dfu/Explanatory%20Note%20for%20the%20UAS%20Prototype%20regulation%20final.pdf`. Accessed: 01-05-2018.

[23] Jan Roskam. *Airplane flight dynamics and automatic flight controls*. DARcorporation, 1998.

[24] Robert C Nelson. *Flight stability and automatic control*, volume 2. WCB/McGraw Hill New York, 1998.

[25] Agostino De Marco and Domenico P Coiro. Dinamica e simulazione di volo. 2015.

[26] Vladislav Klein and Eugene A. Morelli. *Aircraft System Identification: Theory and Practice*. American Institute of Aeronautics and Astronautics, Inc. 1801 Alexander Bell Drive, Reston, VA 20191, 2006.

[27] Dorobantu, Andrei and Murch, Austin and Mettler, Bérénice and Balas, Gary. System identification for small, low-cost, fixed-wing unmanned aircraft. *Journal of Aircraft*, 2013.

[28] Lundström, David and Sobron, Alejandro and Krus, Petter and Jouannet, Christopher and da Silva, Roberto Gil Annes. Subscale Flight Testing of a Generic Fighter Aircraft. In *30th Congress of the International Council of the Aeronautical Sciences (ICAS), September 25-30, Daejeon, South Korea*, 2016.

[29] Top view drawing Airbus A350-900 - Revision Date May 2012. `https://www.airbus.com/aircraft/support-services/airport-operations-and-technical-data/autocad-3-view-aircraft-drawings.html`. Accessed: 03-04-2018.

[30] S Eder, K Hufnagel, and C Tropea. Semi-span testing in wind tunnels. In *25th International Congress of the Aeronautical Sciences: ICAS*, pages 1–9, 2006.

[31] SN Skinner and H Zare-Behtash. Semi-span wind tunnel testing without conventional peniche. *Experiments in Fluids*, 58(12):163, 2017.

[32] H.J. Alons. OJF External Balance documentation. Technical report, NLR, 2008.

[33] ANSYS Fluent Mosaic Technology with Polyhedral Elements for Fast and Accurate Flow Resolution. https://www.simutechgroup.com/images/easyblog_articles/7/ANSYS-Fluent-Mosaic-Technology-Automatically-Combines-Disparate-Meshes-with-Polyhedral-Elements-fo pdf, . Accessed: 01-01-2019.

[34] Spalart, PRaA and Allmaras, S1. A one-equation turbulence model for aerodynamic flows. In *30th aerospace sciences meeting and exhibit*, page 439, 1992.

[35] Huber, Kerstin and Schutte, Andreas and Rein, Martin. Numerical investigation of the aerodynamic properties of a flying wing configuration. In *30th AIAA Applied Aerodynamics Conference*, page 3325, 2012.

[36] Dacles-Mariani, Jennifer and Zilliac, Gregory G and Chow, Jim S and Bradshaw, Peter. Numerical/experimental study of a wingtip vortex in the near field. *AIAA journal*, 33(9):1561–1568, 1995.

[37] Stokkermans, Tom C and Arnhem, Nando v and Sinnige, Tomas and Veldhuis, Leo L. Validation and Comparison of RANS Propeller Modeling Methods for Tip-Mounted Applications. In *2018 AIAA Aerospace Sciences Meeting*, page 0542, 2018.

[38] Spalart, Philippe R and Rumsey, Christopher L. Effective inflow conditions for turbulence models in aerodynamic calculations. *AIAA journal*, 45(10):2544–2553, 2007.

[39] Keating, Mark and Principal Engineer, ANSYS. Accelerating CFD solutions. 2011.

[40] Daniel C Garmendia and Dimitri N Mavris. Alternative trim analysis formulations for vehicles with redundant multi-axis control surfaces. *Journal of Aircraft*, 2015.

[41] Neyman, Jerzy. X-Outline of a Theory of Statistical Estimation Based on the Classical Theory of Probability. *Phil. Trans. R. Soc. Lond. A*, 236(767):333–380, 1937.

[42] Ansys Documentation - Maximum Corner Angle. https://www.sharcnet.ca/Software/Ansys/16.2.3/en-us/help/wb_msh/msh_max_corner_angle.html, . Accessed: 01-01-2019.

[43] Ansys Documentation - Mesh Orthogonal Quality. https://www.sharcnet.ca/Software/Ansys/16.2.3/en-us/help/wb_msh/msh_orthogonal_quality.html, . Accessed: 01-01-2019.

[44] ANSYS Documentation - Monitoring Residuals: Definition of Residuals for the Pressure-Based Solver. http://www.padtinc.com/blog/wp-content/uploads/2017/04/Advanced-Techniques-in-ANSYS-Meshing_Blog.pdf, . Accessed: 01-01-2019.

[45] Jeong, Jinhee and Hussain, Fazle. On the identification of a vortex. *Journal of fluid mechanics*, 285:69–94, 1995.

[46] Hansen, Charles D and Johnson, Chris R. *Visualization handbook*. Elsevier, 2011.

[47] Ed Obert. *Aerodynamic design of transport aircraft*. IOS press, 2009.

[48] Morton, Scott and Forsythe, James and Mitchell, Anthony and Hajek, David. DES and RANS simulations of delta wing vortical flows. In *40th AIAA Aerospace Sciences Meeting & Exhibit*, page 587, 2002.

Appendices

A

Appendix A

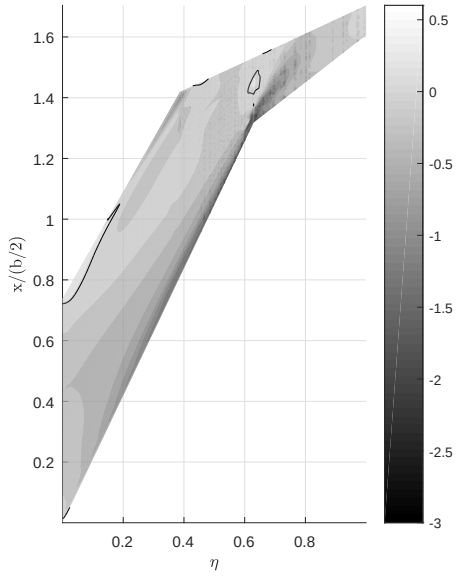

Figure A.1: C_P contour on the suction side.
Black edge: contour line at $C_P = 0$.
α = 15 degrees.

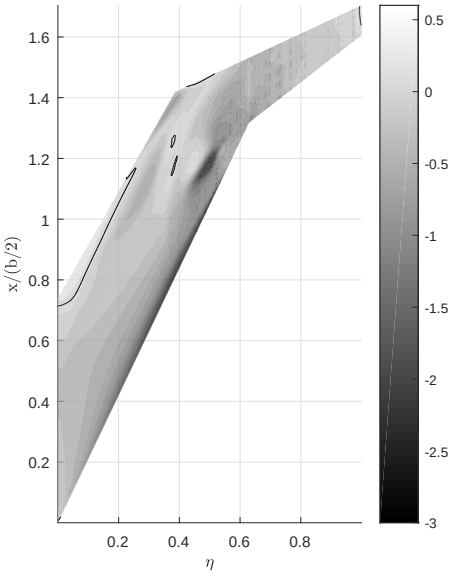

Figure A.2: C_P contour on the suction side.
Black edge: contour line at $C_P = 0$.
α = 20 degrees.

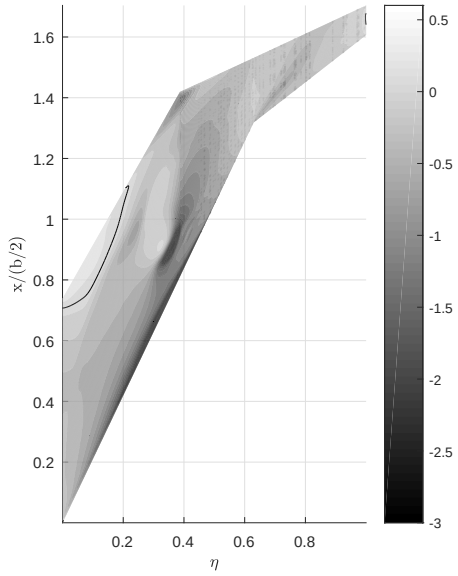

Figure A.3: C_P contour on the suction side.
Black edge: contour line at $C_P = 0$.
α = 25 degrees.

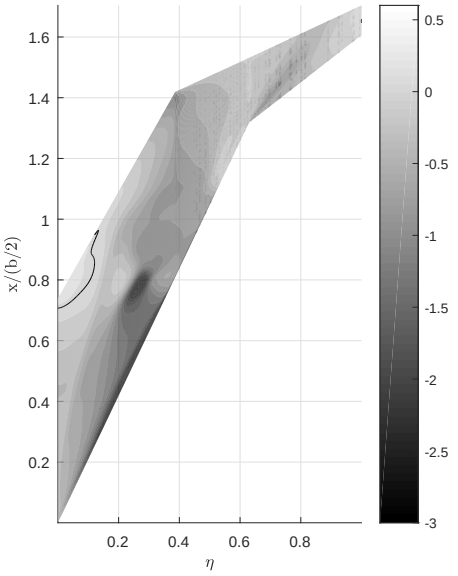

Figure A.4: C_P contour on the suction side.
Black edge: contour line at $C_P = 0$.
α = 30 degrees.

B

Appendix B

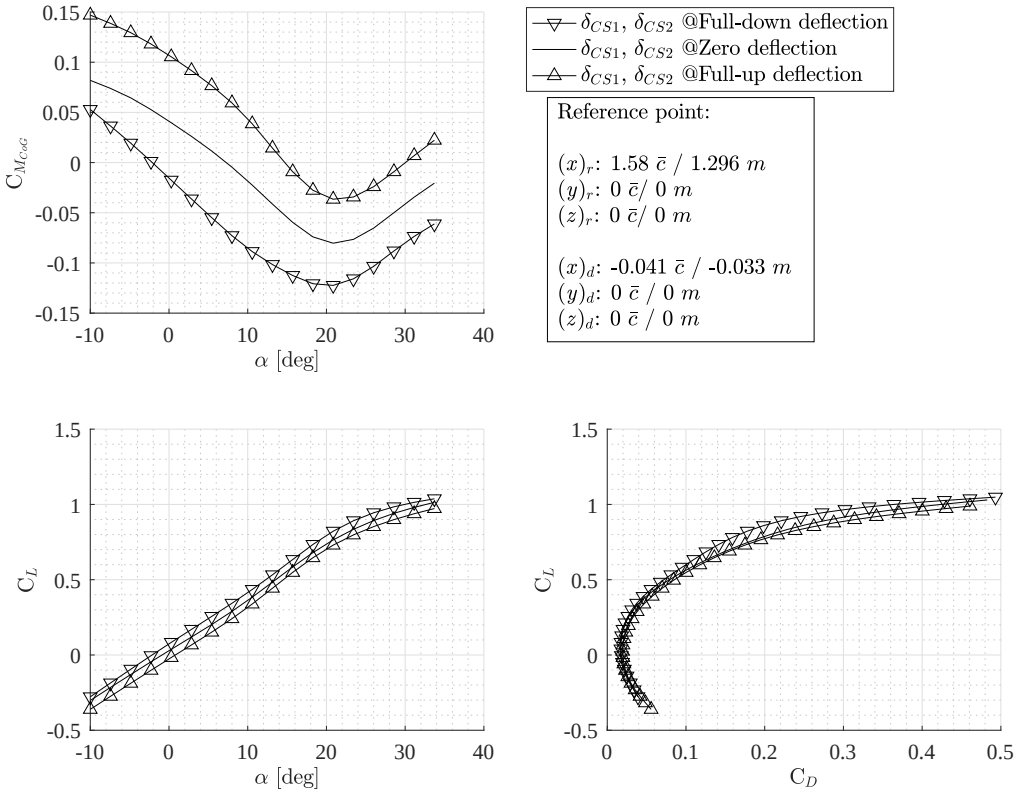

Figure B.1: Support picture. Aerodynamic characteristics Flying V model.

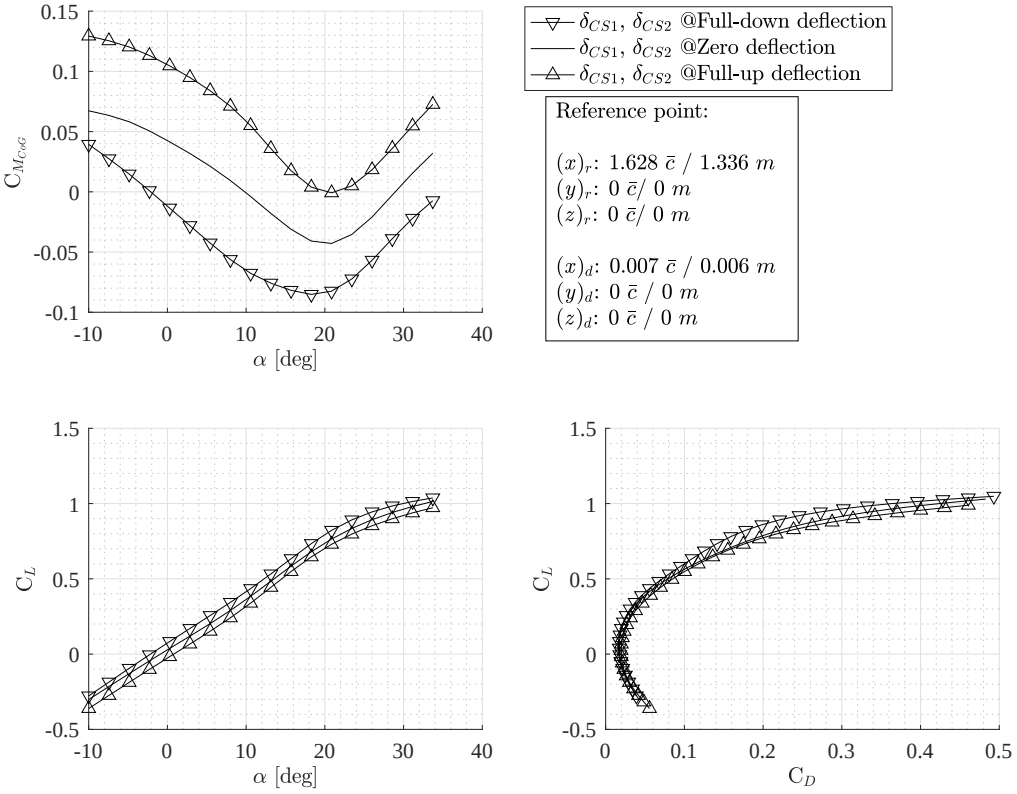

Figure B.2: Support picture. Aerodynamic characteristics Flying V model.

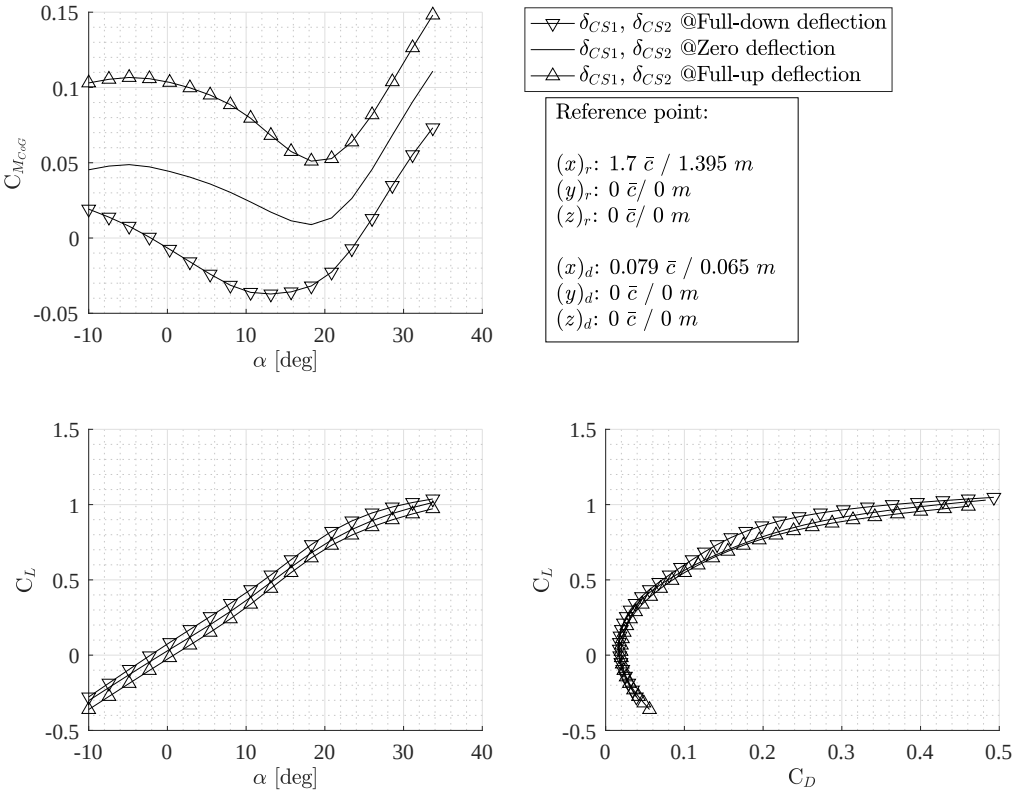

Figure B.3: Support picture. Aerodynamic characteristics Flying V model.

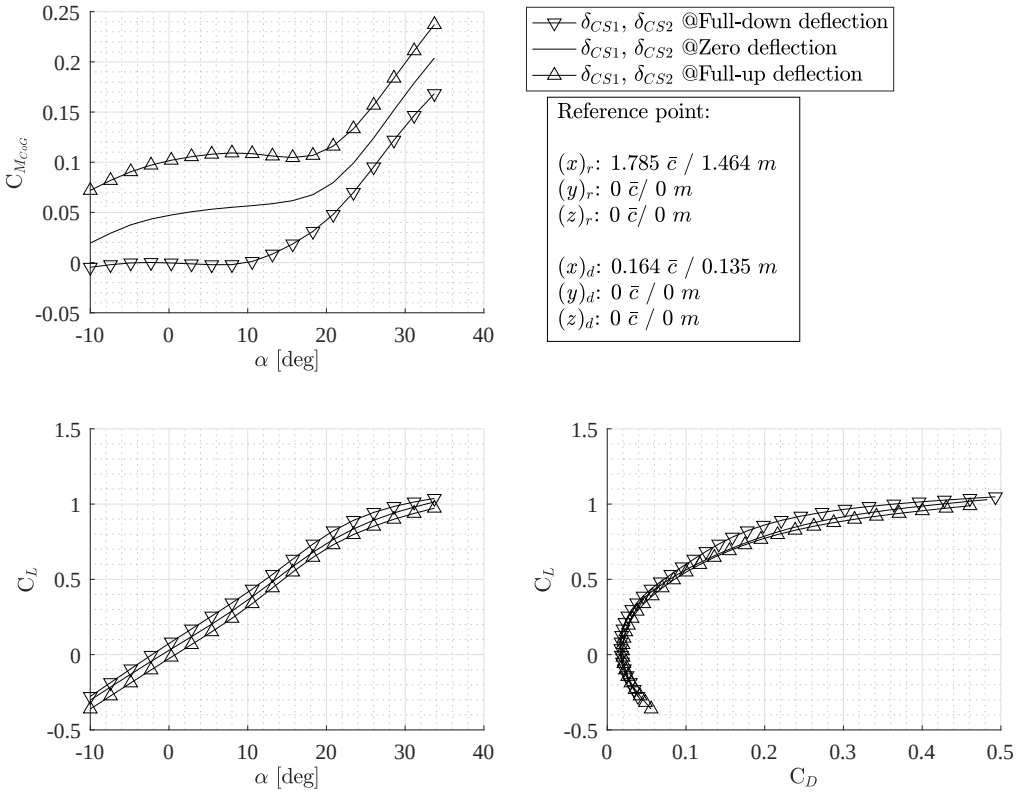

Figure B.4: Support picture. Aerodynamic characteristics Flying V model.